NTNU
Norwegian University of
Science and Technology

The potential of extracting wave energy from rip currents

Valentin Chabaud

Master of Science in Product Design and Manufacturing
Submission date: March 2011
Supervisor: Tor Ytrehus, EPT

Norwegian University of Science and Technology
Department of Energy and Process Engineering

Problem Description

Several approaches are under consideration for extracting energy from sea waves; largely by means of the motion of floating bodies, but also by means of stationary onshore constructions for upwelling of waves to higher elevations that allows for conventional hydropower production. A particular member of this last group is the concept of rip current, which employs small transversal barriers on an incline in the surf zone in order to promote breaking and elevation of incoming waves. The basic theory for such devices dates back to Longuet-Higgins (1962), and several simplified empirical approaches have been following along with experiments of sediment transport and breakwater devices. The objective of the present thesis is to build and test a model for rip current flow, and if possible, compare the performance with available theoretical or semi empirical predictions.

Assignment given: 30. August 2010
Supervisor: Tor Ytrehus, EPT

Preface

This report marks the end of a 5 months master thesis within the Norwegian University of Science and Technology (NTNU). At the same time it acts as the final internship of French Grandes Ecoles, within a double master degree program between the Energy & Processes department at NTNU and the National Polytechnic Institute of Grenoble (G-INP).

I had the chance to choose as topic my own concept of wave energy conversion, which I invented within a previous project on renewable energies at NTNU the year before. Extracting energy from breaking waves being a totally innovative concept, almost no technical supervising has been furnished since this field is not studied neither in the department of Energy & Processes neither in other departments of NTNU. The work has been done entirely in autonomy, from the literature survey to the model construction, from the analytical study to the experiments.

As a consequence communication had a significant role in the project, overall to realize experiments. That's why I would like to thank my supervisor Tor Ytrehus. Without his official support, my project would have never been possible. I am also grateful to those who have contributed to carry it through: Arnt Egil Kolstad, Sverre Steen, Torgeir Wahl, Dag Myrhaug and Geir Tesaker.

It is desirable to have some basics on linear wave theory and coastal engineering to read and completely understand the work presented hereby.

Valentin Chabaud

Trondheim 16.02.2011

Abstract

Existing wave energy converters are only based on a few ways to produce electricity from ocean waves. All of them suffer from low cost-efficiency so the proposal of new technologies is still up to date. This is a preliminary study to an innovative concept, based on wave-induced currents. As waves propagate into shallow water and break over a barrier, they dissipate their energy. The latter can be partly transformed in a hydraulic potential through the wave set-up behind the barrier and the cross-shore mass transport from waves. Electricity can then be produced by the mean of a water turbine.

This study estimates qualitatively this energy potential. The 2D set-up is analyzed by the model of Calabrese et al. (2008) and is adapted to 3D for a regulated net cross-shore discharge. The 3D model of Bellotti (2004) is also used. Experiments have been carried out on a simplified lab-scale model to check qualitatively the applicability of the models, determine experimentally their calibration parameters and find the optimal combination flow rate/pressure head which gives the highest hydraulic potential. Two different barrier profiles are tested: a breakwater-like barrier with a steep seaward slope and a sandbar-like barrier with a mild slope. Despite a significant uncertainty, experimental and analytical results correlate well.

The conclusions on the future of this technology are not thorough. Experimental conditions applied to full scale show a quite low efficiency compared to the main competitors, but much more perspectives of optimization are conceivable. Some of them have been studied from an analytical point of view.

Sammendrag

De eksisterende bølgekraftinnretningene er basert på et fåtall metoder for å produsere elektrisk energi fra havbølger. Felles for alle av dem er lav kostnadseffektivitet, derfor utvikling av nye teknologier er forstsatt aktuelt. Dette studiet er et forslag til et innovativt konsept, basert på bølgeinduserte strømninger. Mens bølger forplanter seg inn mot grunt vann og bryter over et rev, sprer energien deres i varme og turbulens. Men en del energi kan transformeres i hydraulisk potensial gjennom bølgeoppsettet (vannløftet) bak revet og massetransport parallelt med stranden. Elektrisk energi kan høstes ved bruk av en vannturbin.

Dette studiet anslår kvalitativt dette energipotensialet. Det 2D oppsettet er analysert med modellen fra Calabrese et al. (2008) og er adaptert til 3D for en regulert utstrømning i turbinen. 3D modellen fra Bellotti (2004) er også brukt. Eksperimenter har blitt utført på en forenklet småskala modell for å kvalitativt undersøke anvendbarhet av de analytiske modellene, bestemme eksperimentelt deres kalibreringsparametre samt finne det optimale forholdet mellom utstrømning og vannhøyden som gir det høyeste hydrauliske potensialet. To forskjellige revprofiler er undersøkt: et ”breakwater-like” rev med høy innfallende skråning og et ”sandbar-like” rev med lav skråning. Til tross for nevneverdig usikkerhet, korrelerer de eksperimentelle og analytiske resultatene bra.

For å trekke konklusjoner rundt denne teknologiens fremtid, behøves grundigere forskning. Overføres resultatene fra dette studiet til en storskala modell, oppnås ikke høy virkningsgrad sammenlignet med andre bølgekraftinnretninger. Imidlertid har dette konseptet stort forbedringspotensial, og noen forbedringsområder er presentert hermed.

Table of Contents

List of figures

List of symbols

Notation	Definition	Dimension
A	Barrier reaction coefficient	$[m]$
$A_{barrier}$	Cross section over the barrier	$[m^2]$
$A_{channel}$	Cross section in the channel	$[m^2]$
A_{trough}	Area of the trough	$[m^2]$
A_{ts}	Area of the test section	$[m^2]$
B_0	Wave shape factor	$[-]$
c	Wave phase celerity	$[m.s^{-1}]$
c_g	Wave group velocity	$[m.s^{-1}]$
C_v	Head loss coefficient	$[-]$
d	Gate opening	$[m]$
d_H	Hydraulic diameter	$[m]$
E	Wave energy	$[kg.m.s^{-2}]$
E_f	Wave energy flux	$[kg.m^2.s^{-3}]$
F	Reaction of the barrier	$[kg.m.s^{-2}]$
f, f', f''	Friction coefficients	$[m^{-3}.s^2], [s^{1/2}], [m^{-1}.s]$
f_w	Wave-current friction factor	$[-]$
G	Shallow water number	$[-]$
g	Gravity constant	$[m.s^{-2}]$
H	Wave height	$[m]$
h	Depth or submergence	$[m]$
h_0	Bore upstream depth	$[m]$
h_1	Bore downstream depth	$[m]$
h_m	Bore head height	$[m]$
K	Friction factor	$[-]$
k	Wave number	$[rad.m^{-1}]$
K_i	Splitting coefficient	$[-]$
k_N	Equivalent sand grain roughness	$[m]$
K_r	Reflection coefficient	$[-]$
K_s	Shoaling coefficient	$[-]$
K_t	Transmission coefficient	$[-]$
K_{WM}	Wave maker coefficient	$[-]$
L	Wave length	$[m]$
$L_{barrier}$	Length of the barrier	$[m]$
L_{gate}	Length of the channel at the gate	$[m]$
P	Hydraulic potential, Pressure forces	$[kg.m^2.s^{-3}], [kg.m.s^{-2}]$
Q	Flow rate in the channel	$[m^3.s^{-1}]$
q	2D discharge in the channel	$[m^2.s^{-1}]$
Q_{in}	3D cross-shore discharge (influx)	$[m^3.s^{-1}]$
q_{in}	2D "	$[m^2.s^{-1}]$
Q_u	3D undertow	$[m^3.s^{-1}]$
q_u	2D "	$[m^2.s^{-1}]$
R_c	Hydraulic resistance in the channel	$[m^{-1}.s]$
R_u	Hydraulic resistance over the barrier	$[m^{-1}.s]$
R_{vf}	Hydraulic resistance due to volume flux (negative)	$[m^{-1}.s]$
S	Stroke of the wave maker	$[m]$
S_{xx}	Radiation stresses: Cross-shore component	$[kg.m.s^{-2}]$

S_{xy}, S_{yx}	Radiation stresses: Shear components	$[kg.m.s^{-2}]$
S_{yy}	Radiation stresses: Alongshore component	$[kg.m.s^{-2}]$
T	Wave period	$[s]$
t	time	$[s]$
U	Velocity	$[m.s^{-1}]$
u	Horizontal particle velocity	$[m.s^{-1}]$
U_0	Bore head velocity	$[m.s^{-1}]$
U_f	Friction velocity	$[m.s^{-1}]$
U_{fc}	Friction velocity from current	$[m.s^{-1}]$
U_{fw}	Friction velocity from waves	$[m.s^{-1}]$
w	Vertical particle velocity	$[m.s^{-1}]$
x	Cross-shore position	$[m]$
y	Alongshore/transversal position	$[m]$
z	Vertical position	$[m]$
α	Discharge fraction	$[-]$
$\tan\beta$	Seaward slope	$[-]$
Γ_c	Continuity parameter	$[-]$
Γ_{vf}	Volume flux parameter	$[-]$
ΔH	Pressure head, error in wave height	$[m]$
δ	Wave set-up	$[m]$
δ_c	Continuity set-up	$[m]$
δ_{mf}	Momentum flux set-up	$[m]$
δ_{vf}	Volume flux set-up	$[m]$
η_3	Heave motion	$[m]$
θ	Angle of incidence	$[rad]$
κ	Von Karman constant	$[-]$
ν	Dynamic viscosity	$[m^2.s^{-1}]$
ξ	Surf similarity parameter	$[-]$
ρ	Density	$[kg.m^{-3}]$
τ	Friction forces	$[kg.m.s^{-2}]$
ϕ	Velocity potential	$[m^2.s^{-1}]$
ω	Wave frequency	$[rad.s^{-1}]$

subscript, accentuation, superscript:

$_t$	Transmitted/trough
$_0$	Offshore
$_b$	Breaking, bottom
$_c$	Crest
$_i$	Incident
$\_^a$	On the alongshore axis of symmetry
	Averaged over one wave period
*	Dimensionless
$_{opt}$	Optimal
$_{eff}$	Effective (deduced from head losses estimation)
$_{kin}$	Kinetic
$_{pot}$	Potential
$_1$	First barrier, 2D ($\alpha = 1$)
$_2$	Second barrier

I. Introduction

With today's focus on global warming and CO_2 emissions, research and development of renewable energy is more important than ever. While hydropower and wind power have been an important source of renewable energy for a long time, wave power is still a relatively unused source of energy, in spite of its huge potential.

Existing concepts are at the moment at a more or less advanced stage of development, none of them being at a real commercial stage. The challenge of wave energy is indeed to overcome a high initial cost. The latter is due to harsh environment in open sea and no large scale production. Therefore no convergence toward a most cost-efficient device has been started, and the best concept is still to be found.

There are many technologies in use, and more under development, but they all seem to be derivatives and improvements of the same conventional solutions and suffer from the same intrinsic problems.

In quest of a new energy source, inspiration has been found on shores and breaking waves. Besides the waves themselves, a natural phenomenon known as a rip current shows potential as a source of renewable energy.

This study analyzes this innovating concept which has in appearance many advantages with respect to existing wave energy converters, insofar as it has a high enough energy potential to be competitive.

The goal of this study is consequently to estimate this energy potential.

A project on the field had been done previously by the author, and the main features to develop in the thesis were the following:

- Realize a deep literature survey on the field to find out the main processes related to the concept and their governing equations
- Find a simple but accurate enough analytical model and adapt it to describe the processes related to the new wave energy converter
- Perform experiments and compare results to theory to bring credibility to the model
- Use experimental results to determine the input parameters needed in the analytical model
- Optimize analytically the energy potential

The conclusions should teach us whether it is worthy to carry on the research on this new way of capturing wave energy.

II. Nearshore processes

A brief outline of the nearshore processes and technical terms in the surf zone is presented here. Further information can be found in the books *Mechanics of coastal sediment transport*, by Fredsøe & Deigaard (1992) and *Introduction to nearshore hydrodynamics*, by Svendsen (2006).

A more detailed explanation of these processes including governing equations is available in appendices, together with basics on wave linear theory.

Let's consider the barred beach profile Figure II-1, with a **mild seaward slope**, a **barrier** (sandbar, reef…) and a **trough** behind.

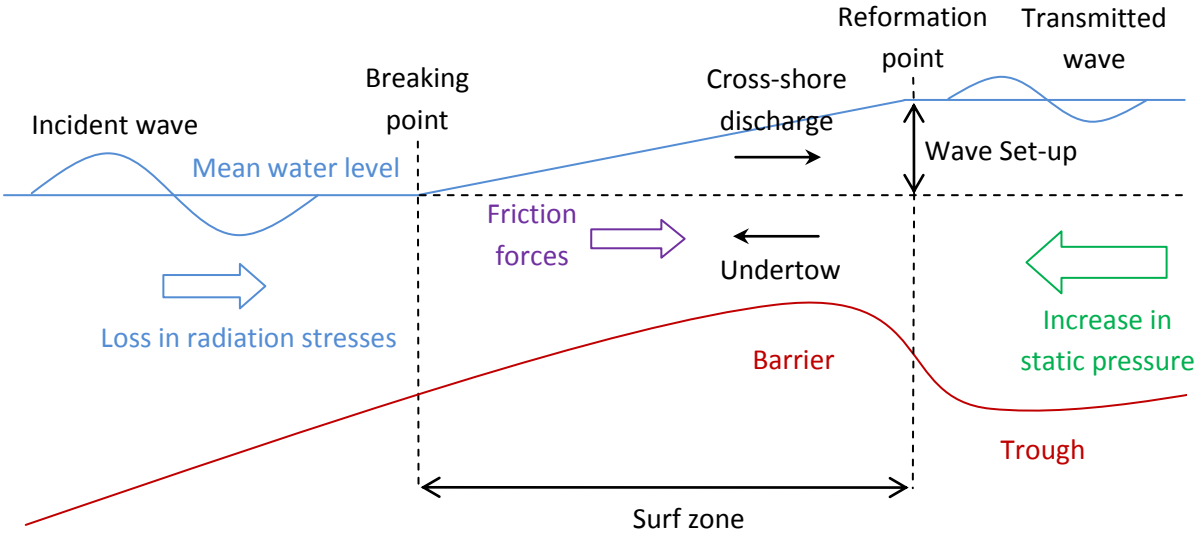

Figure II-1: 2D beach profile

As the waves propagate into shallower water, a process called **wave shoaling** make the wave height increase and the wave length decrease. As a consequence the steepness of the wave increases, until the top of the wave falls forward, creating foam called "**surface roller**". This is **wave breaking**. At first, the ordinate wave transfers its energy to the surface roller in the form of kinetic energy. The surface roller then dissipates this energy into turbulence and heat.

The **surf zone** is therefore the place where waves dissipate their energy. However, the energy of the wave is proportional to the wave height squared, so the wave height decreases.

Waves and surface rollers carry also momentum. This is called "**radiation stresses**", from the theory of Longuet-Higgins (1964). This momentum is also proportional to the wave height squared, so it decreases as the wave breaks.

The loss of momentum (dynamic pressure) in the surf zone has to be compensated by a gain of static pressure, i.e. an elevation of the mean water level. This is the so-called **wave set-up**.

At the same time, mass is carried inshore the barrier. This **cross-shore** (perpendicular to the beach) **discharge** (or influx) has to flow out from the trough. With 2D conditions (infinite barrier in the **alongshore** direction, i.e. parallel to the beach), the only way is to return offshore over the barrier. This flow is the so-called **undertow**.

The cross-shore discharge is located between the wave trough and the wave crest. Over the barrier, the undertow flows therefore in a narrow duct between the sea bottom and the trough of the wave. This induces large **friction forces** that must be compensated. It leads to an additional increase of the set-up.

As the water becomes deep again in the trough behind the barrier, breaking stops. It is **wave reformation**. The **transmitted wave** thus created propagates shoreward until it breaks again.

Let's now consider a no longer uniform beach profile in the alongshore direction, with a gap in the bar called "**rip channel**", like on Figure II-2. The larger depth in the channel leads to a weaker breaking (or no breaking at all), so a lower set-up. A **pressure gradient** is formed, driving a flow called feeder or **longshore current** in the trough and gathering into the channel to form a **rip current**.

The cross-shore discharge is then split into the undertow and the longshore current. The decrease in the undertow leads to a decrease of the wave set-up, since there is less friction.

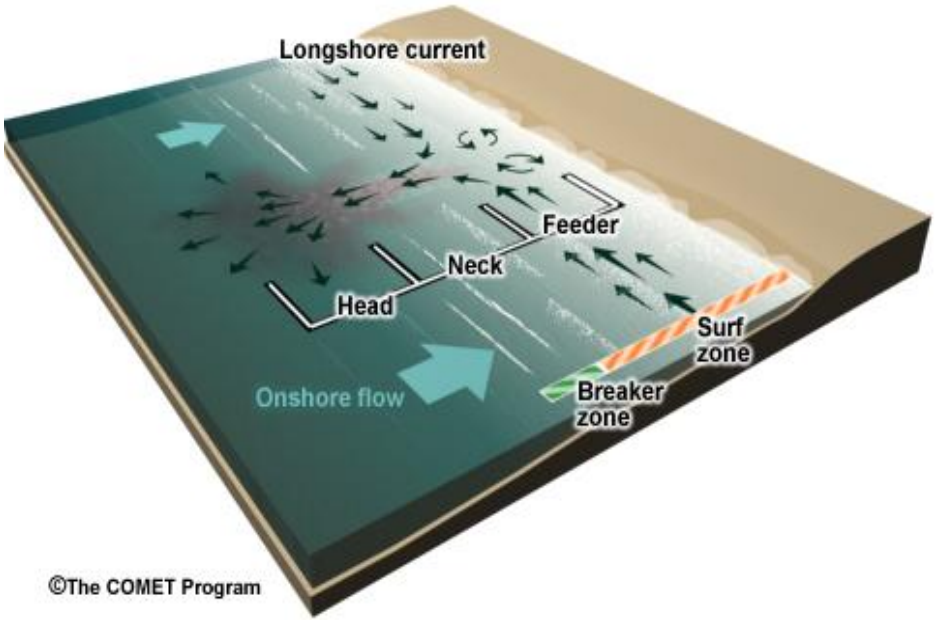

Figure II-2: Rip system

III. An innovating concept of wave energy conversion

The processes described in part II can be used to produce energy. The energy from the waves is first transformed in hydraulic energy with a pressure head and a flow rate.
It can then be used to produce electricity through a turbine.

The concept is shown on Figure III-1 and Figure III-2. The channel has been replaced by a duct starting from the trough behind the barrier. The water flows then downwards before it is dispersed underneath the structure.

The potential can be calculated classically with the formula

$$P = \rho g Q \Delta H$$

In which $Q = Flow\ rate, or\ Cross\ shore\ discharge\ over\ the\ barrier$
$\Delta H = Pressure\ head, or\ Wave\ set - up$: *Elevation of water due to excess of momentum + excess of mass*

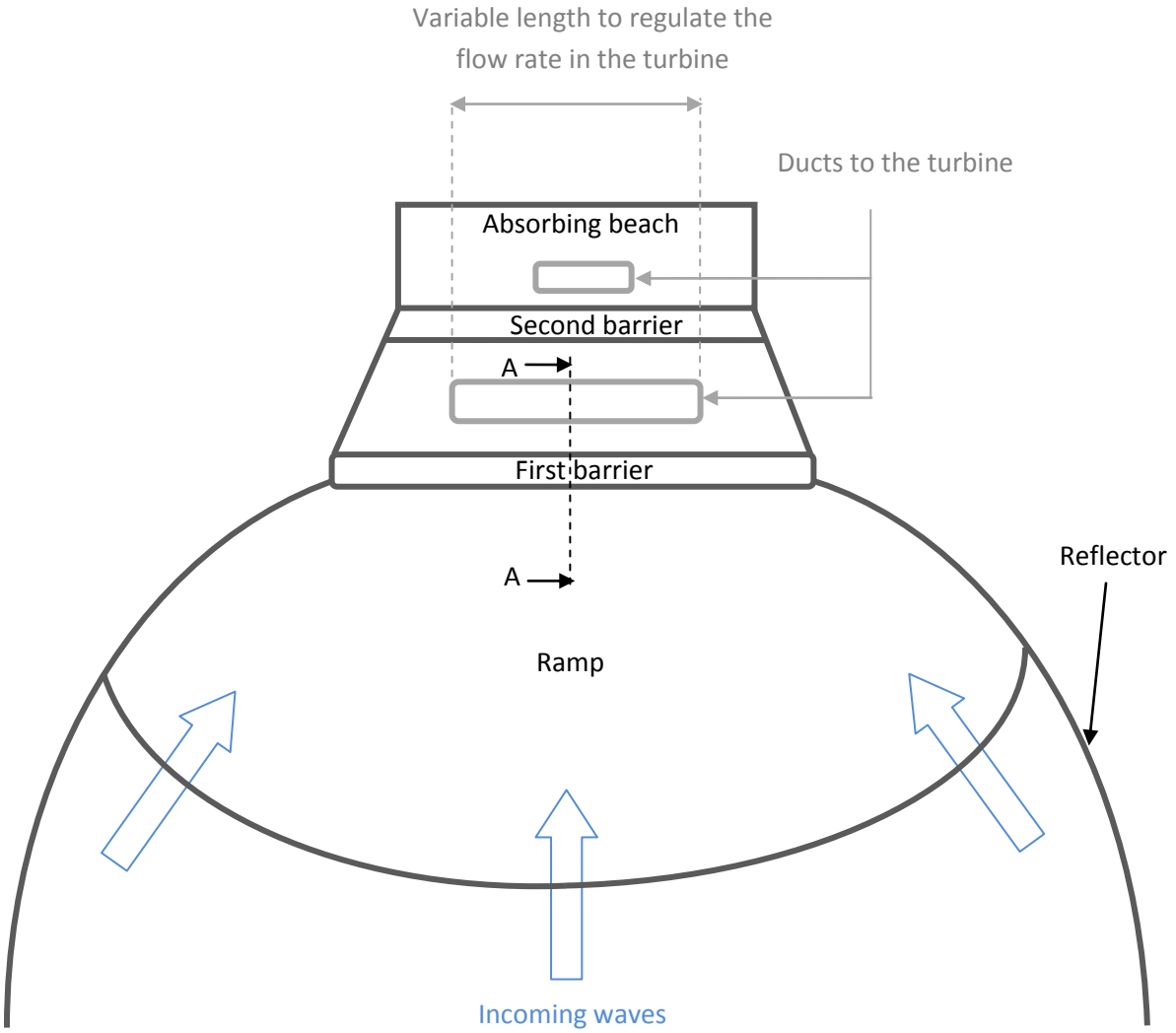

Figure III-1: Wave energy converter, top view

Q can be regulated. ΔH depends on Q, the incident wave conditions and the geometry of the barrier.

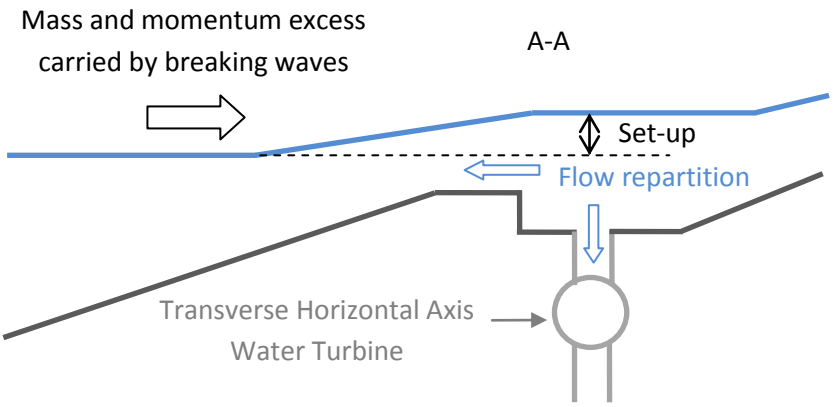

Figure III-2: Wave energy converter, side view

IV. Review on wave breaking and nearshore processes

Wave breaking and related processes in the surf zone have been the topic of many investigations these last decades. Many analytical and numerical models, experimental studies, field surveys can be found in the literature. However there is no final agreement on a single way of modeling, each university/company proposing its own model. Numerical models are developing fast but none of them can really predict the natural phenomena without empirical relations, because of the physical and numerical difficulty to describe the strongly non-linear process of wave breaking. The lack of general governing equations confines existing models to the description of the natural phenomena, whose analysis is economically reliable regarding sediment transport and therefore coastal engineering. Even if the concept in this study isn't theoretically stuck to existing phenomena, we have no other choice to consider the same configurations to be able to use existing models.

Before numerical models made their apparition, empirical formulas on wave breaking and set-up were first developed. Among them we can mention the pioneer works of Miche (1944) and Munk (1949) who first determined a wave breaking criterion in terms of depth or given deepwater wave conditions. An applicability study of these empirical formulas to steep slopes (higher than 1/10) was done by Tsai et al. (2005).

Regarding wave breaking, wave energy dissipation and wave set-up, a major work which most models are based upon was done in Svendsen (1984a), then improved in Hansen (1990) and Svendsen & Putrevu (1993). He linked the decay of wave height across the surf zone and the energy dissipation, using the radiation stress theory introduced by Longuet-Higgins & Stewart (1964). He also introduced the effect of the surface roller in his model.

Extension to irregular waves (random wave breaking) and transformation of the wave spectrum has also been the topic of several studies, for instance Thornton and Guza (1983), Dally (1992) or Goda (2004).

The radiation stress theory has been improved by calculating its vertical variation (for instance Xia et al. 2004). Wang et al. (2008) used a non-linear numerical model of wave breaking to improve the model of Svendsen, whose main disadvantage is to average the quantities over one wave period and therefore to linearize a strongly non-linear process.

Some studies of wave breaking more specific to submerged reefs were done by Blenkinsopp & Chaplin (2010) and Calabrese et al. (2008). The first one analyzed experimentally the effect of the seaward slope on breaking, set-up and reflection. The second one determined the type of breaker on submerged breakwaters according to their geometry. The type of breaker has a strong impact on the intensity of breaking and therefore on the set-up.

The net flow over a nearshore bar was analyzed by Dalrymple (1978). A resulting work in the modeling of the processes driving the undertow, resulting from 2D mass conservation in the surf zone, was given by Svendsen 1984b. It was improved in Hansen & Svendsen (1985), and checked experimentally in Hansen & Svendsen (1987) and Svendsen & Hansen (1987). At the same time Stive & Wind (1986) developed a similar model. The incorporation of the undertow in nearshore currents modeling was studied by Svendsen & Buhr Hansen (1988) in order to develop the numerical model SHORECIRC. An example of field application survey can be found in Greenwood & Osborne (1990). An alternative model based on the same principles was found out by Tajima & Madsen (2006). The effect of beach reflection on the undertow was studied by Veiskarami et al. (2009).

Alternative models including the undertow and the longshore current were proposed in Kuriyama & Nakatsukasa (2000), Ostrowski et al. (2003) and Zheng et al. (2008).

The study of the longshore current from obliquely incident waves on a longshore bar has been the subject of many investigations. Among them we can notice the work of Goda (2006, 2008) who introduced a state-of-the-art modeling of random wave breaking, and the experimental study of Reniers & Battjes (1997).

Finally, the description of rip currents was first done in the pioneer work of Bowen (1969) from the radiation stress theory. Aagaard et al. (1997) proposed a simplified modeling based on mass conservation. Thorough experimental analyses were performed by Haller et al. (2002) and Drønen et al. (2002), coming to both similar and complementary conclusions. A numerical analysis with the model SHORECIRC can be found in Haas et al. (2002). Plenty of field surveys have been done (for instance Castelle et al. (2005)). A global review was done by Mc Mahan et al. (2006).

The studies presented above concern mainly sediment transport, and main features are gathered in Fredsøe and Deigaard (1992), or more in details in Svendsen (2006).

Simplified models for engineering applications have been done within the development of breakwaters to protect the coastline (Johnson et al. (2005), Soldini et al. (2009), Vicinanza et al. (2009)). Bellotti (2004) proposed a very simplified analytical model. Calabrese (2008) focused on an ideal 2D case (infinitely long breakwater) to analyze the set-up splitting it in two contributions, after the work of Dalrymple and Dean (1971). The models need an empirical transmission coefficient of the wave height behind the breakwater, for example given in Diskin et al. (1970), Van der Meer & D'Angremont (1992), or more recently in Van der Meer et al. (2005), Shirlal et al. (2006), Wang et al. (2007) or Buccino & Calabrese (2007). Chang (2007) studied wave reflection by several breakwaters.

V. Analytical models

A. Variables and notations

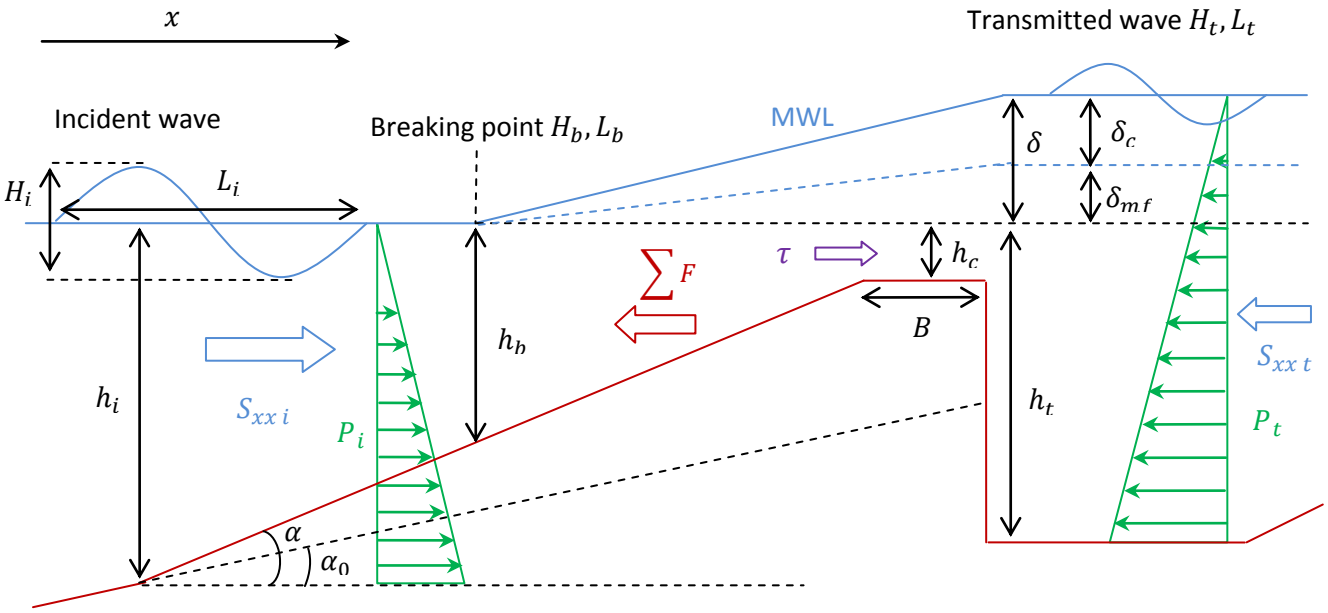

Figure V-1: Variables and notations for analytical models

B. 2D model

The study is based on the analytical model of Calabrese (2008). The main difference between other models is the assumption proposed by Dalrymple and Dean (1971) who split the set-up in two contributions $\delta = \delta_{mf} + \delta_c$.

These two contributions result from momentum and mass conservation laws across the barrier.

δ_{mf} is called the the momentum flux set-up and accounts for the conservation of momentum. It represents the increase in mean water level (static pressure) in the surf zone due to the loss of radiation stresses (dynamic pressure) caused by the wave height decay from energy dissipation.

δ_c is called the continuity set-up and accounts for the conservation of mass. The mass transported over the barrier has to return seaward by the same way it came. The hydraulic diameter over the barrier is low so the friction is high. δ_c compensates the friction forces noted τ on Figure V-1.

1. Momentum flux contribution

Calabrese assumed the wave set-down to be less than ten times lower than the wave set-up and negligible.

As the wave height decreases due to breaking, the cross-shore component of the radiation stress S_{xx} is lower onshore than offshore of the barrier.

The momentum balance in the horizontal direction reads:

$$S_{xx\,t} + P_t = S_{xx\,i} + P_i - \sum F \qquad \text{Eq. V-1}$$

With $\sum F$ the horizontal component of the sum of external forces, here the reaction of the barrier, as expressed by the following:

$$\sum F = -\int_{x_b}^{x_t} \rho g\big(h(x)+\delta(x)\big)\frac{\partial h}{\partial x}dx = -\rho g\left(\frac{h_t^2}{2}-\frac{h_b^2}{2}\right) - \rho g\delta_{mf}\int_{x_b}^{x_t}\frac{x-x_b}{x_t-x_b}\frac{\partial h}{\partial x}dx$$
$$= -\rho g\left(\frac{h_t^2}{2}-\frac{h_b^2}{2}\right) - \rho g\delta_{mf}\,A \qquad \text{Eq. V-2}$$

For simplicity, it has been assumed that only the mean hydrostatic pressure plays a role here. Integrated dynamic pressures and Reynolds stresses over the barrier are expected to vanish or be negligible. The longer the barrier, the better these assumptions are.

h_b and then x_b are calculated by the use of the following wave breaking criteria:

$$\begin{cases} H_i = \frac{1}{1+K_r}\left[0.218 - 0.076\frac{1-K_r}{1+K_r}\right]L_b \tanh\left(2\pi\frac{h_b}{L_b}\right) & \text{if } h_i \le h_b \le h_c \quad \text{Iwata and Kiyono (1985)} \\ h_b = h_c \quad \text{if} \quad H_i \ge 0.095\,L_0\,tanh\left(2\pi\frac{h_c}{L_0}\right) & \text{Hur et al. (2003)} \end{cases}$$

Where L_0 is the deepwater wave length. L_0 and L_b are calculated from L_i through the wave dispersion relation (see appendices for basics on wave linear theory).

In his work Calabrese considered the same depth for the offshore and inshore toes ($h_i = h_t$). A general expression is derived here. h_t can vary up to the wave reformation limit. A common value for the wave reformation was proposed by Dally (1992): $\frac{H_t}{h_t} \le 0.4$.

Considering the transmission coefficient $K_t = \frac{H_t}{H_i}$ and the reflection coefficient $K_r = \frac{H_r}{H_i}$ (calculation method in appendix E), we get from radiation stress theory (see appendix D):

$S_{xx\,i} = \frac{1}{8}\rho g H_i^2(1+K_r^2)\left(\frac{2k_ih_i}{\sinh 2k_ih_i}+\frac{1}{2}\right)$ and $S_{xx,2} = \frac{1}{8}\rho g H_i^2 K_t^2\left(\frac{2k_th_t}{\sinh 2k_th_t}+\frac{1}{2}\right)$

If h_t doesn't match the reformation criterion, $K_t = 0$.

The pressure forces are:

$P_1 = \frac{1}{2}\rho g h_i^2$ and $P_2 = \frac{1}{2}\rho g\big(h_t+\delta_{mf}\big)^2$

We therefore get a second order equation in δ_{mf}:

$$\frac{1}{2}{\delta_{mf}}^2 + (h_t - A)\delta_{mf} + \frac{1}{\rho g}(S_{xx\,t} - S_{xx\,i}) + \left(\frac{h_t^2}{2}-\frac{h_i^2}{2}\right) - \left(\frac{h_t^2}{2}-\frac{h_i^2}{2}\right) = 0$$

Which has only one positive solution:

$$\delta_{mf} = A - h_t + \sqrt{(h_t-A)^2 - \frac{2}{\rho g}(S_{xx\,t} - S_{xx\,i})} \qquad \text{Eq. V-3}$$

This is valid as long as the crest depth is high enough, i.e the bar is continuously submerged over one wave period. Calabrese suggested that it should only be used within the range $0.3 \le \frac{h_c}{H_i} \le 2$.

If the crest submergence is lower, overtopping effects become significant, and emerged barriers could be considered as weirs (Dalrymple and Dean1971, Loveless et al.1998). It is not the goal here since such phenomenon is already used by existing wave energy converters.

2. Continuity contribution

The continuity set-up is given from Bernoulli equation $\delta_c = f {q_u}^2$ where f is a friction coefficient to be determined and q_u is the discharge returning seaward (undertow). In the 2D situation q_u equals q_{in}, the cross shore discharge carried by waves over the barrier.

3. Cross-shore discharge

Calabrese used the following approximation, from Svendsen (1984b) :

$$q_{in} = \sqrt{g h_c} H_c \left(B_0 \frac{H_c}{h_c} + 0.06 \right) \qquad \text{Eq. V-4}$$

with B_0 the wave shape factor. $B_0 \approx \frac{1}{12}$ for a saw tooth profile. Calabrese used another formulation of B_0, but it appeared to underestimate the flow rate with respect to experimental results (3D tests).

H_c was approximated by Calabrese as $\frac{H_i + H_t}{2}$, though it is known that there is a drop in the wave height right after the barrier, where dissipation is the highest due to the brutal change in depth. H_c should then be closer to $H_i$than to H_t. This may compensate the difference in the formulation of B_0 for the small scale case, since analytical and experimental results coincide well. However when extrapolating the model to real scale, B_0 is not expected to change unlike the difference in H_c which increases with the scale. The cross-shore discharge might then be somewhat underestimated in the final calculation of the potential.

At the same time, B_0 and therefore q_{in} should be increasing proportionally to the square root of the wave steepness. Taking B_0 as constant introduces an additional uncertainty.

A more accurate calculation of B_0 can be found in Hansen (1990).

4. Friction factor

Regarding the friction coefficient, Calabrese used the Gauckler-Strickler formula which gives

$$f = \frac{B_{eq}}{K} {d_H}^{-10/3} \qquad \text{Eq. V-5}$$

d_H is the hydraulic diameter, K is a friction factor, B_{eq} is an equivalent width of the barrier. The formulation of Calabrese has been adapted for a sloped bottom: $B_{eq} = \frac{A_{barrier}}{\frac{h_i + h_t}{2} - h_c}$ in which $A_{barrier}$ is the cross section of the barrier.

K can be calculated from the wave-current friction factor f_w by the relation: $K = \sqrt{\frac{2g}{f_w {d_H}^{1/3}}}$. It is there assumed that the boundary layer is rough turbulent and that the amplitude of the bottom particle velocity from waves $u_{c\,b}$ is much higher than the bottom velocity from current $U_{c\,b}$.

Regarding the first assumption, it should be reasonable considering the small hydraulic diameter and the turbulence from breaking.

The second assumption is validated in the following:

$u_{c\,b} = \frac{\pi H}{T}\frac{\cosh(k_{eq}h_{eq})}{\sinh(k_{eq}h_{eq})}$ where h_{eq} is an equivalent height of the barrier: $h_{eq} \approx \frac{2(h_i-h_c)^2+6h_c(h_i-h_c)+h_cB}{B+6(h_i-h_c)}$

Calculations from experimental data for small scale give an order of magnitude of $u_{c\,b}$ of 0.3 m/s while the averaged value of the current velocity over the depth is 0.1 m/s, so the bottom velocity $U_{c\,b}$ is much lower. Therefore $u_{c\,b} \gg U_{c\,b}$.

f_w is calculated from the relation

$$f_w = 0.04\left(\frac{u_{c\,b}\,T}{\frac{2\pi}{k_N}}\right)^{-1/4}$$ Eq. V-6 (from Fredsøe & Deigaard (1992)).

Methods to calculate the equivalent sand roughness k_N can be found in Schlichting & Gersten (1999). In this case like in most situations it must be determined experimentally.

C. Simple analytical 3D model for engineering applications

The model presented above is an ideal 2D case. In reality a fraction of the flow is returning offshore through the undertow and the other fraction is flowing in the channel. Bellotti (2004) proposed a simple 3D model giving an analytical solution to the 3D set-up, using the cross section of the channel together with a simple head loss model.

Up to now, this 3D modeling needed numerical simulations or crude empirical formulas. This model aims to give a first idea of the order of magnitude of the set-up without using complicated numerical models, for example to design breakwaters.

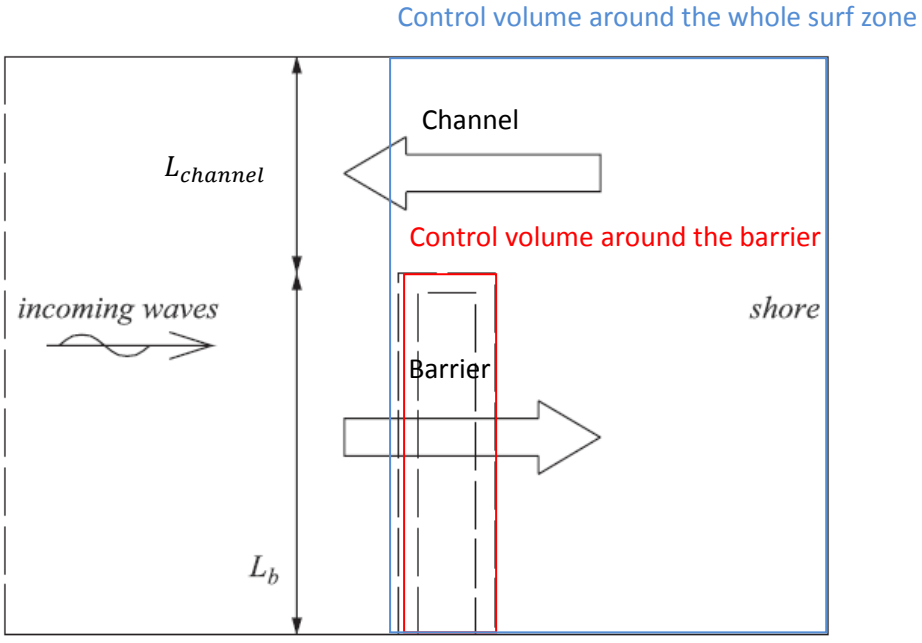

Figure V-2: Top view and control volumes used in Bellotti (2004)

It is based on integrated equations over control volumes shown on Figure XII-9.

Momentum conservation over the barrier reads:

$$\underbrace{(h_t+\delta){U_t}^2-h_i{U_i}^2}_{Volume\ flux}+\underbrace{\frac{g}{2}\left((h_t+\delta)^2-{h_i}^2\right)}_{Pressure}+\underbrace{\sum F}_{Reaction}+\underbrace{(S_{xx\,t}-S_{xx\,i})}_{Radiation\ stresses}-\underbrace{\tau}_{Friction}=0 \qquad \text{Eq. V-7}$$

Eq. V-7 is similar to **Eq. V-1**, but the volume flux forces have been added and there is no separation of the two contributions of the set-up.

Bellotti kept the friction term in its final equation, but the friction coefficient has no physical meaning and is used as a calibrating parameter. The author showed that it has a weak effect on the results and therefore could be neglected.

Mass conservation in the surf zone reads:

$$\begin{cases} (h_t+\delta)U_t-h_iU_i=0 \quad across\ the\ barrier \\ A_{barrier}U_i+A_{channel}U_{channel}=0 \quad on\ the\ entire\ surf\ zone \end{cases}$$

The major assumption is to estimate the velocity in the channel as $U_{channel}=C_v\sqrt{2g\delta}$, in which C_v is a head loss coefficient from flow contraction (see Chow 1959). The undertow and the flow repartition are taken into account in an implicit manner.

It leads to the following equation:

$$\frac{\delta^2}{2}+\delta\left(C_v h_i\,\frac{A_{channel}}{A_{barrier}}\right)^2\left[\frac{2}{h_t+\delta}-\frac{2}{h_i}+B_{eq}\,\mu\left(\frac{1}{h_t+\delta}+\frac{1}{h_i}\right)^2\right]+\delta(h_t-A)+\frac{3}{16}\left({H_t}^2-{H_i}^2\right)=0 \qquad \text{Eq. V-8}$$

In which μ is the friction factor. Bellotti took $B_{eq}=B$, however it is more accurate to use the formulation of Calabrese (used in **Eq. V-5**).

A is identical to the one in **Eq. V-2**, but Bellotti calculated it from the incident point and not the breaking point.

Eq. V-8 has to be solved by iterations, for example with the Newton method using the 2D value $\left(\frac{A_{channel}}{A_b}=0\right)$ that can be calculated analytically as a guess value.

The model of Bellotti is known to underestimate 2D wave set-up (from Calabrese (2008)). It is not expected to be valid with too low values of $\frac{A_{channel}}{A_{barrier}}$. It is based on many rough assumptions, and has only been validated experimentally for $\frac{A_{channel}}{A_{barrier}}=0.2$. It would be interesting to check its ability to predict the variation of δ with $\frac{A_{channel}}{A_{barrier}}$.

D. Transmission coefficient

Both 2D and 3D models need the transmission coefficient across the barrier. Its behavior with the crest submergence has been studied for submerged reefs by Blenkinsopp and Chaplin (2008). However they didn't include an explicit formulation and the crest width was inexistent (no flat part).

We shall use the theory proposed by Van Der Meer et al. (2005), who proposed empirical formulas of transmission coefficient across breakwaters, adapted from Van der Meer & d'Angremont (1992):

$$K_t = -0.4\,\frac{h_c}{H_i} + 0.64\left(\frac{B}{H_i}\right)^{-0.31}\left(1 - \mathrm{e}^{-0.5\xi_i}\right) \qquad \text{Eq. V-9}$$

ξ_i is the surf similarity parameter introduced by Battjes (1974): $\xi_i = \frac{\tan\beta}{\sqrt{\frac{H_i}{L_i}}}$ in which $\tan\beta$ is the seaward slope of the barrier.

It is important to notice that this formula has been designed for a totally different purpose than creating the highest set-up. Indeed breakwaters are designed to protect shore. Consequently they target a very low transmission coefficient, a high reflection coefficient and a low set-up as well, since the set-up enhances sediment erosion through nearshore currents and therefore damages the shore.

As a consequence we will use this formula with some parameters values different from the usual ones: The crest width will be lower, the barrier submerged and the seaward slope milder.

E. 3D model derived from 2D model

The main difference between rip currents and the concept of wave energy conversion presented hereby is the regulation of the discharge in the channel.

Indeed the natural phenomenon has no regulation. The wave forcing conditions are naturally changing the morphology of the beach, and the discharge in the rip channel is a direct function of these conditions.

In our case, we can regulate the flow rate independently on the forcing conditions (set-up), by the use of a gate. We can therefore choose the fraction of the flow which returns directly offshore as undertow and the one which flows toward the channel, or toward the turbine.

To describe these processes, an alternative way of modeling is proposed. An equivalent RC electrical circuit has been used to model the dynamics of the mass conservation in the surf zone, as shown on Figure V-3.

The inshore mass flux q_{in} carried by the waves can be modeled by a constant current generator. The head losses over the barrier δ_c and in the channel δ are modeled by electrical resistances R_u and $R_{channel}$ and the reservoir formed by the trough behind the barrier is a capacitor. R_{vf} is a negative resistance which accounts for the volume forces.

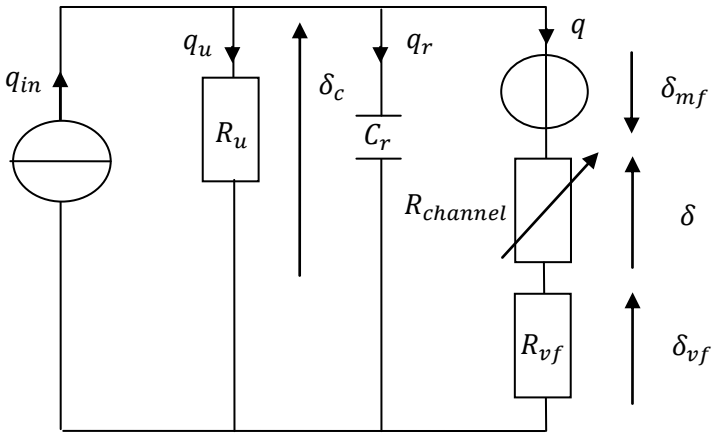

Figure V-3: Equivalent circuit diagram

$R_{channel}$ (i.e. the opening of the gate) is variable to regulate the discharge in the channel q.

Behind the barrier, mass conservation reads

$$q_{in} = q + q_u + A_{trough}\frac{d\delta_c}{dt} \qquad \text{Eq. V-10}$$

In which A_{trough} is the area of the trough and q_u the undertow.

1. Dynamics of the continuity setup

The initial conditions are still water (no setup) and 2D conditions (channel closed), i.e $\delta_c = 0$ and $R_{channel} = \infty$.
As a consequence when the first waves break on the barrier, $q = q_u = 0$ and $q_r = q_{in}$. Therefore $\frac{d\,\delta_c}{dt} = \frac{q_{in}}{C_r}$, the setup increases. It leads to $q_u \neq 0$ so q_r decreases, the setup increases slowlier and slowlier. As soon as $\delta_c = R_u q_u$, the capacitor is charged, the setup has reached its maximum value.

2. Modeling R_u

R_u can be modeled by the Gauckler-Strickler formula mentioned in part V.B: $R_u = f\,q_u$ (the hydraulic resistance is proportional to the flow rate).

However it will be shown in part IX.C from experimental results that for a mild seaward slope, $R_u = f'\frac{1}{\sqrt{q_u}}$ and for a steep seaward slope $R_u = f''$. f, f' and f'' are friction coefficients.
The three cases are treated in the following.

3. Modeling R_{vf}

The undertow doesn't compensate totally the influx like in the purely 2D case, i.e. there is a net cross-shore discharge corresponding to $q_{in}(1-\alpha)$.

The set-up would then increase by $\frac{{U_c}^2}{g}\frac{h_c}{h_t}$ where U_c is the velocity over the barrier.

It can be approximated by $U_c = \frac{q_{in}(1-\alpha)}{H_c}$ since the wave drift occurs between the wave crest and the wave trough. the volume flux set-up becomes $\delta_{vf} = \frac{{q_{in}}^2(1-\alpha)^2}{g{H_c}^2}\frac{h_c}{h_t}$. Using the expression of q_{in} in Eq. V-4, we get:

$$\delta_{vf} = \frac{{h_c}^2}{h_t}\left(B_0\frac{H_c}{h_c} + 0.06\right)^2(1-\alpha)^2 \qquad \text{Eq. V-11}$$

δ_{vf} is in reality a part of δ_{mf}, but the two processes have been separated according to their dependency on α.

R_{vf} can then be expressed as $R_{vf} = -\frac{1}{2g\left(\frac{1+K_t}{2}\right)^2{H_i}^2}$.

4. Energy potential

We assume the steady state reached for the following, i.e. we don't take into account the capacitor.

The channel is opened by reducing $R_{channel}$.
δ_c then decreases to the value $R_{eq}q_{in}$ where $R_{eq} = \frac{R_u\,(R_{channel}+R_{vf})}{R_u+R_{channel}+R_{vf}}$.

We introduce the discharge fraction α so that $q_u = \alpha\, q_{in}$ and $q = (1-\alpha)\, q_{in}$, $0 \le \alpha \le 1$.

The dimensionless potential is defined by $P^* = \frac{P}{q_{in}\,\delta_{mf}}$

With $P = \delta\ q_c = \left(\delta_{mf} + \delta_c + \delta_{vf}\right)\ q_c$

Two dimensionless parameters are introduced: $\Gamma_c = \frac{\delta_{c1}}{\delta_{mf}}$, in which δ_{c1} is the continuity set-up when $\alpha = 1$ (i.e. 2D conditions); similarly $\Gamma_{vf} = \frac{\delta_{vf1}}{\delta_{mf}}$. The latter is weakly varying from one situation to another and can be approximated by $\Gamma_{vf} = 0.1$.

With the different modeling of R_u:

- If $R_u = f\, q_u$
  Then $\delta_c = f {q_u}^2 = f\, \alpha^2 {q_{in}}^2$

  So $P = \delta\, q_c = f\, \alpha^2(1-\alpha){q_{in}}^3 + \delta_{mf}(1-\alpha)q_{in} - R_{vf}(1-\alpha)^3{q_{in}}^3$

$$P^* = \Gamma_c\, \alpha^2(1-\alpha) + (1-\alpha) + \Gamma_{vf}(1-\alpha)^3 = \mathbf{(1-\alpha)(\Gamma_c\, \alpha^2 + 1 + \Gamma_{vf}(1-\alpha)^2)} \quad \text{Eq. V-12}$$

- With a similarity argument, $R_u = f' \frac{1}{\sqrt{q_u}}$ leads to

$$P^* = \Gamma_c \sqrt{\alpha}(1-\alpha) + (1-\alpha) + \Gamma_{vf}(1-\alpha)^3 = \mathbf{(1-\alpha)\left(\Gamma_c \sqrt{\alpha} + 1 + \Gamma_{vf}(1-\alpha)^2\right)} \quad \text{Eq. V-13}$$

- $R_u = f'' \frac{1}{\sqrt{q_u}}$ leads to

$$P^* = \Gamma_c\, \alpha(1-\alpha) + (1-\alpha) + \Gamma_{vf}(1-\alpha)^3 = \mathbf{(1-\alpha)(\Gamma_c\, \alpha + 1 + \Gamma_{vf}(1-\alpha)^2)} \quad \text{Eq. V-14}$$

Results are plotted on Figure V-4, Figure V-5 and Figure V-5.

We can clearly see a maximum in the potential as expected above. The higher the continuity set-up with respect to the momentum flux set-up, the higher the discharge fraction giving the highest potential.
It is compared with experimental results part IX.D.

5. Maximization of the potential

$\frac{dP^*}{d\alpha} = 0$ gives the highest potential. Only the two cases corresponding to real situations are treated.

Steep slope case: $\frac{dP^*}{d\alpha} = -3\Gamma_{vf}\alpha^2 + (6\Gamma_{vf} - \Gamma_c)\alpha + \Gamma_c - 3\Gamma_{vf} - 1 = 0$
The only solution with physical consistency is:

$$\alpha_{opt} = 1 - \frac{\Gamma_c}{6\Gamma_{vf}} + \sqrt{\left(\frac{\Gamma_c}{6\Gamma_{vf}}\right)^2 - \frac{1}{3\Gamma_{vf}}} \quad \text{Eq. V-15}$$

Mild slope case: $\frac{dP^*}{d\alpha} = -2\Gamma_c\sqrt{\alpha} - 1 + \frac{\Gamma_c}{2\sqrt{\alpha}} - 3\Gamma_{vf}\alpha^2 + 6\Gamma_{vf}\alpha - 3\Gamma_{vf} = 0$ which has no analytical solution and must be solved numerically. However it is reasonable to neglect the effect of volume forces, i.e. $\Gamma_{vf} = 0$. It is shown with experimental data in part IX.A.

We get $-2\Gamma_c\sqrt{\alpha} - 1 + \frac{\Gamma_c}{2\sqrt{\alpha}} = 0$ or with $X = 2\sqrt{\alpha}$: $X^2 + \frac{X}{\Gamma_c} - 1 = 0$ which has only one solution with mathematical consistency:

$$\alpha_{opt} = \left(\frac{\sqrt{1 + 4{\Gamma_c}^2} - 1}{4\Gamma_c} \right)^2 \qquad \text{Eq. V-16}$$

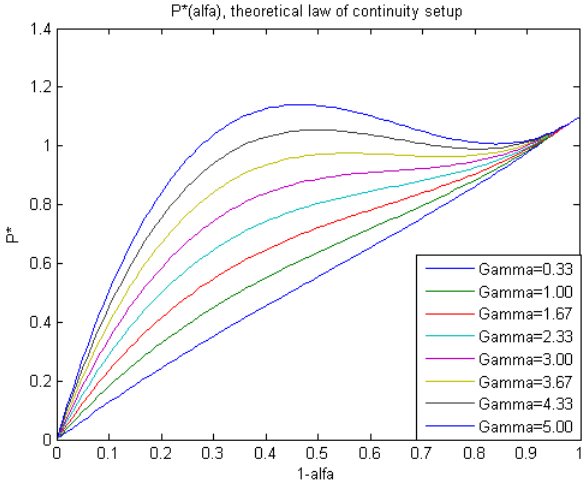

Figure V-4: Theoretical variation of the potential with the discharge fraction

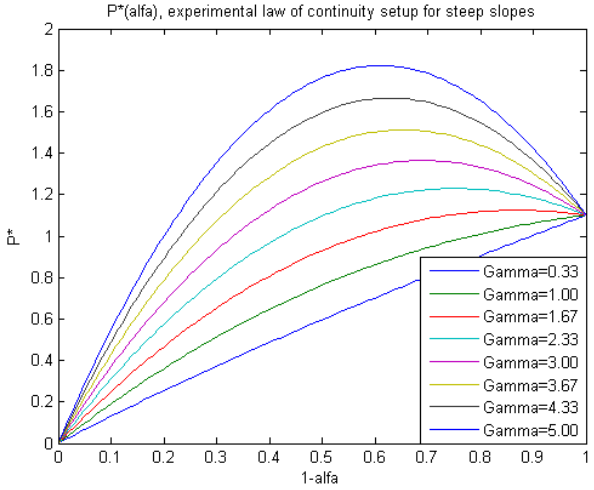

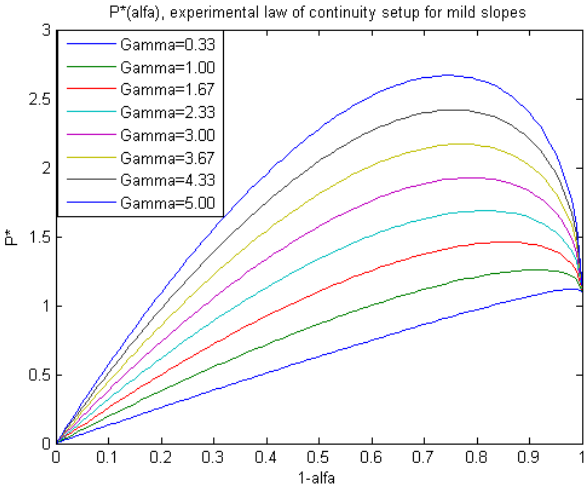

Figure V-5 & Figure V-6: Variation of the potential with the discharge fraction from experimental modeling of the hydraulic resistance over the barrier

VI. Experimental set-up

A. Wave tank

The experiments have been carried out in the student tank of the Marine Technology Institute of NTNU, Trondheim, Norway. Its small size allows quick and easy tests; it is perfect for this first experimental approach which does not need to be very accurate but quick and effective.

Tank characteristics:

- Length: 25 m
- Width: 2.5 m
- Depth: 1.0 m
- Wave maker: Single flap, hydraulically operated
- Maximum wave height: 0.3 m

- Wave period range: 0.25-3 s
- Maximum wave steepness: 1:8

B. Model

1. Generalities

The model is made of plywood with a waterproof coat. It was built in pieces in the laboratory of the Fluid Mechanics Institute of the Energy and Processes Department of NTNU. The last assembling tasks were done in the wave tank.

An overview of the model is presented on Figure VI-1. For a complete description of the experimental set-up with pictures, one is referred to appendices K and L.

2. Geometry

The scale of the physical model is Froude undistorted. It is generally the most appropriate for floating structures and open channel flows in general.

The scaling factor has been initially chosen as 1/40, which means that the 6 cm high planned incident waves corresponded to 2.40 m for full scale conditions.

Appropriate geometrical dimensions have been chosen by the help of the above-described analytical models.

3. Main features and global explanations

- *First bar:* A removable board was used to switch the slope between 1/2 and 1/8
- *Second bar:* It was removed for most of the tests because of the incapacity to measure the set-up due to too small depth
- *Crest submergence:* Varied by changing the still water level (filling or emptying the tank)
- *Trough submergence:* Varied by setting a board in the trough to lift the bottom
- *Gate:* It regulates the flow rate and indirectly the set-up
- *Test section:* The test section is a restriction in the channel to measure the velocity profile and thus the flow rate. It was far enough upstream, so the flow is not disturbed by the gate.
- *Seaward wave gauge:* It measures the incident wave height.
- *Shoreward wave gauge:* It measures the transmitted wave height and the wave set-up.

According to their longshore position, *generated waves* can:

- Continue to propagate freely between the sides of the structure and the walls of the tank
- Be dissipated and reflected on the wave absorber in front of the channel
- Be split in two parts in depth:
  - The deepest propagates under the structure and is partly reflected
  - The closest to the surface shoals, propagates toward the barrier and breaks

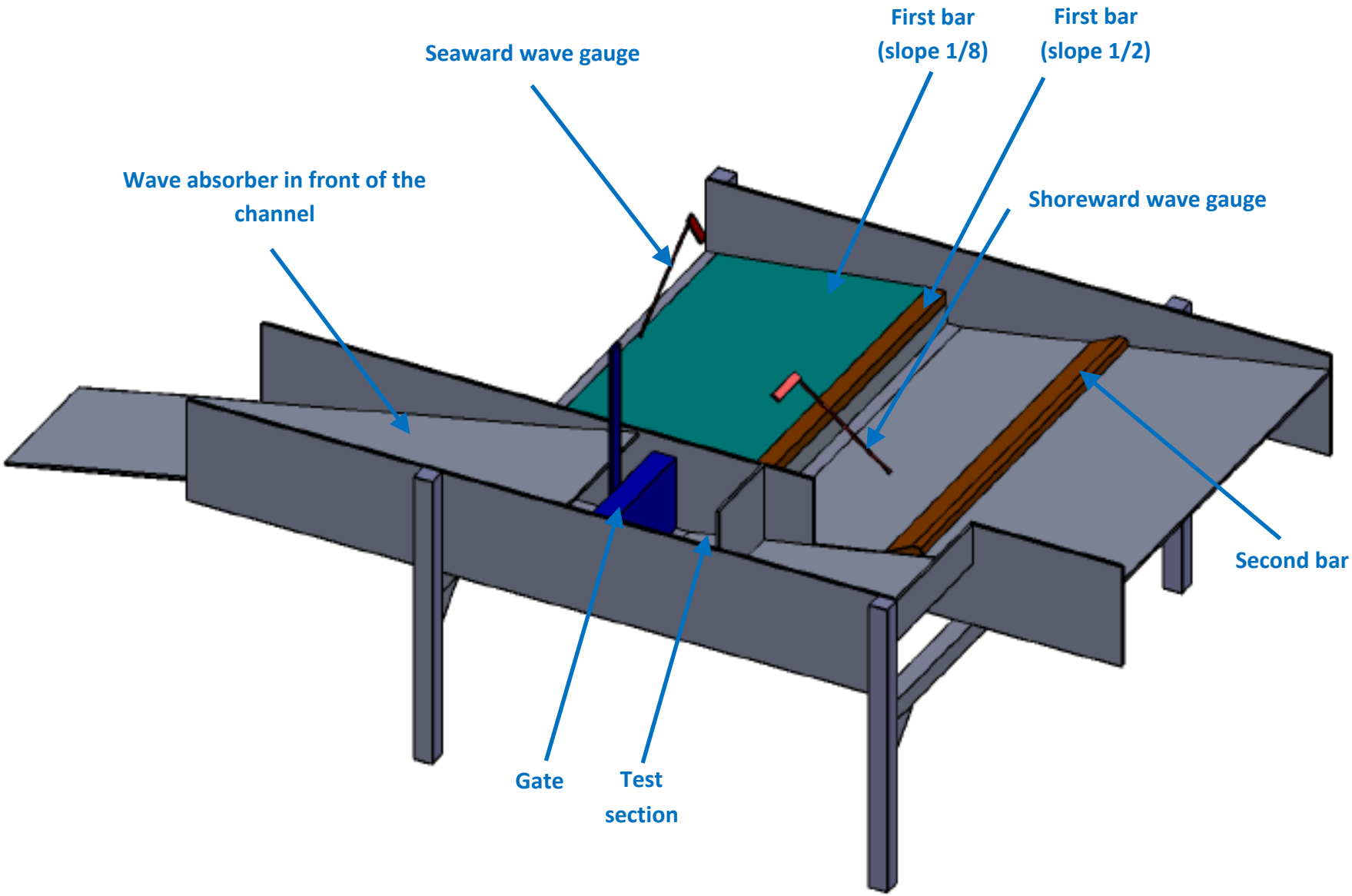

Figure VI-1: 3D Overview of the model

C. Measuring equipment

1. Waves

The waves were measured by two wave gauges of resistance type. The electrical resistance of the submerged tubes varies linearly with submergence. By the mean of an accurate calibration, one can convert the output electrical tension in surface elevation.

These gauges are sensible to temperature and dirt, and should be calibrated often. Since it was not very convenient in our case, and given that errors from other sources are far bigger (see part VII), it was just calibrated once.

Calibration was made by varying the water level (filling and emptying the tank).

The signal passes first through an amplifier, and is transmitted by Bluetooth to the computer. The cables between the gauge and the amplifier and between the amplifier and transmitter were kept the same for each gauge not to change the resistance after calibration.

The software used to capture the data was CATMAN MGC Reg 3.6 developed by MARINTEK. It needs in input the linear coefficient from calibration (see appendix A).

2. Velocity

The probe Vectrino© from Nortek AS was used. It is an acoustic Doppler probe which measures particle velocities from Doppler Effect. Acoustic waves are sent by four beams (see appendix K), reflected by particles in suspension in the volume of control, and captured by the receiver.

The volume of control is located 5 cm from the receiver. The probe does not need any calibration.

The rate of particles in suspension must be sufficient, otherwise acoustic waves are reflected by the walls and the probe gives unusable data. Therefore seeding is needed before the tests. It was done by raising the dust of the tank from the bottom to the surface and leading it to the channel.

Data is transferred through a cable to the computer.

The software Vectrino Plus 1.15 is included with the probe.

D. Test plan

1. 2D tests

The goal of 2D tests was first to check qualitatively the analytical model of Calabrese, i.e. to roughly confirm the dependency of the set-up on main parameters. At the same the empirical formula for wave transmission should be checked.

Secondly 2D tests were meant to provide the friction coefficient needed in the modeling of the continuity set-up in the model of Calabrese.

A list of completed test can be found in appendix G. The experimental procedure to get the variation of the set-up against input parameters is detailed in appendix F.

2. 3D tests

The 3D tests considered only one of the input configurations from 2D tests. The goal was to check the decrease in set-up as the flow rate in the channel increases.

The opening of the gate drives the discharge in the channel. For each opening the set-up is measured and the flow rate in the test section is partly measured, partly deduced from velocity measurements (see part IX.B).

The potential can then be calculated for each discharge in the channel, and the optimal value is deduced.

A list of completed test can be found in appendix H.

3. Additional tests

Additional tests were meant to bring complementary information on the set-up from secondary parameters. Most of them are not presentable because of too few data to overcome the scatter. Others are more or less beyond the scope of this survey. More details are available in appendix J.

VII. Note on uncertainties

A. Generalities

Uncertainty in measurement is extremely difficult to quantify. Some important sources like the motions of the structure will be quantified to show that results could be validated qualitatively.

However given the global uncertainty, from the model itself to the measurement methods, it is utopist to aim a quantitative study. Moreover the analytical model of the set-up is designed for engineering applications and gives a good order of magnitude, but we cannot expect an uncertainty below 20%. It is then pointless to compare quantitative experimental data to qualitative theoretical results.

As a consequence we shall furnish global order of magnitude of uncertainties, but no error bar figures on the graphs for the sake of simplicity and readability.

In 2D tests it is somehow compensated by the number of data. The difference in scattering between experimental and theoretical data gives a good idea on the precision error, i.e. how results from similar tests could vary.

BIAS errors, which are not revealed by the repetition of experiments, could be very huge too and are even more difficult to quantify.

B. Material restrictions limiting accuracy

The dimensions of the model were limited by both technical and financial means.

Mainly in order to allow wave shoaling avoiding wave reflection, a very long mild sloped beach would have been needed (more than 20 meters). Therefore the uniform depth of the tank, due to its main function to simulate offshore deep water waves, was not appropriate.

The length of the structure being limited, a compromise had to be found for:

- The depth of the seaward edge. It influences the amount of wave energy that propagates over and beyond the structure.
- The steepness and length of the incident slope seaward from the barrier. They influence the minimum steepness of the seaward slope of the barrier itself, and therefore the set-up.
- The steepness of the absorbing beach shoreward of the barrier. It influences wave reflection.
- The height of the upper edge of the absorbing beach. It determines the highest transmitted wave run-up and therefore the highest acceptable height of the transmitted wave.
- The width of the barrier crest. It influences the transmission coefficient and therefore the set-up.

These compromises induce a high uncertainty compared to related experiments found in the literature. Therefore no quantitative study is conceivable.

C. Example of uncertainty calculation

The incident wave height was significantly different from one test to another with the same generated conditions. The corresponding relative uncertainty would be: $\frac{\Delta H_i}{H_i}_{measured} = \pm 15\%$

Since we always use relative (dimensionless) variables with respect to the incident wave height like $\frac{h_c}{H_i}$, it would be crucial to know if this precision error comes from sources independent on the measurement device/location. If it does $\frac{h_c}{H_i}$ would keep a correct value, being calculated upon real incident conditions. If not (e.g. if the wave field is not uniform in the longshore direction, i.e. H_i varies depending on the longshore position of the probe), a big uncertainty would be created, and uncertainties on geometric parameters like h_c (±2%) would be negligible.

It is unfortunately not possible to check the nature of the uncertainty on H_i, it is therefore pointless to quantify uncertainty for all parameters.

D. Sources of uncertainty

The uncertainties influencing the results are of different natures (structure geometry, measurement devices…). The most important ones that have been quantified are:

- The heave motion of the structure, see appendix E.
- The calibration errors. If a strong incompatibility of data from one single test with existing data and theoretical model is found in the results, it can be from an error of calibration (default). This test is then removed.
- Wave reflection, see appendix E.
- Friction and head losses on the velocity. They are calculated in part IX.A and IX.B.

VIII. 2D results

A commented example of data acquisition by wave gauges is available appendix B.

A. Set-up as a function of barrier width and transmission coefficient

The method presented in appendix I is not accurate enough to predict a generated wave height keeping constant the width of the barrier $\frac{B}{H_i}$. The main reason for this was the motions of the structure under wave loads, which could significantly change the incident wave height.

It was then not possible to separate the parameters. Fortunately, $\frac{B}{H_i}$ came out not to influence significantly the set-up. It is shown on

Figure VIII-1, from which no law or tendency can be extracted.

In the same way, $\frac{B}{H_i}$ didn't seem to influence K_t (similar chaotic scatter to the one plotted

Figure VIII-1), though it should play a key role. As a consequence the empirical law from Van der Meer et al. (2005) underestimated the transmission coefficient K_t, in which is a key parameter. It is illustrated on

. The colors represent the wave period. It seems that K_t is underestimated for high wave periods ($T \geq 0.7s$) and over estimated for low periods.

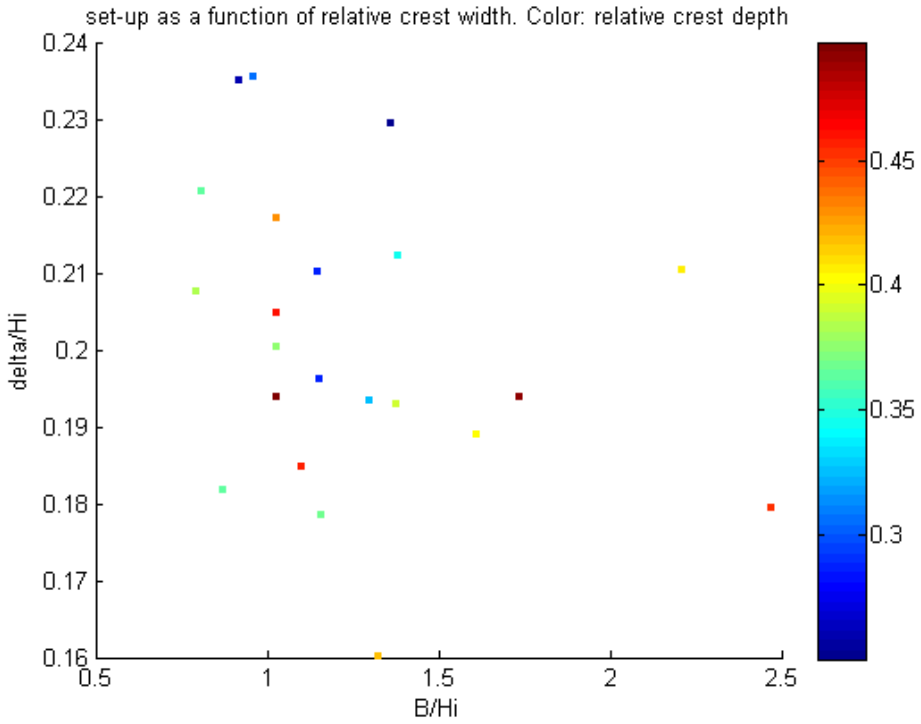

Figure VIII-1: Set-up against relative crest width. Colors represent the relative crest depth.

A reason for this could be the small values of $\frac{B}{H_i}$ used. The formula of Van der Meer et al. was designed to describe breakwaters protecting the coastline, and therefore having the lowest transmission coefficient as possible, i.e. a wide barrier ($\frac{B}{H_i} \geq 5$). Regarding the dependency upon the

wave period, it is more delicate. Either Van der Meer should have included it (or the wave steepness) in its formula; either the period creates a big uncertainty on the experimental results. Indeed it was observed that the wave was not uniform in the longshore direction, and a "gap" in the broken wave was sometimes observed close to the wave probe. It could have lead to higher or lower measured transmitted wave heights than the average one over the barrier. This phenomenon was strongly depending on the period, though no law has been sorted out.

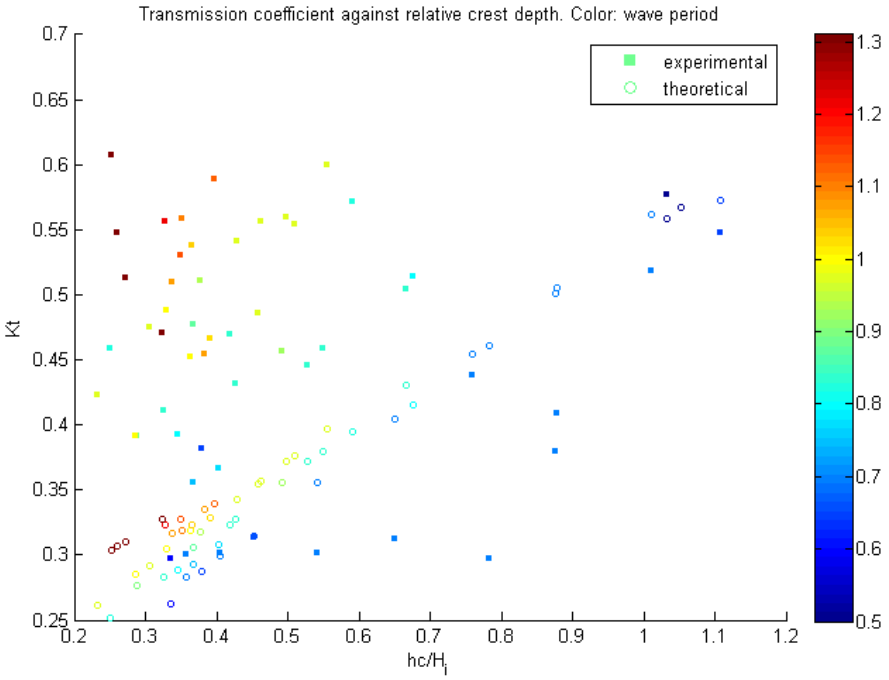

Figure VIII-2: Transmission coefficient against relative crest depth. The color scale represents the wave period.

B. Set-up as a function of relative crest depth for mild seaward slope

The results are plotted Figure VIII-3. We see a clear decrease of the set-up with the relative crest depth $\frac{h_c}{H_i}$. The difference between the experimental and theoretical results accounts for the continuity set-up.

For high values of $\frac{h_c}{H_i}$, we can notice a light overestimation of the set-up by the model of Calabrese. However we are interested in the lowest values of the set-up, i.e. $0.3 \leq \frac{h_c}{H_i} \leq 0.5$. The model is expected to be valid in this range.

C. Set-up as a function of relative crest depth for steep seaward slope

The results for a steep slope are plotted

Figure VIII-4. Like in the mild slope case, there is no major contradiction that could lead us to invalidate the theoretical model, but there is still an overestimation for high values of $\frac{h_c}{H_i}$.

From both steep and mild configurations, we can conclude that the momentum flux set-up decreases more sharply with the relative crest depth than what the analytical model predicts.

The processes over the barrier in the steep slope and mild slope cases were quite different from each other.

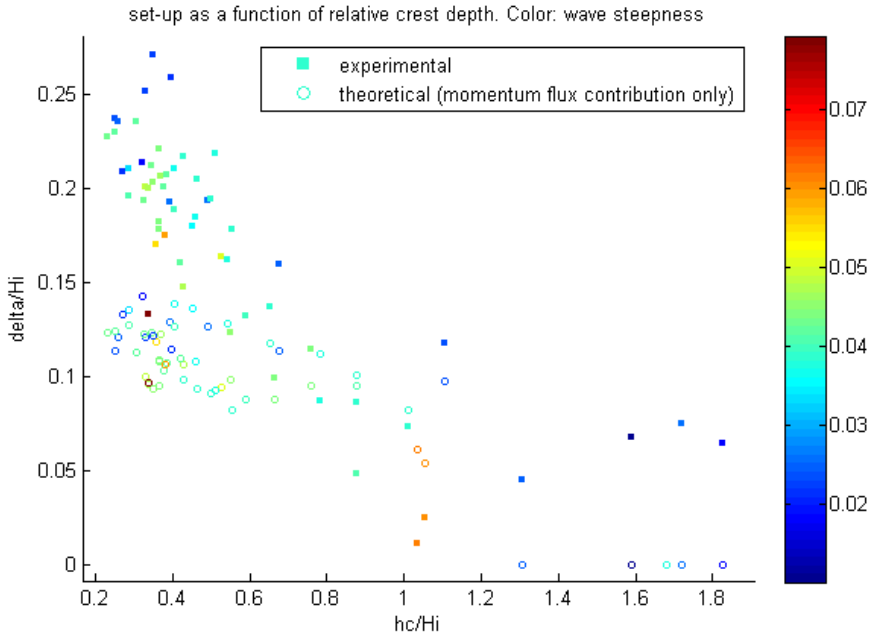

Figure VIII-3: Relative set-up against relative crest depth for mild slope. Colors represent the wave steepness.

Observations of the processes over the barrier during the experiments were the following:

- When the wave and the surface roller are propagating shoreward, the water level increases behind the barrier.
- When the wave is subsiding, a bore is created, similarly to a dam-break.
- A strong current directed seaward takes place. It is visible to the naked eye. The water level decreases.
- The current vanishes as the wave comes back.

The difference between time averaged and time varying mass conservation is illustrated on Figure VIII- and Figure VIII-.

This difference has an effect on the undertow and will change the behavior of the continuity set-up in 3D configuration (see part IX.A). It has also a consequence on the 2D continuity set-up through the nature of the friction that creates this set-up (see part IX.C).

The interaction between the bore and the incident wave could have a strong influence on the momentum balance. We can mention the reflection of the wave by the undertow, including the phenomenon so-called “Bragg reflection” (see Peregrine (1976), Mc Kee (1994)), occuring with periodic currents like it is the case. The wave has also to pass the hydraulic jump at the bore.

These considerations are beyond the subject here, but the momentum flux set-up might be strongly affected by these phenomena, therefore the theoretical results are somewhat more uncertain than they already were for the mild slope case.

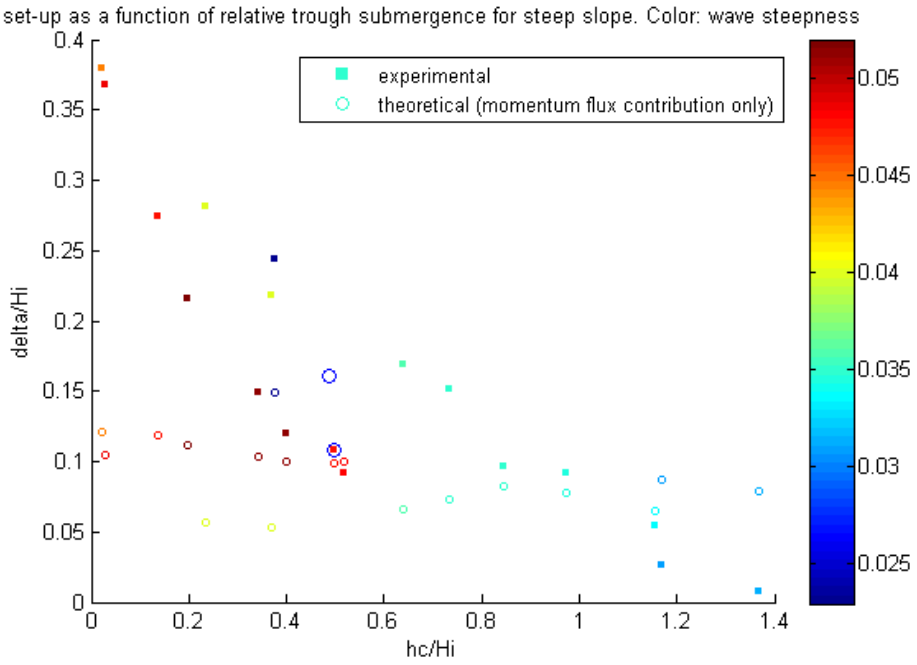

Figure VIII-4: Relative set-up against relative crest depth for steep slope. Colors represent the wave steepness

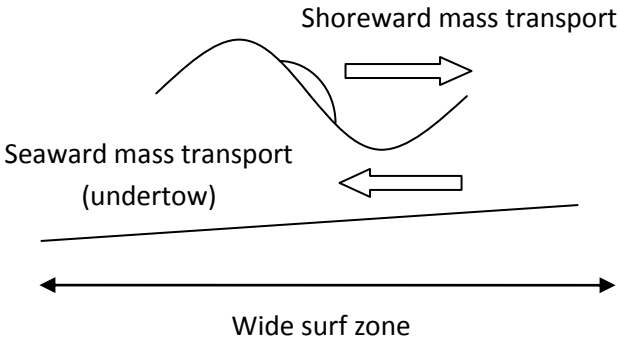

Figure VIII-5: Assumed Cross-shore mass conservation in the theoretical model

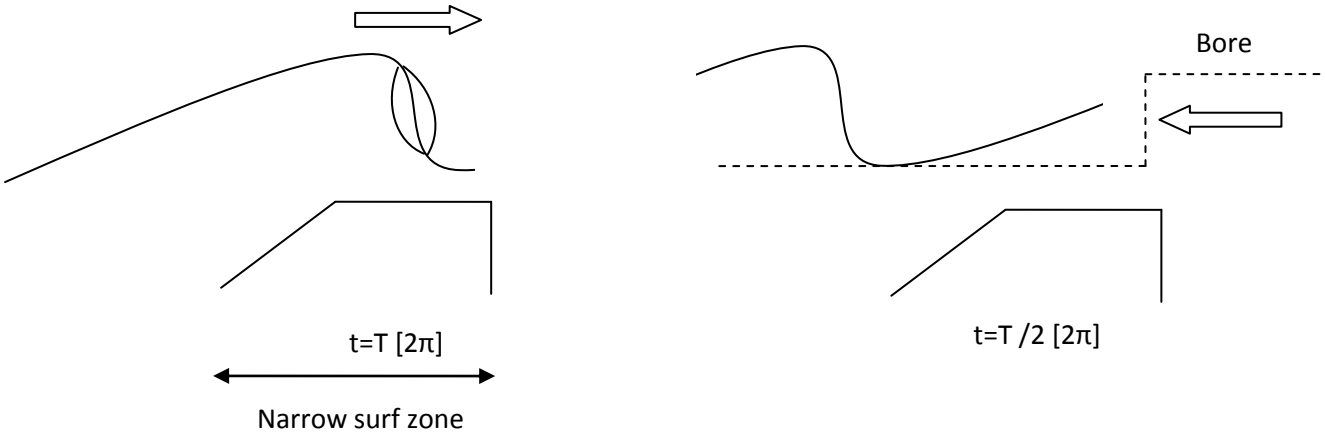

Figure VIII-6: Cross-shore mass conservation in the experiments case with steep seaward slope

D. Wave breaking criterion

Note that on Figure VIII-3, the analytical model predicts no set-up for high values of $\frac{h_c}{H_i}$, i.e. no breaking. Experimental results show that breaking occurs, or at least a phenomenon which dissipates the energy of the wave. The model is consequently not valid for such values of $\frac{h_c}{H_i}$.

E. Friction coefficient

For a mild slope the friction coefficients calculated from $f = \frac{\delta_c}{q_{in}^2}$ have been plotted Figure VIII-5.

We notice an unclear variation with $\frac{h_c}{H_i}$, which can be explained by the interdependence of the hydraulic diameter, $\frac{h_c}{H_i}$ and δ_c. However the chaotic behavior of f with $\frac{B}{H_i}$ leads us to conclude that the classical friction, from roughness and hydraulic diameter, does not play a major role here compared to turbulent eddy viscosity from wave breaking.

This is in agreement with the work of Nelson (1996) who showed that the sand grain equivalent roughness for the undertow over a coral reef has no obvious link with the real roughness but must be deduced experimentally.

For this small scale model, the average value of f of $400\ m^{-3}\ s^2$ is retained.

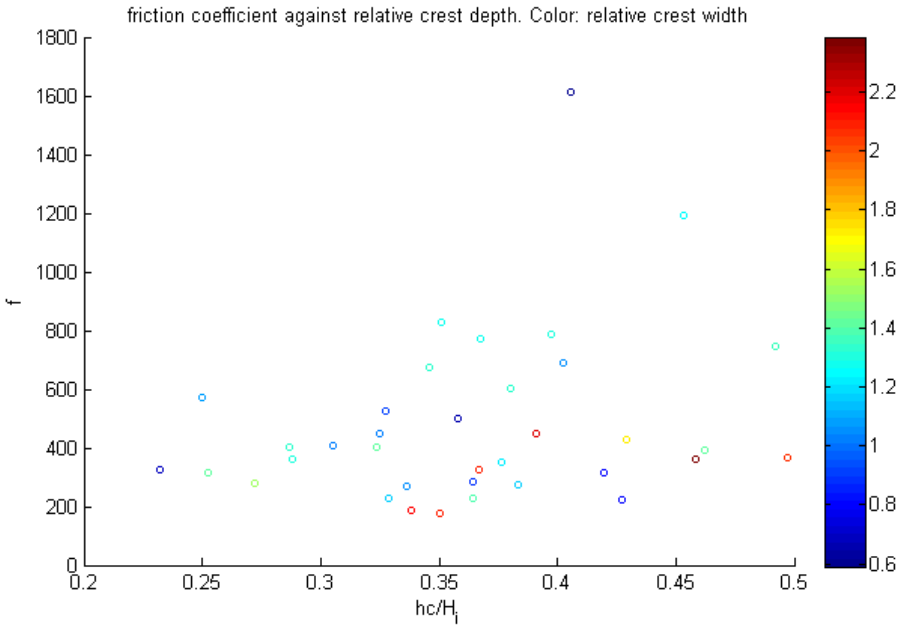

Figure VIII-5: Friction coefficient against relative crest depth. Colors represents relative crest width

F. Set-up as a function of wave steepness

The color scale in Figure VIII-3 represents the influence of wave steepness. It is difficult from this figure to draw conclusions on the influence of the wave steepness on the set-up. Nevertheless, a little tendency of a high $\frac{\delta}{H_i}$ with a low $\frac{H_i}{L_i}$ for a constant $\frac{h_c}{H_i}$ can be seen.

It is depicted more directly on Figure VIII-6. The experimental set-up rises more sharply as $\frac{H_i}{L_i}$ decreases than the analytical one. It seems to be in agreement with the relation found analytically stating that both δ_{mf} and δ_c are proportional to $\frac{H_i}{L_i}$ at a power between -½ and -1.

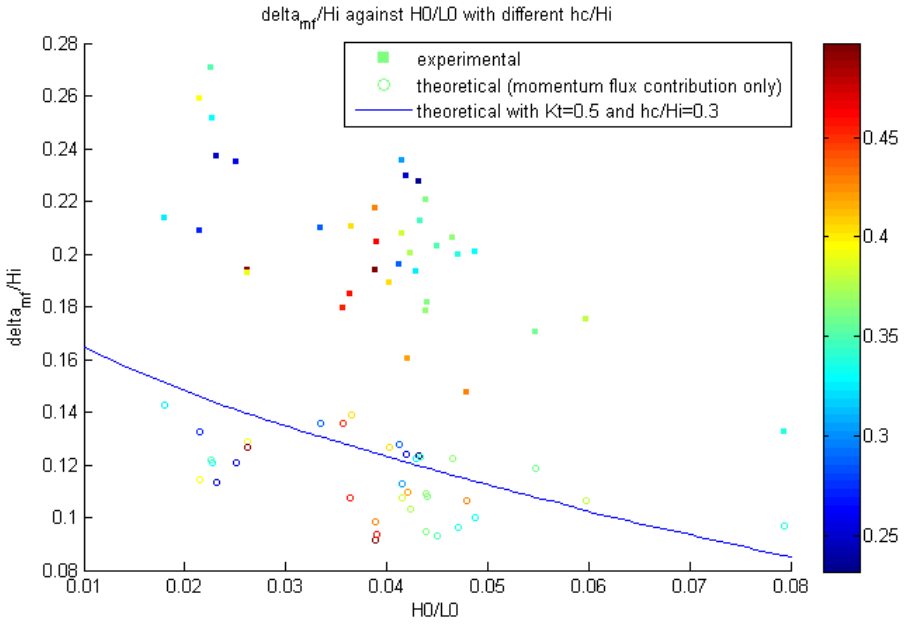

Figure VIII-6: Relative set-up against wave steepness. Colors represent the relative crest depth.

G. Influence of the trough depth

Figure VIII-7 shows the set-up as a function of $\frac{h_c}{H_i}$ with two values of $\frac{h_t}{H_i}$. It is hazardous to put two and two together with such few data, but we can note a general tendency of lower set-ups with lower trough submergence.

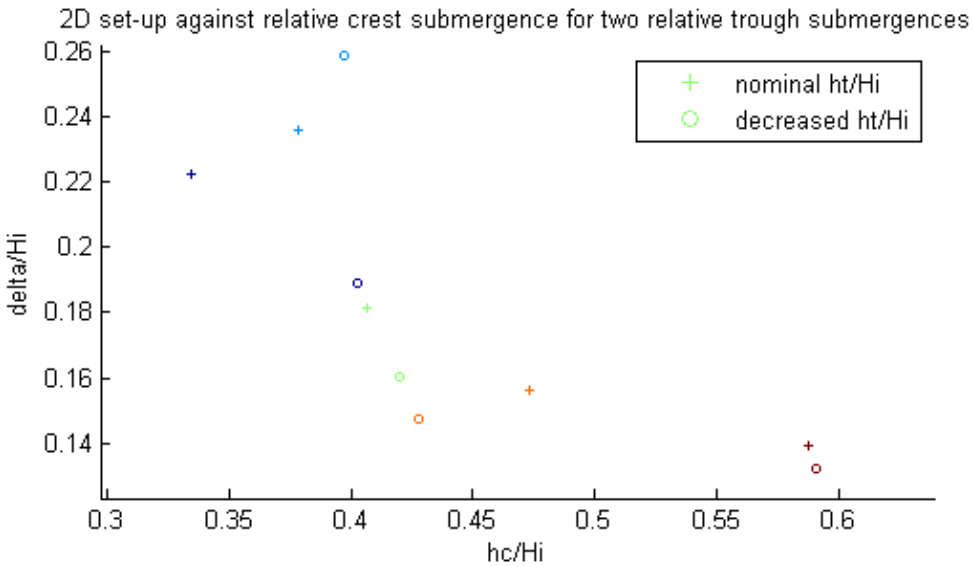

Figure VIII-7: Influence of relative trough depth. Colors are only meant to differentiate the results.

This tendency is in agreement with the model of Calabrese for this range of transmission coefficients (see part X.B for details).

H. Conclusions of 2D experiments

- Uncertainties disallow us to draw thorough conclusions

- The analytical model is hoped valid in the range of interest $0.3 \leq \frac{h_c}{H_i} \leq 0.5$
- The analytical model is expected to be more accurate for mild slopes than steep slopes
- The empirical formula for the transmission coefficient is not appropriate
- $\frac{B}{H_{i_i}}$ has no influence on the set-up in the range of values used in the experiments
- The processes driving the undertow are fundamentally different for steep and mild slopes
- Considering the same value of the total set-up, the continuity contribution is higher for steep slopes; the momentum flux contribution is higher for mild slopes.
- δ_{mf} and δ_c are proportional to $\frac{H_i}{L_i}$ at a power located between -1/2 and -1.
- The friction factor relative to the undertow for mild slopes has been found for this experimental set-up. It is not possible to extrapolate it easily to other situations with different barrier geometry and roughness.
- The higher the trough depth, the higher the set-up

IX. 3D Results

An example of velocity data acquisition is presented in XII.C.

A. Set-up calculation

1. Experimental results

The set-up as a function of the gate opening is depicted Figure IX-1 and Figure IX-2, for steep and mild slopes.

An exponential decay function appears clearly and has been interpolated. It gives:

$$\begin{cases} \frac{\delta}{H_i}(d^*) = 0.06 + e^{-6.7d^*-1.75} & steep\ slope \\ \frac{\delta}{H_i}(d^*) = 0.10 + e^{-4.3d^*-2.45} & mild\ slope \end{cases}$$

The left hand term corresponds to the asymptote when $d^* \to \infty$, and is normally equal to the momentum flux setup, though there is a significant uncertainty (see part VII).

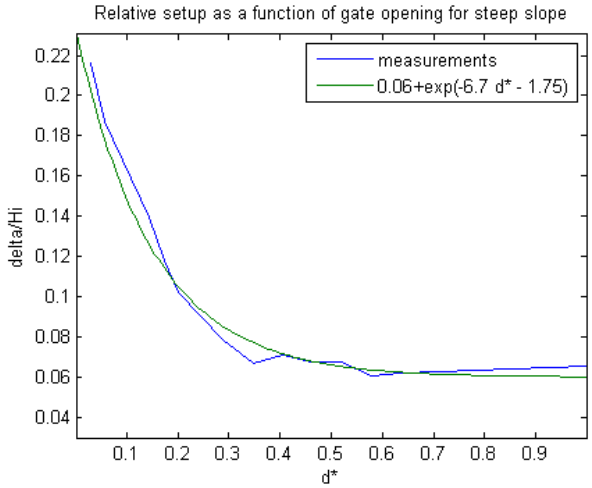

Figure IX-1: Set-up against gate opening for steep slope and interpolation

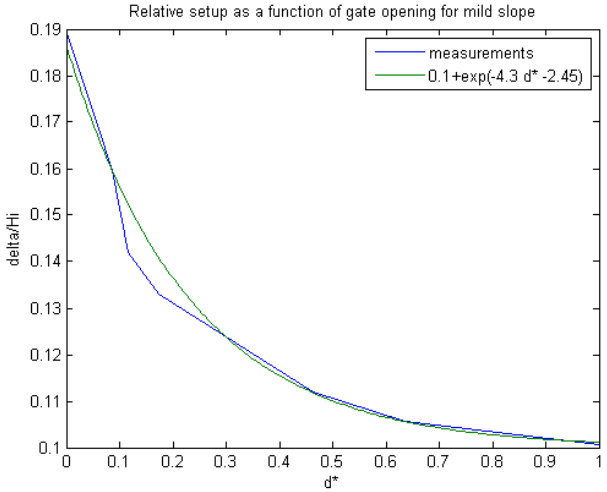

Figure IX-2: Set-up against gate opening for mild slope and interpolation

The incident wave height was varying from one test to another. It is shown Figure IX-3 and Figure IX-3 together with the transmission coefficient. It was partly caused by the precision error, but also by the undertow which can modify the intensity of wave breaking and also the incident wave field (Svendsen & Hansen (1987)). It should also be noted that unlike 2D tests, reflected waves from the structure via the wave maker were not avoided.

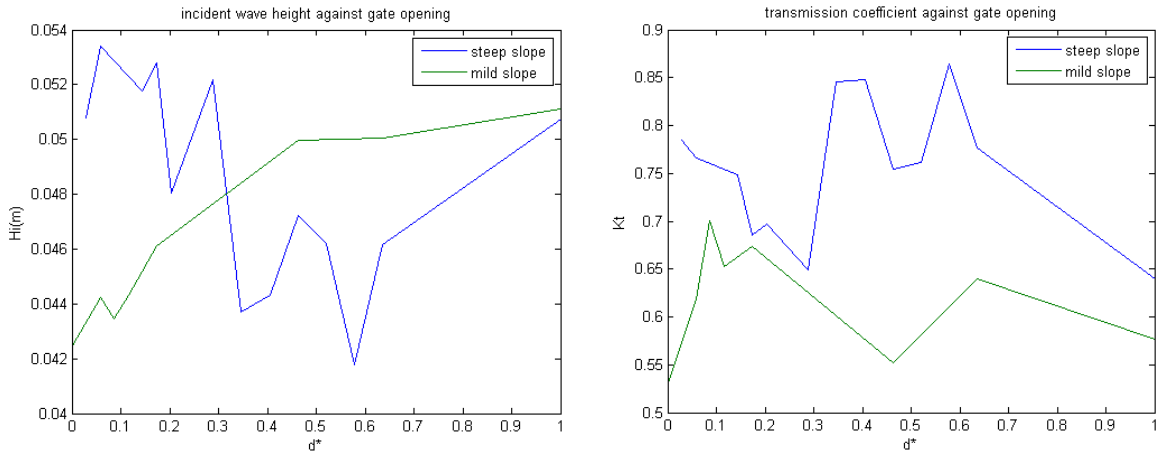

Figure IX-3 & Figure IX-4: Incident wave height (left) and transmission coefficient (right) for the tests presented Figure IX-1 and Figure IX-2

For the following calculations, the mean values of H_i and K_t have been used, i.e.

$$\begin{cases} H_i = 4.84\ cm & steep\ slope \\ H_i = 4.65\ cm & mild\ slope \end{cases} \text{ and } \begin{cases} K_t = 0.62 & steep\ slope \\ K_t = 0.76 & mild\ slope \end{cases}$$

2. Comparison with theory

From above, we have $\frac{h_c}{H_i} = 0.30$ for both cases and $\begin{cases} \frac{H_i}{L_i} = 0.063 & steep\ slope \\ \frac{H_i}{L_i} = 0.060 & mild\ slope \end{cases}$

The momentum flux set-up has been calculated with the analytical model:

$$\begin{cases} \frac{\delta_{mf}}{H_i} = 0.080 & steep\ slope \\ \frac{\delta_{mf}}{H_i} = 0.088 & mild\ slope \end{cases}$$

We notice that the analytical model underestimates the momentum set-up for mild slopes, but overestimates it for steep slopes.

3. Volume forces

From part V.E, $\frac{\delta_{vf}}{H_i}(\alpha = 0) \cong \begin{cases} 0.0024 & steep\ slope \\ 0.0022 & mild\ slope \end{cases}$

It does not explain the difference. The effect of volume forces could be neglected as suggested above.

4. Head losses due to friction

One has also to take into account the friction behind the barrier induced by the flow toward the channel. This produces head losses, which has to be compensated by an increase of the continuity set-up, even more when the gate is fully opened. Therefore the measured value for $d^* = 1$ is not exactly the momentum flux set-up.

Wave-current friction calculations are refered to Fredsøe & Deigaard (1992).

We make the assumption that the wall is hydraulically smooth, which seems reasonable considering the material (waterproof coat covering plywood) and the small velocities. It is also assumed that the waves dominate the current in the boundary layer (see part V.B).

The logarithmic law for the velocity profile for a smooth bottom with current only gives (from Fredsøe & Deigaard (1992)):

$$\frac{u(z)}{U_f} = 5.7 + \frac{1}{\kappa} ln\left(\frac{z\,U_f}{\nu}\right) = \frac{1}{\kappa} ln\left(9.8\,\frac{z\,U_f}{\nu}\right) \qquad \text{Eq. IX-1}$$

U_f is the friction velocity, κ is the Von Karman constant taken as equal to 0.4, z is the upward vertical coordinate and ν the kinematic viscosity.

Fredsøe & Deigaard gives the velocity profile for a wave-current boundary layer and a rough bed. Based on a similarilty argument, the corresponding relation for a smooth bed is:

$$\frac{U}{U_{fc}} = \frac{1}{\kappa}\frac{U_{fc}}{U_{fc}+U_{fw}} \ln\left(9.8\,\frac{z\,U_{fc}}{\nu}\right) \qquad \text{Eq. IX-2}$$

Where U_{fw} and U_{fc} are the friction velocities from waves and current.

$U_{fw} = u_{t\,b}\sqrt{\frac{f_w}{2}}$ with $u_{t\,b}$ the amplitude of the wave particle velocity in the trough, and f_w the wave friction factor calculated by the mean of equation Eq. V-6 (from Fredsøe & Deigaard (1992)). The equivalent sand grain roughness k_N should be determined experimentally since the bed is not uniform and presents imperfections from construction. Here we shall use the values for a smooth material: $k_N < 0.03\ mm.$

We know the mean velocity in the depth at an alongshore coordinate $y^* = \frac{y}{L_{barrier}}$ from

$$\overline{U} = \frac{Q_{in}}{S} y^* \qquad \text{Eq. IX-3}$$

since the alongshore discharge is increasing linearly toward the channel.

A_{trough} is the cross section of the trough. For the sake of simplicity we take an equivalent rectangular cross section with the same area as A_{trough} so that $A_{trough} = h_t * \Delta x_{\text{eq}}$. The flow is then assumed to be uniform over Δx_{eq}.

From Eq. IX-1, $\overline{U} = \frac{1}{h_t}\int_0^{h_t} U\,dz = \frac{1}{h_t}\int_0^{h_t} \frac{1}{\kappa}\frac{{U_{fc}}^2}{U_{fc}+U_{fw}} \ln\left(\frac{z\,U_{fc}}{\nu}\right) dz$ Eq. IX-4

We can then get U_{fc} for each y^* solving Eq. IX-3=Eq. IX-4 by iterations. We get therefore the bottom friction $\tau_b = \rho {U_{fc}}^2$. We can also check the assumption of a hydraulically smooth bed calculating the equivalent sand roughness Reynolds number:

$$k_N^+ = \frac{k_N U_{fc}}{\nu}$$

With the upper bounds of k_N and U_{fc} we get $k_N^+ = 1.4 \leq 5$, so the regime is hydraulically smooth.

We finally deduce the head losses from friction $\Delta\delta$ from energy conservation:

$$\rho g h_t \frac{\Delta\delta}{L_{barrier}} = \int_0^1 \tau_b \, dy^* \qquad \text{Eq. IX-5}$$

Numerical calculations give an order of magnitude of $\frac{\Delta\delta}{H_i}$ of 10^{-5}, i.e. very small compared with the other contributions of $\frac{\delta}{H_i}$. The effect of friction can therefore be neglected.

The effect of wave breaking hasn't been taken into account. It adds turbulence in a significant way and changed the shear stress. It is however hoped that its effect doesn't increase the friction to an order of magnitude as high as 10^{-3}, i.e. multiply the non-breaking case by more than 100, which seems reasonable.

5. Conclusions on analytical and experimental results for the momentum flux set-up

The relative errors between the experimental and analytical results are overestimation as high as 37% for the steep slope case and an underestimation of 10% for the mild slope case. Such a discrepancy was expected for mild slopes, but is quite surprising for steep slopes.

Indeed the model of Calabrese is designed for breakwaters, i.e. steep slopes, though it is **theoretically** applicable to mild slopes. It has been validated by 4 data sets, with a seaward slope ranging between $\frac{1}{3}$ and $\frac{1}{2}$.

The discrepancy for steep slope can be explained by the very simplified modeling of the reflection coefficient. Given the high transmission coefficient observed, the reflection would have been weaker than planned and the calculated set-up much higher.

It is also probable that the difference for steep slope comes from uncertainties in the measurement (BIAS error), particularly from wave reflection. From appendix E it could induce an error of 20% for mild slopes and 10% for steep slopes. It doesn't change from one test to the other since it depends only the wave period. Therefore it is hazardous to draw conclusions only with one wave period like it is the case.

6. Experimental determination of Γ_c and f

From equation XX, $\Gamma_c = \frac{\delta_{c\,1}}{\delta_{mf}}$. Then $\Gamma_c = \frac{\delta(\alpha=1)-\delta(\alpha=0)+\delta_{vf}(\alpha=0)}{\delta(\alpha=0)-\delta_{vf}(\alpha=0)} = \begin{cases} 2.93 \; steep\; slope \\ 0.98 \; mild\; slope \end{cases}$

In the mild slope case, the friction factor can be calculated:

$f = \frac{\delta_{qdm}\,\Gamma_c}{{q_{in}}^2} = 400\, m^{-3}s^2$. It is in perfect agreement with the 2D results.

7. Applicability of the model of Bellotti for 3D set-up

As suggested in part V.C, the model of Bellotti (2004) has been used to check its ability to predict the 3D set-up as a function of the ratio of the section areas in the channel and over the barrier.

The area over the barrier has been modeled by $A_{barrier} = H_i * L_{barrier}$ and the area in the channel by $A_{channel} = L_{gate} * d$ in which L_{gate} is the width of the channel at the gate.

The two parameters μ and C_v are needed to calibrate the model. Bellotti showed that the friction factor μ doesn't play a significant role and should be neglected given its approximate modeling.

The head loss coefficient C_v is normally close to 0.6 for flow constrictions, but first it is quite different here because of the elbow and the diaphragm, secondly it is not expected to have a physical meaning but only to calibrate the model.

The results are plotted Figure IX-5. It is clear that $C_v = 0.6$ is far from the reality. Whatever C_v the predicted value for $d^* = 0$ is much too low compared to experimental results. We may consider that the model of Bellotti is applicable to the continuity set-up only and not the entire set-up. Then if we add the momentum flux set-up and choose a very high head loss coefficient ($C_v = 9$) the correlation is good for $d^* \geq 0.1$ or $\frac{A_{channel}}{A_{barrier}} \geq 0.13$. The model needs however to be refined for low values of $\frac{A_{channel}}{A_{barrier}}$.

The reason why Bellotti's model is not able to predict the momentum flux set-up can be explained by its strong dependency on the trough depth h_t. If h_t is higher than h_i the model crashes, and if h_t is only slightly lower than h_i it gives inconsistent results like it is the case.

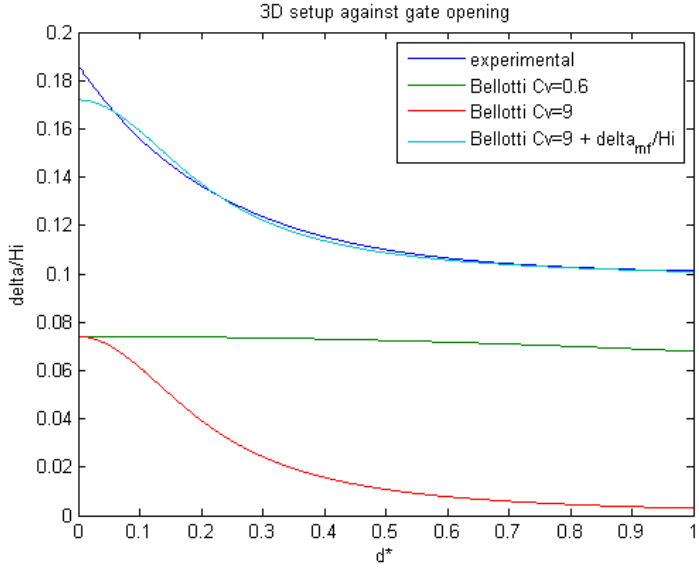

Figure IX-5: 3D set-up from experiments and Bellotti's model

B. Flow rate calculation

1. Velocity profile

The experimental procedure planned initially assumed a known velocity profile in the test section. Indeed it was expected to be logarithmic from the walls and the bottom. A simple observation of the flow from the trough behind the barrier to the channel was sufficient to show that it was not the case. As shown on Figure IX-6, The 90° elbow induced higher velocities on the outer part of the test section than on the inner part. The flow was indeed concentrated close to the outer wall.

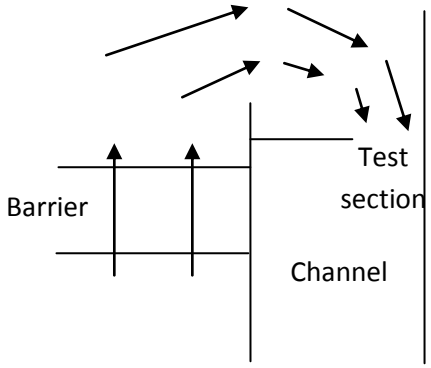

Figure IX-6: Top view of the low upstream from the test section.
Arrows represent velocity amplitude along streamlines.

Moreover, large eddies created by the structure geometry were observed, leading to a non-logarithmic velocity profile in depth.

As a consequence, the number of measuring points needed to calculate the flow rate was much higher than planned. For an accurate measurement, a complete flow mapping would have been necessary for each gate opening. This corresponds to more than 50 measuring points per opening. It was not conceivable to do such a tedious work within this project, considering the limited accuracy of the other measurements/analytical analyses.

2. New test plan

To calculate the flow rate Q for each value of gate opening d, the procedure was the following:

1. Perform a complete flow mapping for a fully opened gate. It was not needed to be very accurate considering the accuracy of the next steps: ca. 60 measuring points corresponding to 15 transversal positions y and 4 depth z (the 4^{rth} depth was added after the first results by necessity). The seaward slope of the barrier is steep.
2. Calculate the flow rate for a fully opened gate
3. Check if the velocity profile in the transversal direction was similar for another value of d (flow mapping at only one value of z)
4. Measure the velocity at 3 values of z and 2 values of y for each d
5. Calculate the ratio of the velocities measured in 4. over the corresponding ones measured in 1.
6. Assuming that the velocity profile kept the same shape in both directions, the flow rate at one single value of d would be the one calculated in 1. times the mean value of the ratios calculated in 5.
7. With a similarity argument the flow rate is calculated for a mild slope. It is assumed that the profile is not changing with the seaward slope of the barrier.

3. Flow mapping for a fully opened gate

Figure IX-7 shows the velocity profile in the transversal direction, at different depth. The following dimensionless parameters are used:
$y^* = \frac{y}{B_{ts}}$, $z^* = \frac{z}{h}$, $d^* = \frac{d}{d_{max}}$. $B_{ts} = 0.194\ m$ is the width of the test section, $h = 0.105\ m$ the depth at the test section, averaged over d^*, and $d_{max} = 0.173\ m$ is the depth at the gate.

Adding the no-slip conditions on the walls, a polynomial interpolation has been done in Matlab in two pieces: One for $0 \leq y^* \leq 0.95$ and one for $0.95 \leq y^* \leq 1$. Care has been taken to conserve the continuity in the function.

We confirm the above-mentioned statements, i.e. the velocity U is much higher close to the outer wall (y^* close to 1). In this region a condition on $\frac{\partial U}{\partial y}$ has been added in the interpolation to model properly the profile.

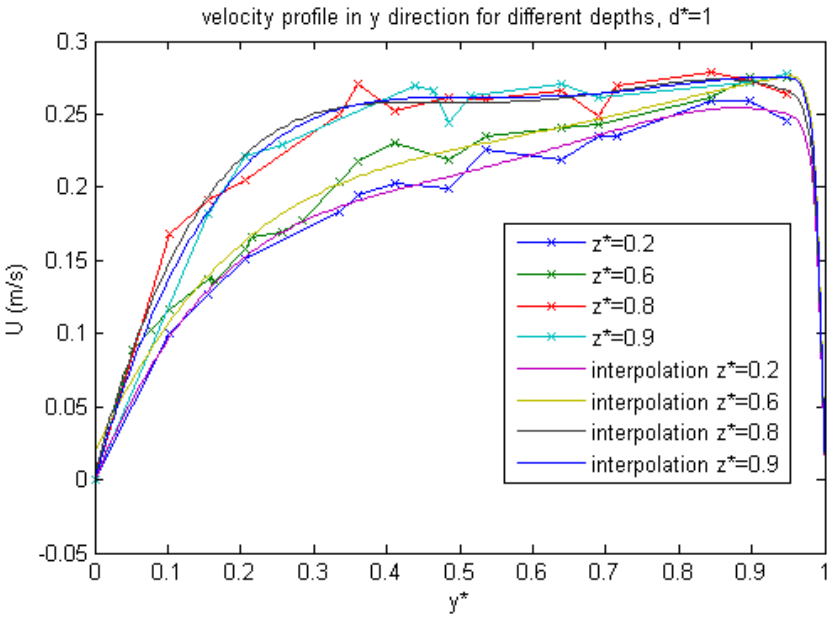

Figure IX-7: Measured values and interpolated velocity profiles in the transversal direction at different depth.

From the interpolated functions along y^* at 4 values of z^*, we can interpolate the profile in the z direction, giving the 3D profile plotted Figure IX-8. A no slip condition and a condition on a large $\frac{\partial U}{\partial z}$ at the bottom have been added as well as an additional condition at the surface.

The latter assumes that $U(z^* = 0) = U(z^* = 0.2)$ and $\left(\frac{\partial U}{\partial z^*}\right)_{z^*=0} = 0$.

4. Calculation of the flow rate

From the 3D mapping it is easy to deduce the flow rate: $Q = \sum_{maped\ area} U({y^*}_i, {z^*}_j)$
It gives $Q_{d^*=1} = 0.0042\ m^3/s$

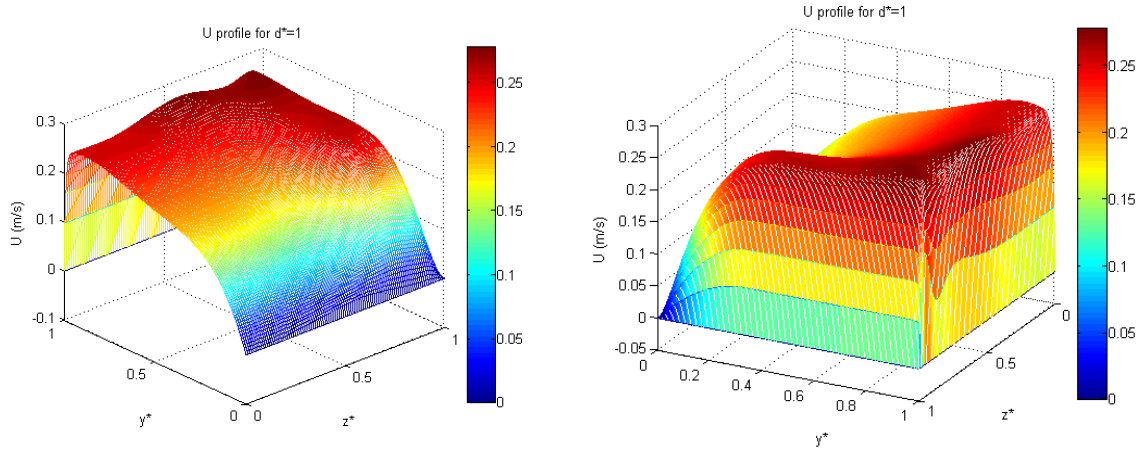

Figure IX-8: 3D velocity profile

5. Transversal velocity profile for a partially closed gate

The velocity profiles along y^* for $z^* = 0.6$ and $d^* = 0.29$ are plotted Figure IX-9, together with the corresponding profile for $d^* = 1$.

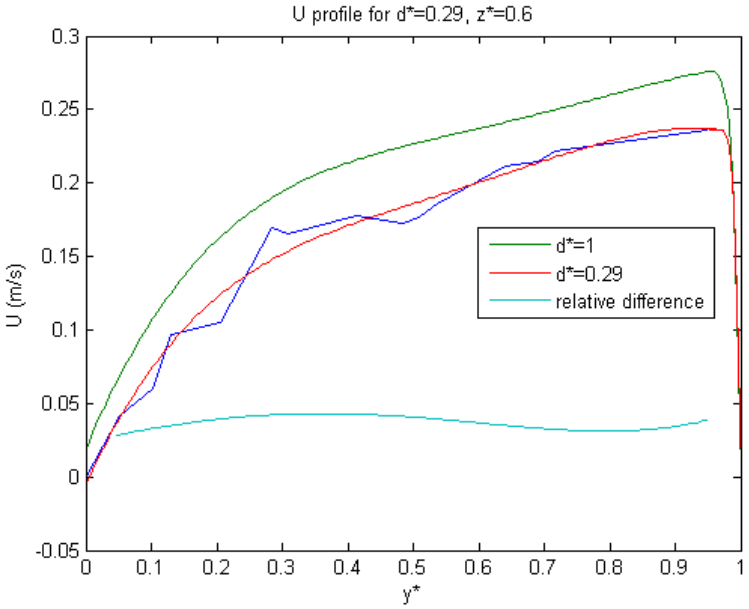

Figure IX-9: Velocity profile in the transversal direction for $z^* = 0.6$

As expected the velocity profiles are similar. The difference can be considered as constant, so that if we have only one measuring point at a given depth, we can deduce the transverse profile at this depth.

6. Measuring velocities for all values of d

For more accuracy two values of y^* have been used: $y^* = 0.36$ and $y^* = 0.95$. The second one appeared not to be the best choice since the profile is varying in the near-wall region. Results are plotted on Figure IX-10 and Figure IX-10. We can see that for $y^* = 0.36$ the profile stays the same

while d is changing, it is not really the case for $y^* = 0.95$, particularly for d^* close to 1.

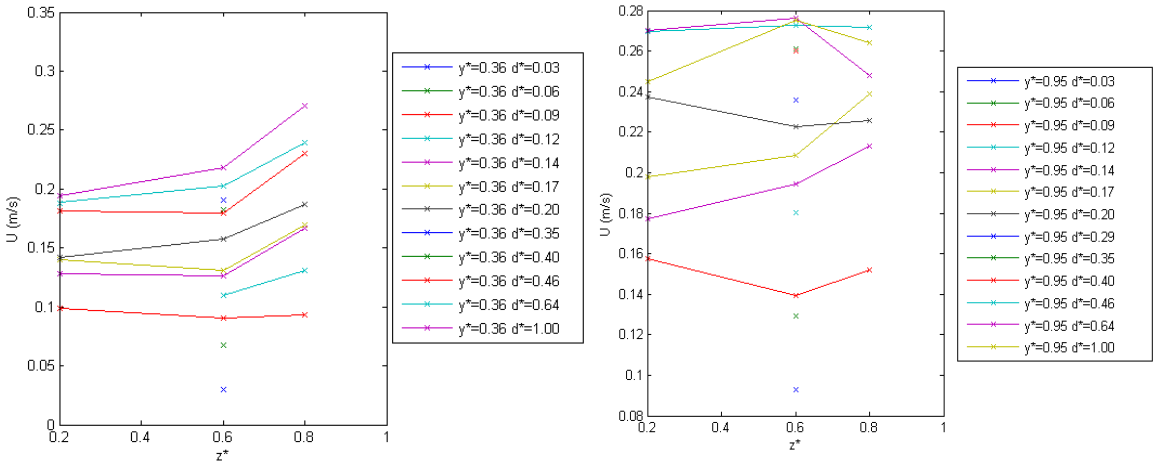

Figure IX-10 & Figure IX-11: velocity profiles in the z direction for $y^* = 0.36$ (left) and $y^* = 0.95$ (right) for a range of values of d^*

7. Velocity ratios

For each value of y^*, the mean value of the ratios $\frac{U_j(d^*)}{U_j(1)}$ is calculated. It is then averaged over y^*.

The mean ratio used in the calculation of the flow rate is therefore:

$$\overline{\left(\frac{U(d^*)}{U(1)}\right)} = \frac{\sum_{i=1}^{ny^*}\sum_{j=1}^{nz^*}\frac{U_{ij}(d^*)}{U_{ij}(1)}}{ny^* * nz^*}$$

With $ny^* = 2$ and $nz^* = 4$

8. Q as a function of d for a steep slope

We can calculate the flow rate for any d^*: $Q(d^*) = Q_{d^*=1} * \overline{\left(\frac{U(d^*)}{U(1)}\right)}$

The results are plotted Figure IX-12. The variation of $Q(d^*)$ seems to be a logarithmic function which has been interpolated.

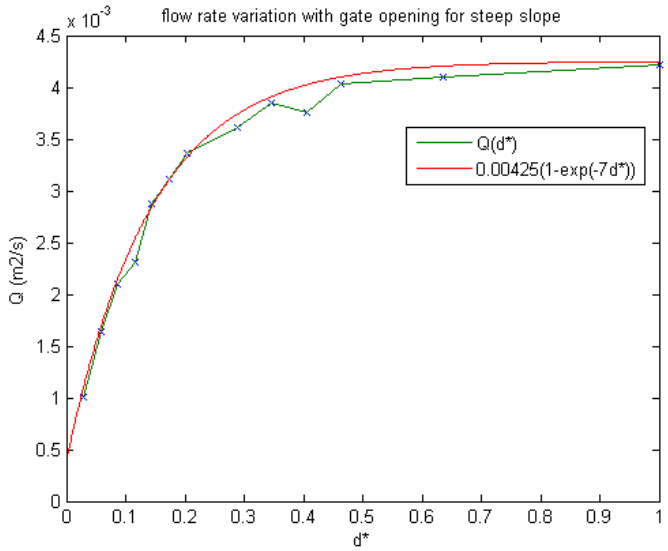

Figure IX-12: Flow rate in the channel as a function of gate opening for a steep seaward slope of the barrier

The resulting flow rate varies from 0.5 to 4.25 l/s. It is not equal to 0 when $d^* = 0$ because of the leakage of the gate. Indeed the gate was not perfectly fitting with the channel and some leakage was present on the sides. Moreover the gate was made of foam and therefore porous. This doesn't affect the final results since d^* is an intermediary variable to link the flow rate and the set-up.

9. Q as a function of d for a mild slope

Similarly the results for a mild seaward slope are presented Figure IX-13. As expected, the flow rate is higher for $d^* = 1$ ($Q_{d^*=1} = 0.0047\ m^3/s$) thanks to the higher momentum set-up which drives the flow. It increases also more rapidly.

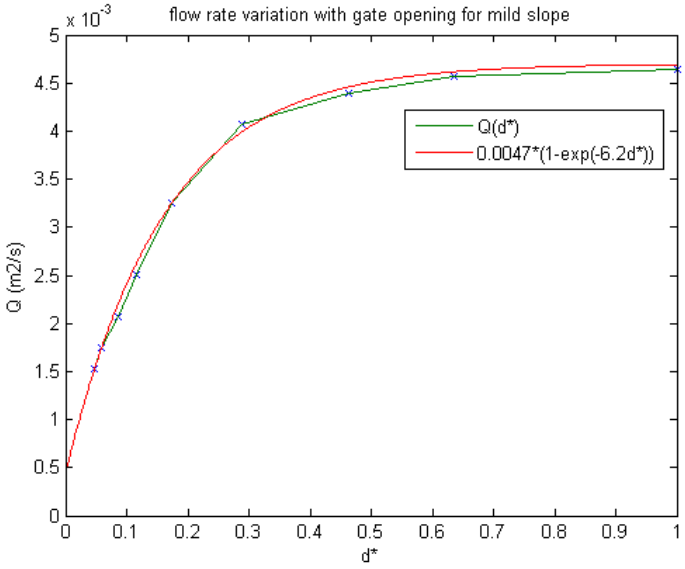

Figure IX-13: Flow rate in the channel as a function of gate opening for a mild seaward slope of the barrier

10. Cross-shore discharge and wave shape factor

The equation for the cross-shore discharge given in Eq. V-4 gives $\begin{cases} Q_{in} = 0.0069\ m^3 s^{-1} & steep\ slope \\ Q_{in} = 0.0055\ m^3 s^{-1} & mild\ slope \end{cases}$

This significant difference can be explained by the too simple estimation of the wave shape factor B_0, and probably an interference with the bore-like undertow for the steep slope case.

Using the experimental results we can calculate a more relevant wave shape factor for mild slopes:

$$B_0 = \frac{\frac{1+K_t}{2}\frac{h_c}{H_i} * \frac{1}{12} * \frac{0.0069}{0.0047} + 0.06\left(\frac{0.0047}{0.0069} - 1\right)}{\frac{1+K_t}{2}\frac{h_c}{H_i}} = 0.048$$

which is about the half of the assumed value of $\frac{1}{12}$ in part V.B. However it is also about the double of the value assumed by Calabrese in its model for this configuration.

11. Discharge fraction

The discharge fraction α can be calculated for each d^* from $\alpha = \frac{Q(d^*)}{Q_{in}}$ with the experimental value of Q_{in}.

C. Undertow and continuity set-up

Figure IX-14 shows the set-up against the discharge fraction, for the two configurations (steep and mild seaward slope).

It seems that δ is proportional to α for a steep slope and to $\sqrt{\alpha}$ for a mild slope. This is checked by fitting respectively a linear curve and a second order polynomial with inversed axis, both giving a correlation coefficient of 0.9998, i.e. very close to 1.

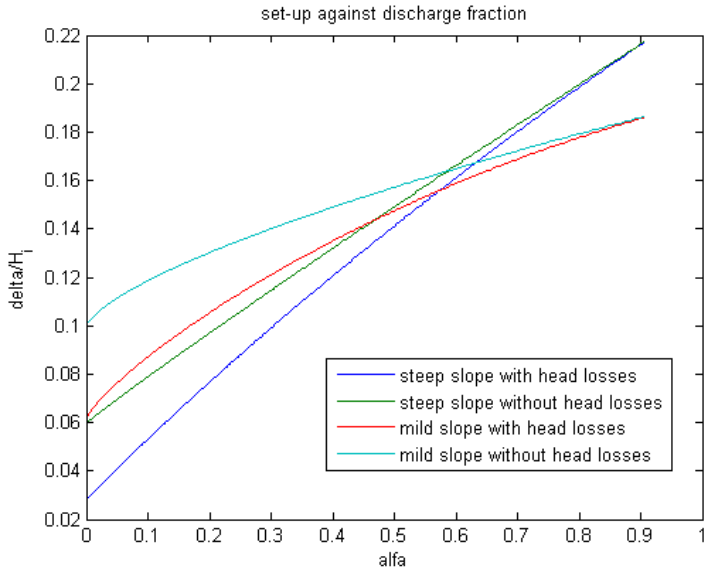

Figure IX-14: relative set-up against discharge fraction for the two configurations from experimental data. Details on head losses are found part IX.D

It is in first sight not in agreement with the theory of Calabrese et al. (2008) who stated that the 2D continuity set-up was defined by the Gauckler-Strickler formula $\delta_c = f{q_u}^2 = f{q_{in}}^2\alpha^2$.

However this relationship is only valid when $\alpha = 1$, i.e. when it is the undertow which drives the continuity set-up and not the contrary. As α decreases the set-up is driven by the hydraulic resistance in the gate which prevents all the cross-shore discharge from flowing in the channel, letting a fraction of it flowing over the barrier. It is then q_u (and therefore α) which is driven by the set-up. The relationship above gives a boundary condition.

1. Mild slope case (tan β=1/8)

Calabrese et al. (2008) calculated the friction coefficient f by the mean of **Eq. V-5** independently on the set-up, assuming the hydraulic diameter d_H equal the depth of the barrier crest.

In reality, d_H is the distance between the barrier crest and the wave trough, and it directly depends on the mean water level. Since the set-up increases continuously from the breaking to the reforming point, it has to be taken into account. Assuming a set-up increasing linearly, we get:

$$d_H = b\delta + c$$

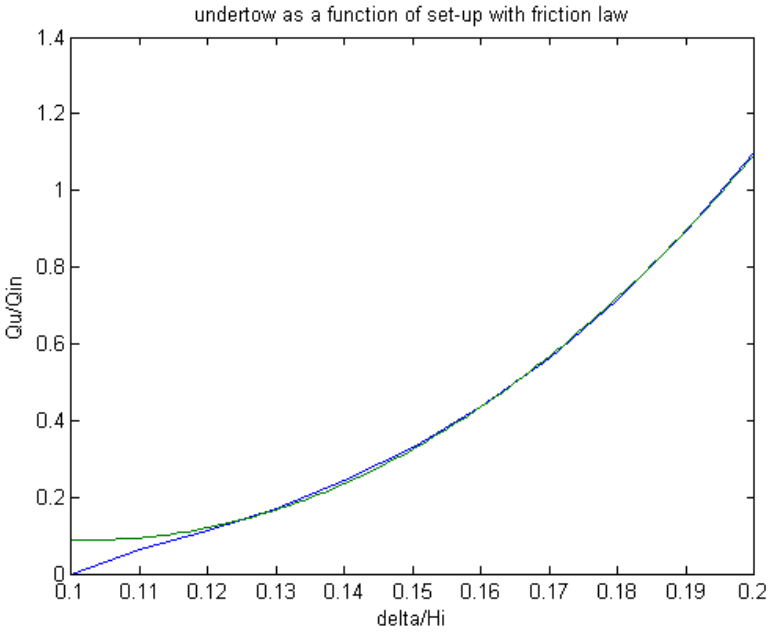

Figure IX-15: dimensionless undertow against relative set-up from theoretical friction law. Quadratic fitting for $0.12 \leq \frac{\delta}{H_i} \leq 0.2$

Then $q_u = \sqrt{\frac{\delta_c}{f}} = \sqrt{\frac{\delta_c (b\delta+c)^{10/3} \frac{2g}{f_w (b\delta+c)^{1/3}}}{B_{eq}}}$. Since $\delta = \delta_{mf} + \delta_c$, the dominant power of δ_c in the equation is $\frac{1}{2}\left(1+\frac{9}{3}\right) = 2$.

It is depicted on Figure IX-15. We see that when δ is large enough q_u is approximately proportional to δ^2.

It is therefore reasonable to say that δ varies with $\sqrt{\alpha}$, more accurately with $\alpha^{6/13}$

The range of values of the dimensionless discharge $\frac{q_u}{q_{in}}$, on Figure IX-15 is in agreement with experiments for a mild slope. It should be equal to α and therefore range from 0 to 1. To calculate the hydraulic diameter to calibrate properly the model we need the length of the surf zone (here taken as 25 cm) and the wave trough depth.

2. Steep slope case (tan β=1/2)

As mentioned in part VIII.C, observations of the undertow for a steep slope lead us to consider the latter as a bore, forming when the incident breaking wave is subsiding and vanishing when the wave is coming shoreward.

A bore is a hydraulic jump behaving like a dam break. It has been the topic of many investigations, for example Mory et al., 2010. A schematic bore is illustrated Figure IX-16. The discharge is defined as $Q = U_0 h_m$, where U_0 is the velocity in the bore head and h_m the height of the head.

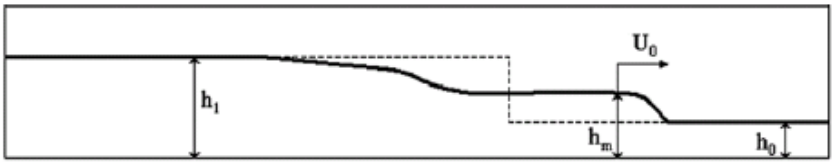

Figure IX-16: Propagation of a bore generated by a dam-break. The dashed line is the initial water level surface. The solid line schematizes the air/water interface a short while later. From Mory et al. 2010.

Dam-break theory from Stoker (1957) gives:

$$U_0 = \sqrt{\frac{g\, h_m}{2}\left(\frac{h_m}{h_0}+1\right)}$$

$$h_1 = h_m + (h_m - h_0)\sqrt{\frac{h_m + h_0}{2h_0}} + (h_m - h_0)^2\left(\frac{h_m + h_0}{8h_m h_0}\right)$$

In our case $h_0 = h_c$ and $\delta = h_1 - h_0$. The result is plotted Figure IX-17. We see that in the range $\frac{\delta}{H_i} \leq 0.3$, $q_u(\frac{\delta}{H_i})$ is a linear function, it confirms the experimental results.

The order of magnitude of the dimensionless undertow is somewhat too high (it should range from 0 to 1), since it has to be averaged over one wave period.

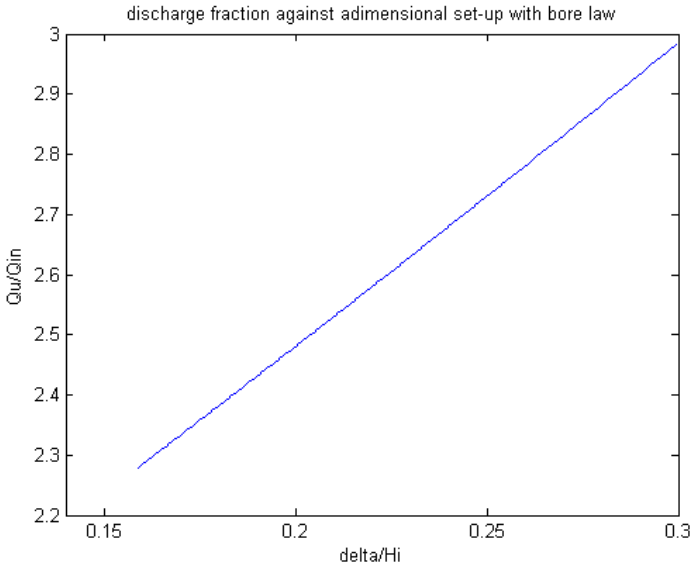

Figure IX-17: dimensionless undertow against relative set-up from theoretical bore law

D. Potential calculation

1. Head losses and way of evacuating the water carried inshore

There is a major difference between the proposed wave energy converter (see part III) and the lab-scale model.

In both cases a part of the onshore discharge returns directly seaward as undertow. The raw results presented in part IX.A and IX.B were therefore appropriate to link the undertow with the continuity set-up and find experimentally the momentum flux set-up.

To the contrary, the discharge in the channel which is used to calculate the potential is significantly different:

Instead of flowing downwards in a pipe to the turbine and then be spread out, the flow passes in a channel on a side of the structure (like a rip current) through a gate used to regulate the flow rate.

As a consequence the pressure head driving the flow measured in the test section is not directly the measured set-up (which drives the undertow). Indeed there are head losses in between due to an elbow of 90° in the flow and a restriction (diaphragm) in the test section.

The final experimental estimation of the potential depends directly on these head losses.

Singular head losses ΔH are defined by a head loss coefficient K proportional to the velocity squared:

$$\Delta H = K\frac{V^2}{2g} \qquad \text{Eq. IX-6}$$

From a fluid mechanics handbook (for example Chow 1959) we get:

$$K_{elbow\ 90^0} = 1.5$$

$$K_{diaphragm} = \frac{A_{channel}}{m * A_{test\ section}} - 1 + \frac{1}{9} \cong 4.5$$

With $m \cong 0.62$ (constriction of the flow)

$$K = K_{elbow\ 90^0} + K_{diaphragm}$$

Since the diaphragm is a "half-diaphragm" (no restriction on a side) and is stuck to the elbow, it is not possible to find an accurate value of K analytically; it would need experiments or CFD calculations.

2. Procedure to calculate $P = f(\alpha)$

1. Measure δ and Q for different values of gate opening d *done in part IX.A and IX.B*
2. Calculate $Q_u(d) = Q_{in} - Q(d)$ *done in part IX.B*
3. Find $\delta_{mf} = \delta$ for a fully opened gate and so $\delta_c = \delta - \delta_{mf}$ *done in part IX.A*
4. Deduce $Q_u(\delta_c)$ from $Q_u(d)$, $d(\delta)$, and $\delta(\delta_c)$ *done in part IX.C*
5. Calculate $\delta_{eff} = \delta - \Delta H$
6. Find $\delta_{mf\ eff} = \delta_{eff}$ for a fully opened gate and so $\delta_{c\ eff}$
7. Use $\delta_{c\ eff}$ in $Q_u(\delta_c)$ to find $Q_{u\ eff}$
8. Calculate $\alpha_{eff} = \frac{Q_{u\ eff}}{Q_{in}}$
9. Deduce $P(\alpha_{eff}) = (1 - \alpha_{eff})\, Q_{in} * \delta_{eff}$

3. Assumptions

- The undertow is driven by the continuity set-up δ_c only
- The momentum flux set-up δ_{mf} does not depend on α
- The friction is negligible

Regarding, the first assumption, the undertow depends on the discharge in the channel, which drives directly δ_c. The assumption amounts to saying that δ_c is only driven by the discharge fraction α. From the expression of the friction coefficient part IX.A we see that δ and α are the only varying fields. The assumption seems then to be reasonable.

The second assumption is known false, but the dependence of δ_{mf} with α has been either included in the calculation through δ_{vf}. The effect of α on the transmission coefficient is still unclear, but from part IX.A and Hansen & Svendsen (1987) it doesn't seem to play an important role.

The third assumption has been shown valid part IX.A.

4. Calculation of $\delta_{eff}(\alpha)$

$\Delta H(\alpha)$ is calculated by the use of **Eq. IX-6**. $V = \frac{Q_{in}(1-\alpha)}{S}$, with A_{ts} the area of the test section ($A_{ts} = 0.0213\ m^2$).

With the intention of a qualitative study, the rough approximation $K = 4$ is taken.

The results have been plotted on Figure IX-14.

This is the real driving force of the flow in the channel.

5. Calculation of P

Upstream from the channel the volume forces set-up $\delta_{vf\ eff}$ is 0 whatever α. Then $\delta_{mf\ eff} = \delta_{eff}(0)$.

As a consequence $\delta_{c\ eff}(\alpha) = \delta_{eff} - \delta_{eff}(0)$.

$\alpha_{eff} = \frac{Q_{u\ eff}}{Q_{in}}$. $Q_{u\ eff}$ is found from the relation $Q_u\ (\delta_c)$ determined part IX.C, used with $\delta_{c\ eff}$.

Then $P^* = (1 - \alpha_{eff})(1 + \Gamma_{c\ eff})$ with $\Gamma_{c\ eff} = \frac{\delta_{c\ eff}(1)}{\delta_{mf\ eff}}$

The results are plotted Figure IX-18 for a steep slope and Figure IX-19 for a mild slope.

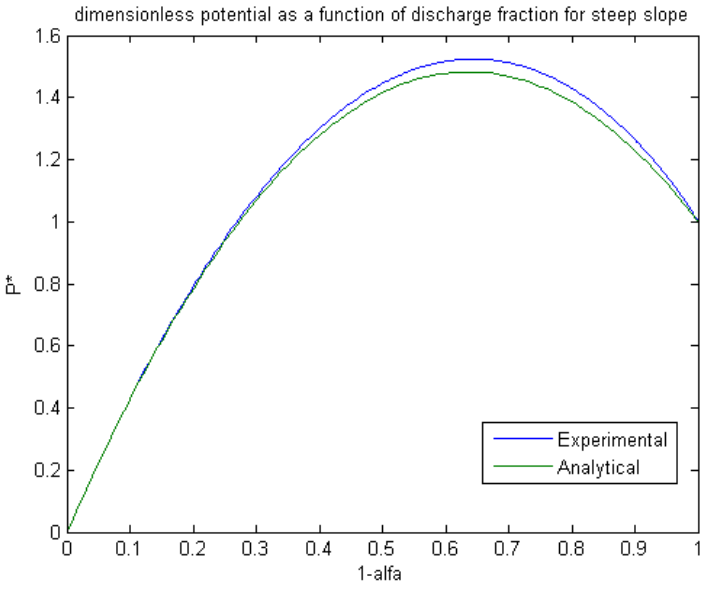

Figure IX-18: Experimental and analytical Dimensionless, steep slope

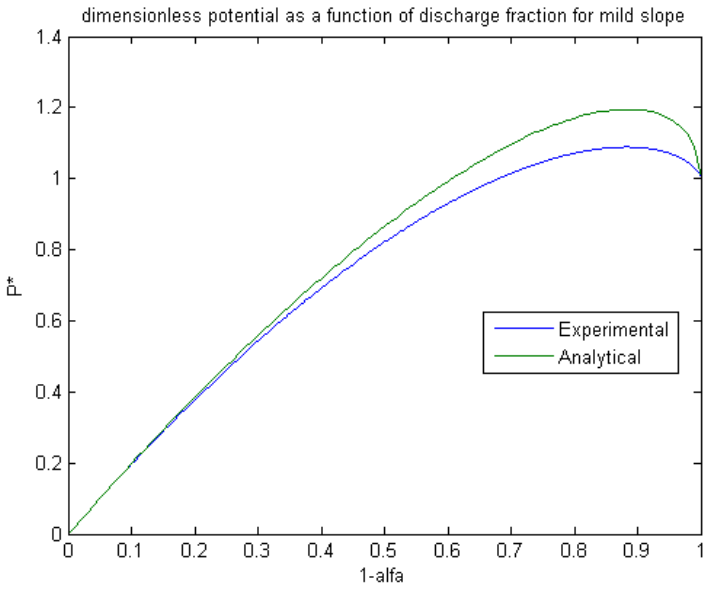

Figure IX-19: Experimental and analytical dimensionless potential, mild slope

As expected, the results have a good correlation with analytical results presented in part V.E, since the experimental relation Q_u (δ_c) has been used in the analytical model. The linear approximation for a steep slope is fully validated. To the contrary, we observe a discrepancy for mild slopes for high values of α. It is because the assumption Q_u proportional to ${\delta_c}^2$ is no more valid for low values of δ_c (see Figure IX-15). A better modeling should be used.

The theoretical results on Figure V-4 don't coincide neither with a steep nor with a mild slope. It proves the dependency of the friction coefficient on the hydraulic diameter, depending itself on the set-up. The modeling of the friction coefficient proposed by Calabrese et al. (2008) has no physical meaning.

E. Conclusions of 3D experiments

- Many rough assumptions and approximations were needed, among them we can note:
  - The calculation of the flow rate from ratios of velocities
  - The modeling of head losses between the trough and the channel
- Despite the high uncertainty, we can take the following values for the dimensionless potential:

$$P^* = \begin{cases} 1.5 \ \ steep\ slope \\ 1.1 \ \ mild\ slope \end{cases}$$

  in the conditions of the experiments.
- The analytical model of Calabrese for 2D set-up was not really in agreement with experiments for steep slopes, probably because of the overestimated wave reflection in the model or more probably because of uncertainties. The correlation was better for mild slopes.
- The model of Bellotti might describe properly the variations of the 3D set-up, but its needs some calibrations and a refinement for narrow channels.

- The wave shape factor had to be refined by half its assumed value to fit the analytical and experimental cross-shore discharges.
- The processes driving the undertow have been deduced from observations and describe properly its behavior. A friction-based undertow takes place for the mild slope case, and a bore-like undertow for the steep slope case.
- The analytical model of the variation of the hydraulic potential with the discharge fraction is validated for steep slopes, but the optimal potential is slightly overestimated for mild slopes. A correction of -10% can be considered.

X. Optimization

The experimental conclusions on the potential presented part IX.D have been carried out without any particular optimization, except the choice of a relative barrier crest of $\cong 0.3$ to get a high momentum set-up.

The final goal of this study is to quantify the energy potential; therefore an attempt of optimization is presented hereby.

A. Optimization from an energy conservation point of view

To get the highest ideal energy potential, all the energy contained in incident waves must be converted in hydraulic energy through set-up and currents. However it is well-known that waves dissipate their energy mostly into turbulence and heat.

These considerations are shown in the energy balance:

$$E_i = E_r + E_t + \underbrace{\overbrace{E_{channel} + E_{undertow}}^{Hydraulic\ energy} + D_{sr} + D_{fw}}_{Energy\ dissipated} \qquad \text{Eq. X-1}$$

In which D_{sr} and D_{fw} are the dissipations into turbulence and heat from surface rollers and bottom friction, E_r and E_t are the energies of the reflected and transmitted waves.

We want $E_{channel}$ as high as possible. E_t can be used by the next barriers, so we don't particularly wish to decrease it.

1. Decreasing E_r

Wave reflection occurs with brutal changes in depth. To avoid wave reflection we must therefore use mild incident slopes $\left(\tan\alpha \leq \frac{1}{10}\right)$, but also ideally a mild slope on the inshore toe of the barrier. The continuity set-up can itself create a brutal change in depth if it increases sharply. A repartition of the friction over the barrier should reduce this problem. Waves can also be reflected by currents like the undertow. To lower $E_{undertow}$ will then lower E_r . Except the incident slope, those sources of wave reflection are beyond the scope of this survey and no order of magnitude is given. One can refer to Mei (1989) for more precisions.

2. Decreasing D_{sr}

The goal is then to force the surface rollers to dissipate the energy in a useful way (i.e. in set-up)

The evolution of energy in surface rollers can be split in two phases:

- First the energy grows: It is transmitted from the ordinate wave to the surface roller. The latter is then a mass of water travelling at the speed of the ordinate wave, containing a lot of kinetic energy.
- When the wave has passed a critical dept, the roller starts to dissipate its energy.

This phenomenon has been pointed out by Svendsen (1984a) after the experimental results of Hansen & Svendsen (1979) and analyzed more precisely by Basco (1985). The latter found out that the transition point for mild slopes was located, as a good approximation, at a depth

$h_{trans} = 0.8\, h_b$ with h_b the breaking depth.

D_{sr} would then be equal to 0 if we take advantage of the kinetic energy contained in surface rollers in the transition region, i.e. $h_b \geq h \geq h_{trans}$.

3. Decreasing D_{fw}

D_{fw} is very small if f_w is low, i.e. the sea bed is smooth. This does not cause any technical problem in itself, but the lower f_w, the lower δ_c if the latter is still driven by the friction over the barrier.

Let's now assume that δ_c is a direct conversion of the kinetic energy contained in the surface roller as pointed out above. In other words, the surface roller gives the energy necessary to force all the cross-shore discharge to flow toward the turbine. Technical solutions are proposed part X.B.

f_w does not influence the set-up anymore and a smooth bed could be considered, reducing D_{fw} to a negligible value.

4. Decreasing $E_{undertow}$

$E_{undertow}$ is equal to 0 if the entire cross-shore discharge flows into the channel. If the continuity set-up δ_c is caused by friction, a decrease in $E_{undertow}$ would induce a decrease in $E_{channel}$, as shown in parts V.E and IX.C. It is again preferable for δ_c to be created by other sources.

If δ_c is balanced by the surface rollers, the highest potential would be reached when the surface roller energy E_{sr} equals the work W_p needed to counteract pressure forces induced by the continuity set-up.

$$W_p = E_{sr} \qquad \text{Eq. X-2}$$

W_p equals a force times a distance, i.e. across the transition region (area noted Ω on Figure X-1).

$$W_p = \int_0^l \int_0^{\delta_c(x)} \rho g z \, dz \, dx$$

l is the length of the transition region.

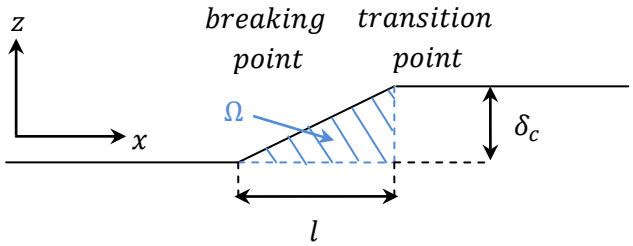

Figure X-1: Momentum balance across the surf zone

If the setup is assumed linear: $\delta_c(x) = \frac{\delta_c}{l} x$

We get $W_p = \rho g \frac{{\delta_c}^2}{2l^2} \int_0^l x^2 \, dx = \frac{\rho g}{6} {\delta_c}^2 l$ **Eq. X-3**

Svendsen (1984a,b) expressed the surface roller energy per unit of area as proportional to its area in the cross-shore vertical plane S_{sr}:

$E_{sr} = \frac{1}{L}\rho S_{sr}\frac{c^2}{2}$

In which S_{sr} is the roller area and c the wave celerity. In shallow water we have $c = \sqrt{gh}$.

Okayasu (1986) found out the relationship: $S_{sr} = 0.06\ H\ L$

Then

$$E_{sr} = \rho g \frac{0.06}{2\ l}\int_0^l H(x)h(x)dx \qquad \text{Eq. X-4}$$

We then get from Eq. X-3 and Eq. X-4:

$$\delta_{c\ max} = \sqrt{3 * 0.06 * \frac{1}{l}\int_0^l H(x)h(x)dx} \qquad \text{Eq. X-5}$$

It is the highest theoretical continuity setup.

To calculate $\delta_{c\ max}$ we shall assume that the ratio $\frac{H}{h}$ is constant in the transition region. This assumption has been used in many models and shown reasonable, for example in Bowen (1969). This constant is taken as the breaking depth criterion for mild slopes, i.e. $\frac{H_b}{h_b} = 0.8$.

Then $\int_0^l H(x)h(x)dx = \int_0^l 0.8\ h(x)^2 dx$

If h is linear, $h(x) = h_b + \frac{h_{trans}-h_b}{l}x = h_b\left(1 - \frac{0.2}{l}x\right)$, So

$$\int_0^l H(x)h(x)dx = \int_0^l 0.8\ {h_b}^2\left(1 - \frac{0.2}{l}x\right)^2 dx = 0.8{h_b}^2\frac{l}{0.2}\frac{1}{3}(1 - 0.8^3) = 0.65\ {h_b}^2 l$$
$$= 1.02\ {H_b}^2 l$$

Finally $\delta_{c\ max} = \sqrt{3 * 0.06 * \frac{1}{l}1.02\ {H_b}^2 l} = 0.43\ H_b$ Eq. X-6

An order of magnitude of the ideal potential for one barrier is then

$$P_{max} = \rho g Q_{in}(\delta_{mf} + 0.43\ H_b)$$

It is of course impossible to reach, but it represents the upper limit, analogous to the Betz theorem for wind power.

B. Optimization of the potential from analytical models

1. Full scale potential

The lab scale model was an undistorted Froude model. The scaling ratio was defined by

$sr = \frac{H_{full\ scale}}{H_{small\ scale}}$

Therefore when extrapolating to full scale, the lengths are multiplied by sr and the velocities by $\sqrt{sr}$.

From the dimensionless potential calculated analytically in part V.E and validated experimentally part IX.D, we can deduce the energy potential for a full scale structure.

$$P = P^* \, \delta_{mf} \, Q_{in}$$

δ_{mf} is proportional to H and therefore to sr. Q_{in} is proportional to $sr^{3/2}$.

P^* depends on $\Gamma_c = \frac{\delta_{c1}}{\delta_{mf}}$ which does not change with H. Finally $P_{full\ scale} = P_{lab\ scale} * sr^{5/2}$

2. Capture ratio

For the calculation of the order of magnitude of the potential for full scale, we shall take an offshore wave height H_0 of 2.3m and a period T of 7s. The corresponding steepness is 0.03. The length of the barrier is 100m.

Wave linear theory gives the energy flux per meter of wave crest:

$E_f = \frac{1}{8}\rho g {H_0}^2 c_g = \frac{1}{16}\rho g {H_0}^2 \frac{L_0}{T} = 36\ kW/m$. It is a common sea state, e.g. the average value over one year off the coast of Norway.

The capture ratio d is a way of analyzing efficiency for wave power. $d = \frac{P}{E_f L_{capture}}$

The offshore wave height and the incident wave heights are linked by the shoaling coefficient $K_s = \frac{H_i}{H_0}$ calculated from linear wave theory.

The energy potential in the experimental conditions with a scaling ratio of 45 gives:

$P = 266\ kW$. Then $d = \frac{266}{100*36} = 0.074$

It means that 7.4% of wave energy is transformed into currents, the rest is lost.

This value is very low, since no particular optimization has been done.

3. Comparison between steep and mild slopes

From the high dimensionless potential for steep slopes, one could jump to the conclusion that steep slopes are more efficient than mild slopes. However one as to multiply by the momentum flux set-up to get the real potential, and it is considerably smaller for steep than mild slopes. All in all the two optimal potential are exactly the same if we consider $\begin{cases} \frac{\delta_{mf}}{H_i} = 0.15\ mild\ slope \\ \frac{\delta_{mf}}{H_i} = 0.10\ steep\ slope \end{cases}$ like the 2D experiments suggest.

However it could be a coincidence and generally the potential would be higher for mild slopes due to the higher value of α_{opt}, allowing a higher flow rate.
There are also more perspectives of optimization for a mild slope, from the energy conservation point of view. Indeed the energy lost in the steep slope case is hopeless to be used:

- Energy from reflected waves by steep slopes is definitely lost
- There is no hope to catch the energy from surface rollers since the transition region (see part X.A) is short, not to say inexistent due to the rapid change in depth.

For the optimization we shall consider only the mild slope case.

4. Parameters influencing the potential

From the results part IX.D, we have $P_{opt} = Q_{in}\ \delta_{mf}\ P^*(\alpha_{opt}) = Q_{in}\ \delta_{mf}\ P^*{}_{opt}(\Gamma_c)$

$P^*{}_{opt}(\Gamma_c)$ is plotted Figure X-2.

It seems clear that it would be worthy to increase Γ_c, without reducing δ_{mf}, i.e. increase $\delta_{c\,1}$,i.e. increase f and Q_{in}. However increasing f amounts to saying either increasing the wave friction factor f_w, either the width of the barrier B_{eq}. Both actions will tend to decrease the transmission coefficient K_t, therefore increasing δ_{mf} but decreasing Q_{in}.

To this adds the fact that a second barrier can be considered. The set-ups add from the first barrier to the second. Therefore the potential reads:

$P = Q_{in_1}\ \delta_{mf_1}\ P^*{}_1 + Q_{in_2}(\delta_1 + \delta_{mf_2})P^*{}_2$, with $Q_{in} = Q_{in_1} + Q_{in_2}$.

A decrease in K_t would also mean a decrease in H_t and so Q_{in_2} and δ_{mf_2}. And the $P^*(\alpha_{opt})$ calculated before is no longer valid for the first barrier since α plays a role in the term $(\delta_1 + \delta_{mf_2})$.

On top of that, it is worthy to add reflectors to increase the potential, like on the Wave Dragon (see Kramer & Frigaard (2002)). It increases H_i, but at the same time $\frac{H_i}{L_i}$ and decreases Q_{in}.

This interconnection of parameters in the potential renders an analytical survey impossible. One has to try different combinations of parameters in the numerical model and find the best one.

5. Optimization of the continuity set-up

Besides the fact that increasing Γ_c is extremely delicate, the friction law for the continuity set-up is certainly not the best one in terms of efficiency, as pointed out part X.A.

An efficient system would:

- Prevent water from flowing seaward over the barrier
- Allow waves propagating over the barrier (avoid wave reflection)
- Allow waves carrying water shoreward, i.e. no obstacle between the wave trough and the wave crest
- Preferably catch kinetic energy from surface rollers

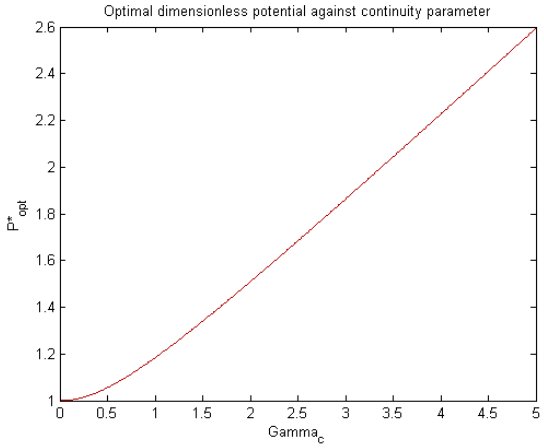

Figure X-2: Optimal dimensionless potential against continuity parameter

Several technical solutions can be considered. The most obvious one would be an array of flexible membranes, slack enough not to disturb wave motion (particularly at the bottom), and waterproof to avoid undertow. The top of the membrane should never be higher than the wave trough.

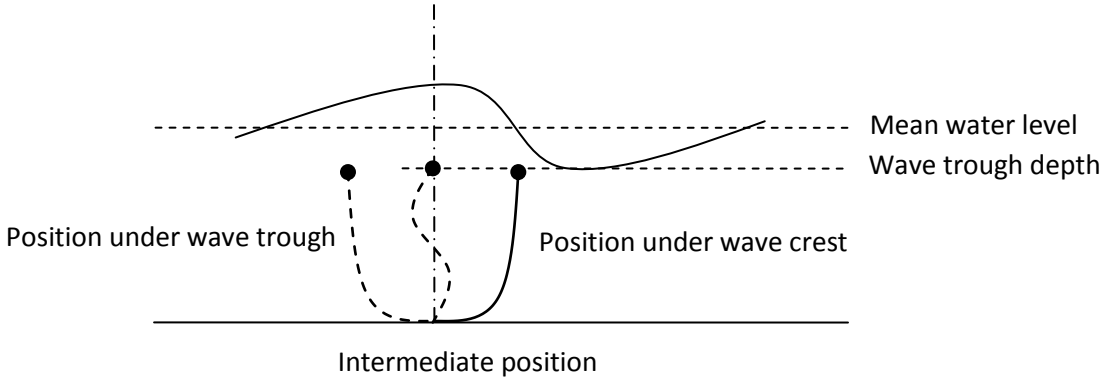

Figure X-3: Flexible membrane concept

An attempt of experimental investigation on this topic has been done. Stripes of adhesive tape regularly cut (each cm) has been stuck on the barrier crest (see Figure X-4). Unfortunately it turned out that waves encountered difficulties to propagate over the barrier, and the results on the set-up were falsified, since there was no way to differentiate the continuity and the momentum flux set-ups.

To the contrary the results were successful for steep slopes, as the bore-like undertow and the inshore discharge were separated in time. It was shown Figure VIII-4 with the two large blue circles. The stripes increased the continuity set-up by more than 100% (if we take into account the overestimation of the momentum set-up for steep slopes by the analytical model).

Several membranes should be considered to avoid wave reflection from brutal changes in depth. Information can be found within stiff flexible membrane breakwaters, e.g. in Kee & Kim (1996 I and II). The purpose is fundamentally different but the theory remains the same. A 100% transmissive membrane is impossible to build (some reflection occurring), and a balance has to be found.

An improvement to this concept would be a free rotation at the bottom, but only shoreward. The length would be high so that the system could emerge. When the wave is propagating shoreward, the surface roller hits the top and makes the structure rotate. With a smart balance between inertia

and restoring forces, the plate would stay right underneath the trough for a while and emerge again for the next surface roller. This has also been tried experimentally but the problems were the same as mentioned earlier.

Another option would use the Venturi effect. The membrane would then be very slack and free at the bottom. As the undertow becomes stronger the pressure drops, the membrane is sucked and tightens the duct. This effect has been observed while operating the first attempt above.

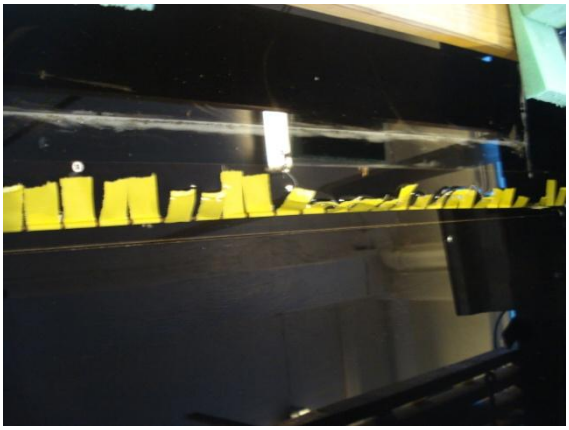

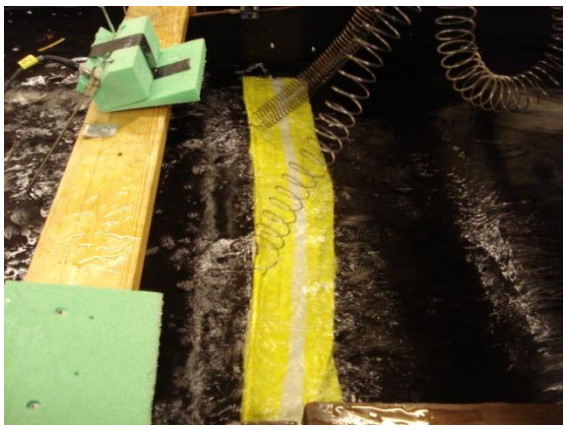

Figure X-4 and Figure X-5: Attempts to reduce the undertow and catch energy from surface rollers

Side effects

As the membrane stops totally the undertow, **Eq. V-10** applies and the water level is rising in the trough behind the barrier but also on the barrier crest. The top of the membrane has then to be higher to keep on blocking the undertow.

Such a process can obviously not continue infinitely and the theoretical limit has been determined in part X.A, i.e. when the surface roller has no longer enough energy to transport the elevated water inshore the barrier.

Moreover, the increase of mean water level has a direct impact on wave breaking since h_c is changing. The barrier should therefore rise, rather than the membrane. Then either the breaking points moves seaward, either the mean water level increases more sharply.

The first option would reduce considerably the cross shore discharge since water would return directly offshore before having passed the barrier.

The second one would increase wave reflection.

In both cases energy is lost. A balance has to be found.

Advantages of such mechanisms

- It insures a continuity set-up varying weakly with the undertow. As a consequence we could take advantage of the whole cross shore discharge, keeping a high set-up:
  $\alpha_{opt} \cong 0 \quad and \quad P^*_{opt} \cong 1 + \Gamma_c$
  It increases the potential by 35%.
- If the top of the membrane can rise at the same time as the mean water level, a very high continuity set-up could be reached, i.e. a very high Γ_c .
- If on top of that the mechanism can catch the energy from the rollers, the theoretical limit introduced part X.A would be even more approached.

6. Geometry of the barrier

From experiments and analytical models it is clear that the relative crest depth $\frac{h_c}{H_i}$ plays a key role in the transmission coefficient and therefore in the momentum flux set-up. $\frac{h_c}{H_i}$ and the crest width $\frac{B}{H_i}$ are the parameters to be varied to reach the optimal transmission coefficients found in the following. $\frac{h_c}{H_i}$ is easier to change than $\frac{B}{H_i}$, since it can be achieved by sinking or lifting a floating structure.

The influence of the relative trough depth $\frac{h_t}{H_i}$ has to be taken into account. As pointed out experimentally in part VIII.G, the higher the trough depth, the higher the set-up. It is shown on Figure X-6.

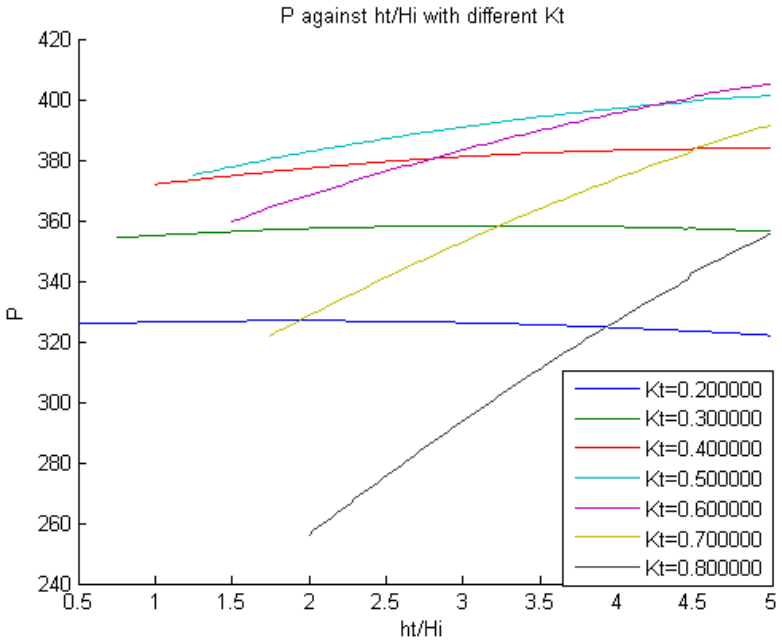

Figure X-6: Potential as a function of trough depth. Each curve starts from the limit of wave reformation.

It appears that there is very strong increase of the potential with $\frac{h_t}{H_i}$ for low transmission coefficients. However the model is not designed for such high $\frac{h_t}{H_i}$, and for example the effect of reflection from brutal change in depth should play a role.

7. Obliquely incident waves

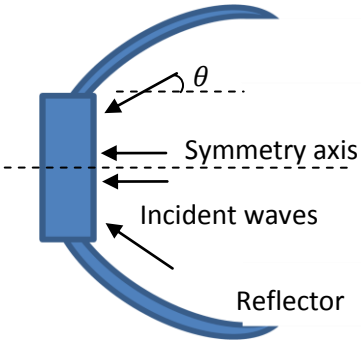

It is well known that a longshore current occurs when waves break on the shore with an angle. Indeed a momentum unbalance is created in the longshore direction due to the decay of the shear components of the radiation stresses S_{xy}. A pressure gradient is then formed which drives the flow toward the channel.

In the concept presented part III there is no channel, the turbine being underneath the structure. Waves propagate with an angle symmetrically to an axis in the middle of the structure. It can be done by wave reflectors, or by changing the inclination of the barrier. The

pressure gradient is then transformed in an alongshore set-up, and the highest point is on the axis of symmetry.
At this point (subscript a) waves break normally to the structure ($\theta_a = 0$).
In the model of Calabrese, the term $S_{xx\,t} - S_{xx\,i}$ becomes

$$\underbrace{S_{xx\,t} - S_{xx\,i} + S_{yx\,a} - S_{yx\,t}}_{cross-shore\ balance} + \underbrace{S_{xy\,t} - S_{xy\,i} + S_{yy\,a} - S_{yy\,t}}_{alongshore\ balance}$$

Where $S_{ij}(\theta)$ is calculated from radiation stress theory (see appendix D).

Results are plotted Figure X-7.

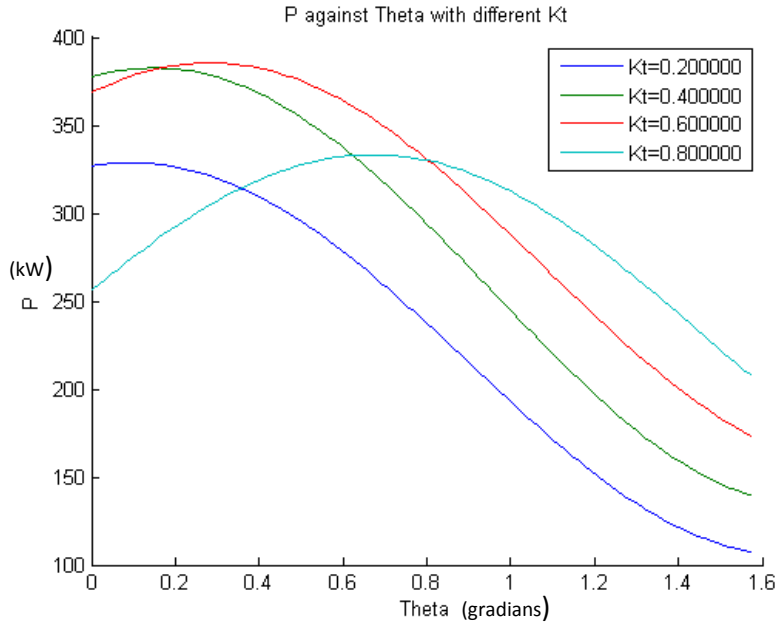

Figure X-7: Potential as a function of incident angle for several transmission coefficients

The highest efficiency is obtained with nearly normally incident waves for $K_t \leq 0.5$. The optimal angle of incidence θ_{opt} increases then with K_t. For $K_t = 0.8$ we have $\theta_{opt} = 38°$. The potential increases by 30% with respect to the normally incident waves case.

These results depends also strongly on the value of $\frac{h_t}{H_i}$.

The increase of mean water level on the symmetry axis is not compensated in the cross-shore direction and acts as the continuity set-up regarding the undertow. Therefore an emergent barrier (with overtopping) should be considered at this location.

8. Optimization of the transmission coefficient and discharge fraction for two barriers

To take advantage of the transmitted wave, a second barrier is needed.

The first barrier has a high flow rate but a low pressure head. The second one is the opposite. The transmission coefficient of the first barrier is a key factor. A fraction of the flow rate of the first bar can be “transformed” in pressure head for the second one through the continuity set-up. The optimization of the second barrier is identical to one barrier alone.

The total dimensionless potential is written

$$P^* = \frac{P}{Q_{in}\delta_{mf_1}} = \frac{Q_{in_1}}{Q_{in}} P^*{}_1(\alpha_1) + \frac{Q_{in_2}}{Q_{in}}\left(1 + \frac{\delta_{c_1}}{\delta_{mf_1}} + \frac{\delta_{mf_2}}{\delta_{mf_1}}\right) P^*{}_2$$

Or $$P^* = \left(1 - \frac{Q_{in_2}}{Q_{in}}\right) P^*{}_1(\alpha_1) + \frac{Q_{in_2}}{Q_{in}}\left(1 + \Gamma_{c\,1}\,\alpha_1{}^2 + \frac{\delta_{mf_2}}{\delta_{mf_1}}\right) P^*{}_2$$ **Eq. X-7**

$\frac{Q_{in_2}}{Q_{in}}$ and $\frac{\delta_{mf_2}}{\delta_{mf_1}}$ depend on K_t.

$\frac{h_t}{H_i}$ takes the arbitrary value of 2, but a higher potential is to be expected for higher $\frac{h_t}{H_i}$.

$\Gamma_{c\,2} = \frac{\delta_{c\,2}(\alpha=1)}{\delta_{mf\,2}+\delta_1}$ is assumed to be small enough so that $\alpha_{opt\,2} \cong 0$.

$(\delta_{mf} * Q_{in})(K_t)$ is plotted Figure X-8 for one barrier. We get $K_{t\,opt\,2}$ =0.48.

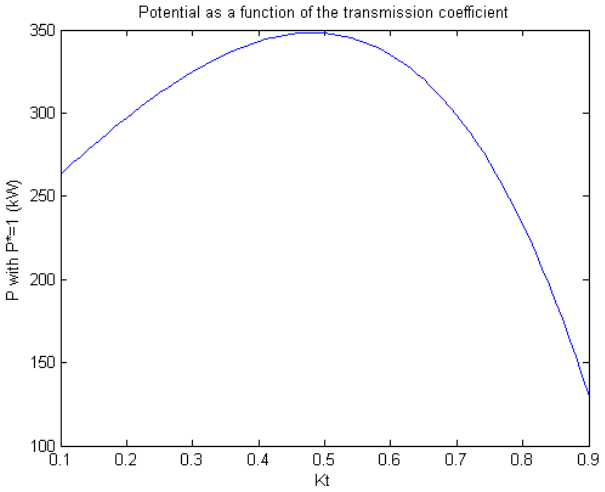

Figure X-8: Optimal transmission coefficient for one barrier

Using the value of $K_{t\,opt\,2}$ above and $\alpha_{opt\,2} = 0$, P^* is plotted

Figure X-9 as a function of $K_{t\,1}$ with different values of α_1. $\Gamma_{c\,1}$ is calculated each iteration from $\Gamma_{c\,1} = \frac{f q_{in\,1}{}^2}{\delta_{mf\,1}}$.

f equals the value deduced experimentally part VIII.D divided by the scaling ratio squared.

We suggest the combination $(K_{t\,1}, \alpha_1)_{opt} = (0.8\,, 0.15)$. Taking $\theta_1 = 38°$ as suggested above and keeping $\theta_2 = 0°$ it gives $P^*{}_{opt} = 8.6$.

Such a high dimensionless potential is normal considering the low value of δ_{mf_1} when $K_{t\,1} = 0.8$.

A higher efficiency would be reached for $K_{t\,1} > 0.8$ but such a high value of transmission coefficient after wave breaking is not physically consistent (Van der Meer et al. (2005)).

The capture ratio is then $d = 15\%$

For three barriers, it rises to $d = 18\%$

If we take $\frac{h_t}{H_i} = 5$, the capture ratio would theoretically only raise to $d = 19\%$ with 3 barriers, because the increase in $\frac{h_t}{H_i}$ has a negative effect on the increase of the potential by θ.

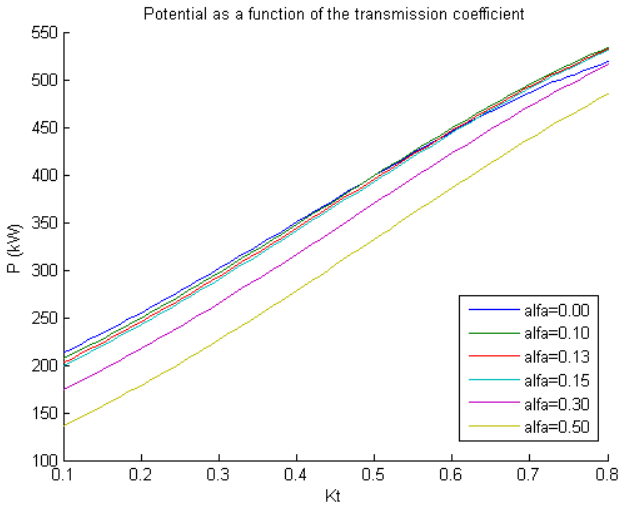

Figure X-9: Optimal transmission coefficient and discharge fraction for two barriers

9. Use of reflectors

Reflectors are used on the Wave Dragon© concept to focus waves toward the central part (ramp in the Wave Dragon, barrier in this study). The effectiveness of these reflectors is studied in Kramer & Frigaard (2002).

They found out that the input energy flux could be increased by 40% by the reflectors. It is complicate to link the energy potential to the energy flux, because we don't exactly know the dependency of the cross-shore discharge on the wave length.

For an optimal efficiency the distance between the two seaward ends of the reflectors is 2.6 times the length of the barrier, i.e. 260m in our study case.

C. Real sea conditions

1. Regulation

In reality it is extremely difficult to get a so precise value of transmission coefficient, wave breaking staying a complicated and unpredictable process. In the same way to calculate the discharge fraction in operation would not be easy. The optimal values of K_t and α found out above might be approached, but never reached exactly all the time. A loss in efficiency would follow.

2. Irregular waves

So far, all the analyses (experimental or analytical) have assumed regular waves. Such an ideal case is not real, and waves have in real sea conditions many components of different frequencies, which all together form a wave spectrum. The link between the regular wave height and the spectrum of irregular waves has been found out by Loveless and Diebski (1998) and Calabrese et al. (2008) checked it analytically. It states that a reasonable approximation of the 2D set-up for a Rayleigh distribution of irregular waves is obtained considering $H_{0\,regular} = H_\mu$, H_μ being the average wave height given by:

$H_\mu = \sqrt{2\pi m_0}$ in which m_0 is the standard deviation of the spectrum. This amounts to saying that we should consider a fraction as low as 63% of the significant wave height as input in the regular model to extrapolate to irregular waves.

However this was carried out for breakwaters and steep slopes. For mild slopes, the numerical model SHORECIRC suggests to use the significant wave height itself.

All in all the potential for irregular waves should decrease, but the extent is unknown to date.

3. Directional waves

Irregular waves in direction are not desirable, since only the fraction of wave energy having a direction close to the mean one can be captured. Therefore it is better in terms of efficiency to have the structure nearshore, where wave refraction gathers the waves in a direction perpendicular to the shore. Anyway a loss of energy should occur.

4. Depth of capture

To capture the maximum of wave energy, the incident point must be as deep as possible. The energy decreases exponentially with twice the depth. As a consequence 95% of E_f is captured if the depth of the incident point is equal to one quarter of the wave length, i.e. from 50 to 15 m depending on the sea-state.

To conserve wave energy from the seaward extremity to the barrier, the slope has to be mild enough to avoid reflection.

From the two points mentioned above and if we consider a straight structure, a length from 100 to 400m seaward from the barrier would be needed! It is obviously not economically conceivable. A more sophisticated profile can be used to reduce this length. However some energy is expected to be lost.

5. Turbine

The ducted THAWT (transversal horizontal axis water turbine) seems to be the most appropriate way to extract energy from this concept. It can handle a huge flow rate (directly proportional to its length, which has no theoretical limit) and a very low pressure head.

The turbine would be ducted to increase efficiency. Nevertheless the latter would be quite low, the state-of-the-art value being 60%. However this type of turbine is under development and no advanced optimization has been done like on Kaplan turbines, so no final conclusion can be drawn.

Technical information on ducted THAWTs can be found in Furukawa et al. (2009), and a global review in Khan et al. (2009).

The created energy potential can also be used differently, for example to increase the current velocity close to the bottom for tidal turbines to increase efficiency. It would also protect them from waves and avoid fatigue phenomena from both waves and the non-uniform velocity profile across the depth.

D. Competitiveness of wave energy conversion from wave-induced currents (WIC)

We shall give two examples of existing wave energy converters (WECs) at an advanced stage of development. A cost-efficiency comparison with the WIC concept gives an idea of the future of our concept.

1. Pelamis wave power

It is the wave energy converter at the most advanced stage at the moment. Full-scale prototypes have been tested and validated and pioneer commercial projects are running. The concept consists in a "sea-snake" made of several cylindrical sections linked by hinged joints. In each articulation, fluid is pumped to high pressure. Hydraulic motors produce electricity. It is then a wave absorbing body, but not a point absorber. Its rated power is 750 kW for a 180m long device. Its capture ratio is very high (90%) but the capture length is small (around 15m).

Figure X-10: Reference wave energy converters

2. Wave Dragon

The wave dragon is an overtopping device, which means that it is a large structures gathering waves and making then run over a ramp. A reservoir located behind the ramp is filled. Classical hydraulic energy through Kaplan turbines produces electric energy.

For a capture width of 300m (between the two seaward edges of the reflectors), its announced rated power is as high as 7 MW for a 36 kW/m sea state. It means a capture ratio of $d = 169\%$. The reflectors increase it by 40%, but d remains higher than 100% which is impossible.

In real sea conditions it is known that the capture ratio of the wave dragon is between 10 and 12%.

3. Comparison

Overtopping device VS wave absorbing body

The Wave Dragon and the WIC concept are in many ways similar. The only difference is that the WIC concept uses the conservations of wave momentum and mass and overtopping devices only mass. They present the same advantages and disadvantages compared to the Pelamis or other wave activated bodies:

- The width of capture is much larger, with no theoretical limit (we could build a ramp or a barrier as long as we would like). The power per unit is therefore higher.
- They can be used to protect the shore, adding economical interests.
- No wanted oscillations with waves. Problems of resonance during storms are avoided.
- No moving parts except the turbine leading to lower maintenance cost
- A more regular way of producing electric energy, so a cheaper connection to the grid

But:

- A much lower capture ratio. It is a "waste" of energy as long as the latter is considered as finite. At the moment the possible locations for wave energy converters are endless.

- An disability to be carried on a ship: difficulties of installation and maintenance

Unlike the Pelamis, wave activated bodies being also point absorbers have an even smaller width of capture, but the ability to capture energy from chaotic (strongly irregular in direction) open sea waves.

Wave-induced current concept VS Wave Dragon

Compared to the Wave Dragon, the WIC concept has the following advantages:

- Less mechanical stresses thanks to the fully underwater device. Breaking occurs on water and not on the structure.
- The decrease in potential from regular to irregular waves is expected to be lower since nearly all the waves break either on the first either on the second bar. In the Wave Dragon low waves don't run over the ramp and are lost.
- Many more possibilities of improvement of the capture ratio. The lost energy can theoretically be captured. In the wave dragon a high wave reflection takes place and the kinetic energy of the overtopping waves is lost as a jet in the reservoir.
- A THAWT is much cheaper to build/maintain than a Kaplan turbine for ultra low pressure heads.

But:

- If no technological improvement is done to increase the continuity set-up independently from the flow rate, the capture ratio stays low in the WIC concept. Breaking dissipates much energy, though it is theoretically possible to catch it.
- The THAWT has a bad efficiency at the moment compared to Kaplan turbines, but it is still at early stage of development.
- The concept of wave reflectors is patented by the Wave Dragon.

XI. Concluding remarks

Conclusions of 2D and 3D experiments have been presented in parts VIII.H and IX.E.

A. Estimation of the energy potential

This study has presented a new way of extracting energy from ocean waves. The related natural phenomenon has been explained and the processes playing a role in the energy potential have been analyzed separately. Analytical results have been validated experimentally and lead to the following conclusions:

- The energy potential for each barrier depends linearly on the momentum flux set-up, the continuity set-up the net cross-shore discharge (influx minus undertow)
- The momentum flux set-up is all the higher as:
  - The incident wave is high (linear relation)
  - The transmission coefficient is low
  - The waves break symmetrically with a precise angle (depending on the transmission coefficient)
  - The wave steepness is low
  - The water behind the barrier is deep (depending on the transmission coefficient and the incident angle)
  - The depth of the barrier crest is small
- The continuity set-up is all the higher as:
  - The incident wave is high (linear relation)
  - It does not depend on the undertow (e.g. use of membranes)

  If it does:
  - The undertow is high (friction-based or bore-like undertow):
    - The discharge fraction is high
    - The influx is high
  - The friction coefficient is high (friction-based undertow):
    - The barrier crest is shallow
    - The barrier crest is wide
    - The barrier crest is rough, to an unknown extent
- The net cross-shore discharge is all the higher as:
  - The discharge fraction is low
  - The influx is high:
    - The wave height is high (increases with $H^{3/2}$)
    - The transmission coefficient is high
    - The wave shape factor is high (its dependency on wave conditions and barrier geometry hasn't been studied)
    - The depth of the barrier crest is not too high, not too low
- The potential for the next barrier is all the higher as:
  - The total set-up behind the previous barrier is high
  - The transmitted wave is high (i.e. high transmission coefficient for the previous barrier)
- The transmission coefficient is all the lower as:

  - The barrier crest is wide (not checked successfully in this study)
  - The barrier crest is shallow
  - The wave steepness is high
  - The undertow is weak (not checked in this study)
- The potential can be increased by:
  - Changing the nature of the undertow and reducing it
  - Using reflectors
  - Capturing energy from surface rollers
- Energy is lost through:
  - Wave breaking
  - Real sea conditions
  - Reflected waves
  - The undertow
  - Waves propagating beyond the structure
  - The turbine efficiency

B. General conclusions

- To sum up the conclusions drawn in parts VIII.H and IX.E, most of the analytical models considered provide reasonable orders of magnitudes, but need a calibration from experimental results to be fully expendable. Some refinements can be necessary too, and some unexplained differences are to be noticed.
- Regarding 3D experiments, observations of unexpected phenomena were needed to correct the models, and the potential has been finally properly modeled. Final conclusions on the optimal combination (flow rate, pressure head) are carried out and allow a determination of the potential of the lab-scale model.
- The objectives were more ambitious than expected, and no precise/thorough conclusions can be given. They are indeed falsified by uncertainties in the measurements, and the question of the applicability of the analytical models cannot be solved without a more accurate experimental survey.
- An extension of the potential to full scale has been done from experimental results. The capture ratio is low, but many perspectives of amelioration are to be considered. The inter-dependency of parameters renders a final estimation difficult.
- It seems possible to avoid losing energy theoretically, but at the moment not technically. The comparison of cost-efficiency with other wave energy converters is not so easy and no final conclusion is possible.
- All in all it is only a very first overview of a new technology and the order of magnitude of the potential let think that it is worthy to carry on researching on the field.

C. Recommendations for further work

1. First phase

- A raw cost-efficiency survey is first needed to prove the advantages of such a concept to justify further investigations.

- A more accurate estimation of the actual potential has to be done, numerically and experimentally. The experiments should pay attention to uncertainties, particularly no waves propagating beyond the structure. A gate on the trough bottom is to be considered instead of a channel. A pump can also be used to study the effect of the net cross-shore discharge (see Svendsen & Hansen (1987)).
- The analytical models used in this survey are designed for breakwaters, i.e. steep reflective slopes and should only be used in this context. To analyze the whole process for mild slopes the open code SHORECIRC is suggested, together with the non-linear model COULWAVE in a second time for more accuracy.

2. Second phase

- The effect of real sea conditions has to be studied, particularly on the transmission coefficient which has a key role in both the set-up and the cross-shore discharge. The same requirements apply to the modeling of reformed waves breaking on the second barrier.
- The turbine has to be developed
- The concept of an array of membranes over the surf zone should be analyzed into details
- Finally a real cost-efficiency analysis must be done before considering larger scale experiments

References

AAGAARD, T., GREENWOOD, B. and NIELSEN, J., 1997. Mean currents and sediment transport in a rip channel. *Marine Geology,* **140**(1-2), pp. 25-45.

BASCO, D.R. and YAMASHITA, T., 1987. Toward a simple model of the wave breaking transition region in surf zones. 1987, *Proceedings of the 20th Coastal Engineering Conference* , pp. 955-970.

BATTJES, J.A., 1974. SURF SIMILARITY. *PROC.14TH ASCE COASTAL ENGNG.CONF.(COPENHAGEN, DENMARK),* **1**, pp. JUNE 24-28, 1974.

BELLOTTI, G., 2004. A simplified model of rip currents systems around discontinuous submerged barriers. *Coastal Engineering,* **51**(4), pp. 323-335.

BLENKINSOPP, C.E. and CHAPLIN, J.R., 2008. The effect of relative crest submergence on wave breaking over submerged slopes. *Coastal Engineering,* **55**(12), pp. 967-974.

BOWEN,A.J.,1969.Rip currents: theoretical investigations. *Journal of geophysical research*, **74**(23), pp. 5467-5478.

BUCCINO, M. and CALABRESE, M., 2007. Conceptual approach for prediction of wave transmission at low-crested breakwaters. *Journal of Waterway, Port, Coastal and Ocean Engineering,* **133**(3), pp. 213-224.

CALABRESE, M., BUCCINO, M. and PASANISI, F., 2008. Wave breaking macrofeatures on a submerged rubble mound breakwater. *Journal of Hydro-Environment Research,* **1**(3-4), pp. 216-225.

CALABRESE, M., VICINANZA, D. and BUCCINO, M., 2008. 2D Wave setup behind submerged breakwaters. *Ocean Engineering,* **35**(10), pp. 1015-1028.

CASTELLE, B., BONNETON, P., SÉNÉCHAL, N., DUPUIS, H., BUTEL, R. and MICHEL, D., 2006. Dynamics of wave-induced currents over an alongshore non-uniform multiple-barred sandy beach on the Aquitanian Coast, France. *Continental Shelf Research,* **26**(1), pp. 113-131.

CHABAUD,V.,BEAUSSEAULT,A.,BREIVIK,S.R.,GRIS,C.,2009. Artificial Surf Zone: How to extract energy from wave-induced currents. Norwegian University of Science and Technology, Trondheim, Norway.

CHANG, H.-. and LIOU, J.-., 2007. Long wave reflection from submerged trapezoidal breakwaters. *Ocean Engineering,* **34**(1), pp. 185-191.

CHOW, V.T., 1959. Open Channel Hydraulics. *Mc Graw Hill*.

DALLY, W.R., 1992. Random breaking waves: Field verification of a wave-by-wave algorithm for engineering application. *Coastal Engineering,* **16**(4), pp. 369-397.

DALRYMPLE, R.A., 1978. Rip currents and their causes. *In: International Conference of Coastal Engineering*, ASCE, Hamburg, pp. 1414–1427.

DALRYMPLE, R.A., Dean, R.G., 1971. Piling-up behind low and submerged permeable breakwaters. Discussion note on Diskin et al. (1970). *Journal of Waterways and Harbors Division WW2*, 423–427.

DEAN, R.G.; DALRYMPLE, R.A. (1991). Water wave mechanics for engineers and scientists. *Advanced Series on Ocean Engineering. **2**. Singapore: World Scientific*.

DISKIN,M.H.,VADJA,M.,L,AMIR,I.,1970.Piling-up behind low and submerged permeable breakwater. *Journal of the waterways and harbors division*, ASCE Proceedings pp.359-371.

DRØNEN, N., KARUNARATHNA, H., FREDSØE, J., MUTLU SUMER, B. and DEIGAARD, R., 2002. An experimental study of rip channel flow. *Coastal Engineering,* **45**(3-4), pp. 223-238.

FREDSØE,J.,DEIGAARD,D.,1992.Mechanics of coastal sediment transport. *World Scientific, Advanced Series on Ocean Engineering.*

FRENCH,R.,1985.Open-Channel Hydraulics. McGRAW-HILL, Civil Engineering Series.

FURUKAWA, A., WATANABE, S., MATSUSHITA, D. and OKUMA, K., 2010. Development of ducted Darrieus turbine for low head hydropower utilization. *Current Applied Physics,* **10**(2 SUPPL.), pp. S128-S132.

GODA, Y., 2004. A 2-D random wave transformation model with gradational

breaker index. *Coastal Engineering*, **46** (1), pp. 1 –38.

GODA, Y., 2006. Examination of the influence of several factors on longshore current computation with random waves. *Coastal Engineering,* **53**(2-3), pp. 157-170.

GODA, Y., 2008. Wave setup and longshore currents induced by directional spectral waves: Prediction formulas based on numerical computation results. *Coastal Engineering Journal,* **50**(4), pp. 397-440.

GREENWOOD, B. and OSBORNE, P.D., 1990. Vertical and horizontal structure in cross-shore flows: An example of undertow and wave set-up on a barred beach. *Coastal Engineering,* **14**(6), pp. 543-580.

HAAS, K.A., SVENDSEN, I.A., HALLER, M.C. and ZHAO, Q., 2003. Quasi-three-dimensional modeling of rip current systems. *Journal of Geophysical Research C: Oceans,* **108**(7), pp. 10-1.

HALLER, M.C., DALRYMPLE, R.A. and SVENDSEN, I.A., 2002. Experimental study of nearshore dynamics on a barred beach with rip channels. *Journal of Geophysical Research C: Oceans,* **107**(6), pp. 14-1-14-21.

HANSEN, J.B., 1990. Periodic waves in the surf zone: Analysis of experimental data. *Coastal Engineering,* **14**(1), pp. 19-41.

HANSEN, J.B. and SVENDSEN, I.A., 1985. Theoretical and experimental study of undertow. 1985, *Proceedings of the 19th Coastal Engineering Conference* , pp. 2246-2262.

HANSEN, J.B. and SVENDSEN, I.A., 1987. Experimental investigation of the wave and current motion over a longshore bar. 1987, *Proceedings of the 20th Coastal Engineering Conference* , pp. 1166-1179.

JOHNSON, H.K., KARAMBAS, T.V., AVGERIS, I., ZANUTTIGH, B., GONZALEZ-MARCO, D. and CACERES, I., 2005. Modeling of waves and currents around submerged breakwaters. *Coastal Engineering,* **52**(10-11), pp. 949-969.

JONES, R.W., 2002. A method for comparing the performance of open channel velocity-area flow meters and critical depth flow meters. *Flow Measurement and Instrumentation,* **13**(5-6), pp. 285-289.

KAMPHUIS,J.W.,2000. An introduction to coastal engineering and management. World Scientific, Advanced Series on Ocean Engineering.

KEE, S.T. and KIM, M.H., 1997. Flexible membrane wave barrier. II: Floating/submerged buoy-membrane system. *Journal of Waterway, Port, Coastal and Ocean Engineering,* **123**(2), pp. 82-90.

KHAN, M.J., BHUYAN, G., IQBAL, M.T. and QUAICOE, J.E., 2009. Hydrokinetic energy conversion systems and assessment of horizontal and vertical axis turbines for river and tidal applications: A technology status review. *Applied Energy,* **86**(10), pp. 1823-1835.

KRAMER, M. and FRIGAARD, P., 2002. Efficient Wave Energy Amplification with Wave Reflectors, 2002, *Proceedings of The Twelfth International Offshore and Polar Engineering Conference*, pp. 707-712.

KURIYAMA, Y., 2010. A one-dimensional parametric model for undertow and longshore current velocities on barred beaches. *Coastal Engineering Journal,* **52**(2), pp. 133-155.

LONGUET-HIGGINS, M.S. and STEWART, R.W., 1964. Radiation stresses in water waves; a physical discussion, with applications. *Deep-Sea Research and Oceanographic Abstracts,* **11**(4), pp. 529-562.

LOVELESS, J.H., DEBSKI, D. and MACLEOD, A.B., 1998. Sea level set-up behind detached breakwaters. *Proceedings of the Coastal Engineering Conference,* **2**, pp. 1665-1678.
MACMAHAN,J.H.,THORNTON,E.B.,Reniers,J.H.M,2006. Rip current review. *Coastal Engineering,* **53**(1), pp. 191-208.

MCKEE, W.D., 1994. Reflection of water waves by a weak rapidly varying shearing current, *Wave Motion*, 20(2), pp. 143-149.

MEI, C.C., 1983. The applied dynamics of ocean surface waves. *Singapore: World Scientific.*

MICHE, R., 1944. Mouvements Ondulatoires des Mers en Profondeur Constante et Décroissante, *Ann, des ponts et Chaussées*, pp 25-78, 131-164, 270-292, 369-406.

MUNK, W.H., 1949. The Solitary Wave Theory and its Application to Surf Problems. *Ann. New York Acad. Of Science*, 51:376-424.

NORTEK AS, 2009. Vectrino user guide.

OSTROWSKI ,R., PRUSZAK ,Z., ROZYNSKI ,G., SZMYTKIEWICZ M.,2003. Field studies and modeling of interaction between nearshore currents and barred coast. *International Conference on Estuaries and Coasts*, November 9-11, 2003, Hangzhou, China.

PELAMIS WAVE POWER website http://www.pelamiswave.com/

PEREGRINE, D. H. 1976, Interaction of water waves and currents, *Adv. Appl. Mech.*, 16, 9–117

RENIERS, A.J.H.M. and BATTJES, J.A., 1997. A laboratory study of longshore currents over barred and non-barred beaches. *Coastal Engineering,* **30**(1-2), pp. 1-22.

SCHLICHTING, H., GERSTEN, K., 1999. Boundary Layer Theory. *Springer*.

SHIRLAL, K.G., RAO, S. and MANU, 2007. Ocean wave transmission by submerged reef-A physical model study. *Ocean Engineering,* **34**(14-15), pp. 2093-2099.

SOLDINI, L., LORENZONI, C., BROCCHINI, M., MANCINELLI, A. and CAPPIETTI, L., 2009. Modeling of the wave setup inshore of an array of submerged breakwaters. *Journal of Waterway, Port, Coastal and Ocean Engineering,* **135**(2), pp. 38-51.

STIVE, M.J.F. and WIND, H.G., 1986. Cross-shore mean flow in the surf zone. *Coastal Engineering,* **10**(4), pp. 325-340.

SVENDSEN, I.A., MADSEN, P.A. and BUHR HANSEN, J., 1979. wave characteristics in the surf zone. *Proceedings of the Coastal Engineering Conference,* **1**, pp. 520-539.

SVENDSEN, I.A., 1984. Mass flux and undertow in a surf zone. *Coastal Engineering,* **8**(4), pp. 347-365.

SVENDSEN, I.A., 1984. Wave heights and set-up in a surf zone. *Coastal Engineering,* **8**(4), pp. 303-329.

SVENDSEN, I.A., 2006. Introduction to Nearshore Hydrodynamics. *Adv. Series on Ocean Engineering, World Scientific.*

SVENDSEN, I.A. and HANSEN, J.B., 1987. interaction of waves and currents over a longshore bar. 1987, *Proceedings of the 20th Coastal Engineering Conference*, pp. 1580-1594.

SVENDSEN, I.B. and BUHR HANSEN, J., 1988. Cross-shore currents in surf-zone modelling. *Coastal Eng.,* 12: 23-42.

SVENDSEN,I.A.,HAAS,K,ZHAO,Q. Quasi-3D Nearshore Circulation Model SHORECIRC Versio 2.0 User Guide. Center for Applied Coastal Research, University of Delaware.

SVENDSEN, I.A. and PUTREVU, U., 1993. Surf zone wave parameters from experimental data. *Coastal Engineering,* **19**(3-4), pp. 283-310.

TAJIMA, Y. and MADSEN, O.S., 2006. Modeling near-shore waves, surface rollers, and undertow velocity profiles. *Journal of Waterway, Port, Coastal and Ocean Engineering,* **132**(6), pp. 429-438.

THORNTON, E.B. and GUZA, R.T., 1983. Transformation of wave height distribution. *Journal of Geophysical Research,* **88**(C10), pp. 5925-5938.

TSAI, C.-., CHEN, H.-., HWUNG, H.-. and HUANG, M.-., 2005. Examination of empirical formulas for wave shoaling and breaking on steep slopes. *Ocean Engineering,* **32**(3-4), pp. 469-483.

VAN DER MEER, J.W. and ANGREMOND, K., 1992. Wave transmission at low-crested structures.

VAN DER MEER, J.W., BRIGANTI, R., ZANUTTIGH, B. and WANG, B., 2005. Wave transmission and reflection at low-crested structures: Design formulae, oblique wave attack and spectral change. *Coastal Engineering,* **52**(10-11), pp. 915-929.

VEISKARAMI, M., NESHAEI, M.A.L. and MEHRDAD, M.A., 2009. The effect of beach reflection on undertow. *Iranian Journal of Science and Technology, Transaction B: Engineering,* **33**(1), pp. 49-60.

VICINANZA, D., CÁCERES, I., BUCCINO, M., GIRONELLA, X. and CALABRESE, M., 2009. Wave disturbance behind low-crested structures: Diffraction and overtopping effects. *Coastal Engineering,* **56**(11-12), pp. 1173-1185.

WANG, B., CHADWICK, A.J. and OTTA, A.K., 2008. Derivation and application of new equations for radiation stress and volume flux. *Coastal Engineering,* **55**(4), pp. 302-318.

WANG, B., OTTA, A.K. and CHADWICK, A.J., 2007. Transmission of obliquely incident waves at low-crested breakwaters: Theoretical interpretations of experimental observations. *Coastal Engineering,* **54**(4), pp. 333-344.

WAVE DRAGON website http://www.wavedragon.net/

WOLF, J. and PRANDLE, D., 1999. Some observations of wave-current interaction. *Coastal Engineering,* **37**(3-4), pp. 471-485.

XIA,H.,XIA,Z.,ZHU,L.,2004. Vertical variation in radiation stress and wave-induced current. *Coastal Engineering,* **51**(4), pp. 309-321.

ZHENG,J.,H.,ZHANG,C.M.,MASE,H.,2008. Incorporation of surface rollers in modeling wave-driven coastal currents. *Chinese-German Joint Symposium on Hydraulic and Ocean Engineering*, August 24-30, 2008, Darmstadt.

XII. Appendices

A. Calibration of the wave probes

The linear coefficient obtained Figure XII-1. is set in the software Catman.

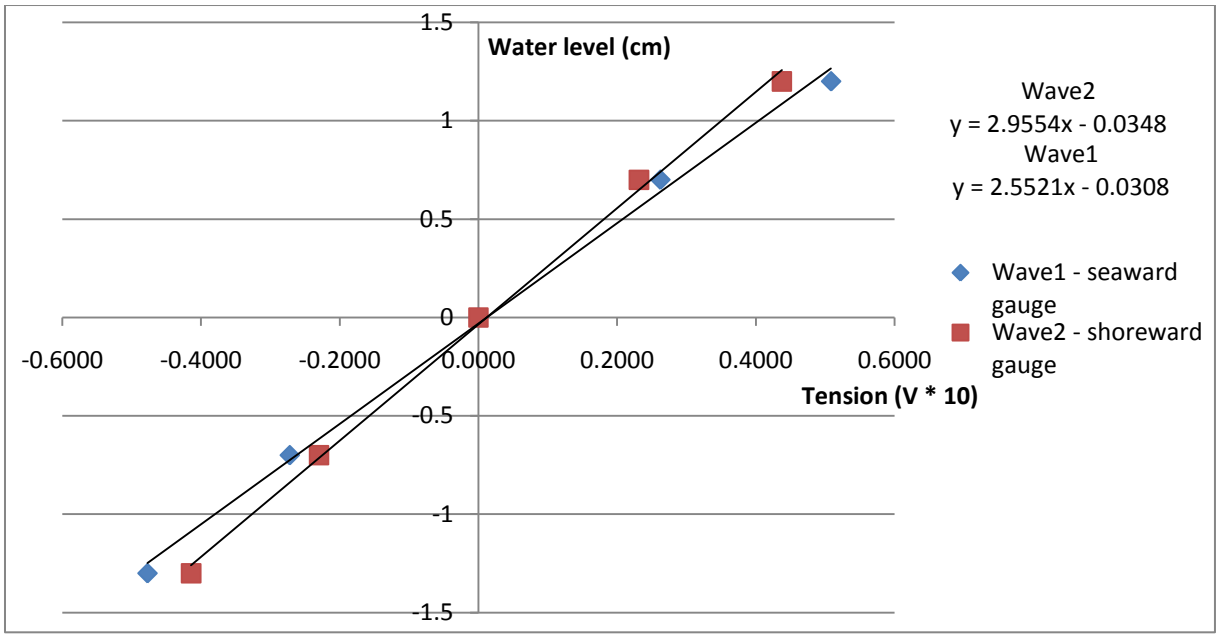

Figure XII-1: Calibration of the wave probes

B. Time series

An example of data acquisition from the seaward wave probe is shown on Figure XII-2 and Figure XII-2.

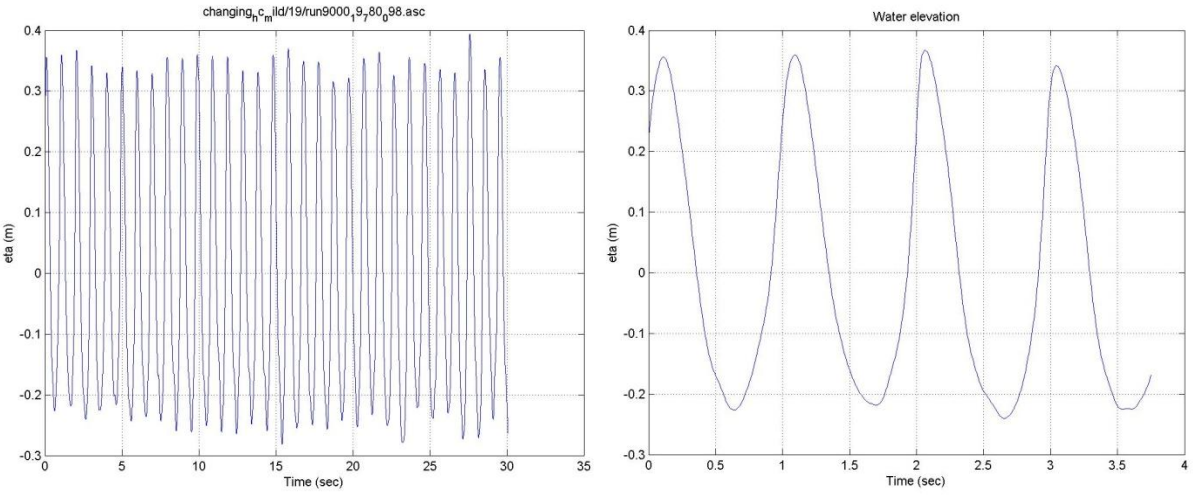

Figure XII-2: example of 2D time series from seaward probe, global (left) and zoomed (right).

We notice the envelope caused by wave reflection, mainly from the absorbing beach (second breaking after the barrier). Figure XII-2 show that the wave profile is not sinusoidal, changing the wave steepness. It is normally induced by wave shoaling in the real case. However, there could be a contribution of wave splitting (under and beyond the structure) that could significantly change the

wave steepness and therefore the results. Indeed there is no way to measure the wave length and it is calculated theoretically, only from wave shoaling.

Similar results for the shoreward probe are plotted Figure XII-3.

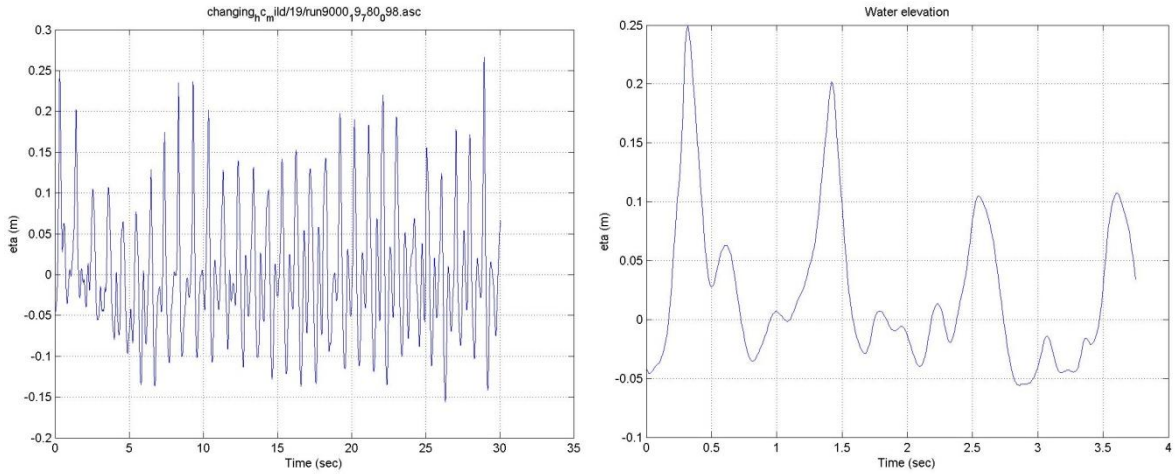

Figure XII-3: of 2D time series from shoreward probe, global (left) and zoomed (right).

We notice a much more chaotic behavior. It is obvious from Figure XII-3 that the relatively short duration of the tests induced uncertainty on the mean values. From Figure XII-3 we can clearly see the wave set-up (mean water level elevation).

A generation of higher harmonic waves (multiples of the initial wave frequency) was observed. It is shown on an example of wave spectrum from the two wave probes Figure XII-4. We can notice a weak second harmonic generation for the seaward probe, due to wave splitting (over and beyond the structure). Breaking induces a much stronger generation of higher harmonics as seen on the spectrum from the shoreward probe.

It is a well-known phenomenon (see for example Calabrese et al. (2008)). The program WAVAN used in the code calculates the significant wave height from the spectrum, so takes into account these higher harmonic waves.

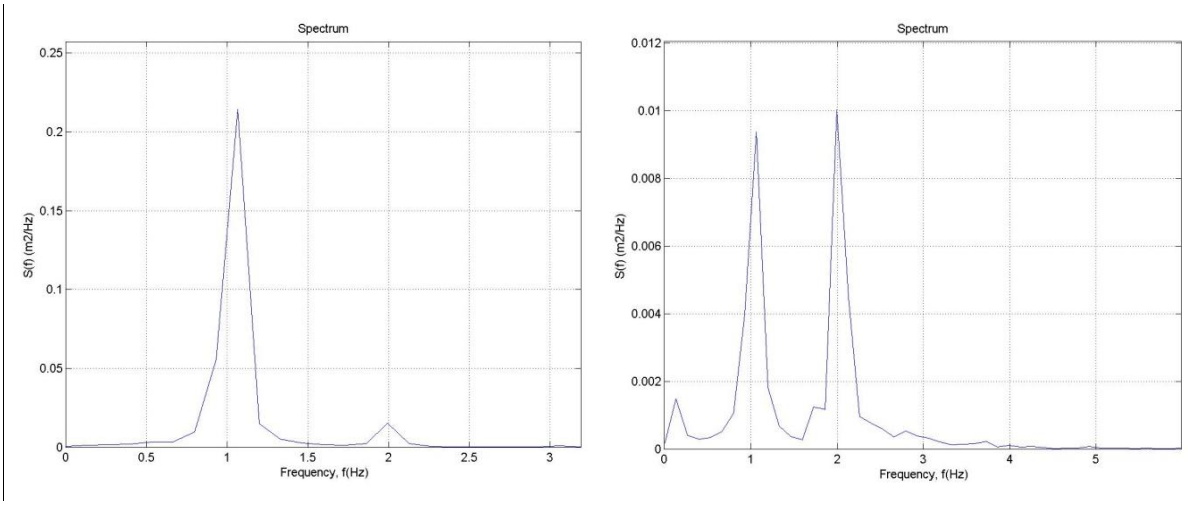

Figure XII-4: example of wave spectra, seaward (left) and shoreward (right) probes.

C. Velocity data acquisition

For each test the velocity was recorded for ca. 30 seconds. An example of data acquisition is presented Figure XII-5. We can notice the periodic oscillations of the velocity due to waves in the channel. Indeed the absorbing beach was not perfect. However it should not change the mean value. A strong turbulence is hiding these oscillations.

On this record like on many others, some noise was observed. Some records were too noisy to be used and were removed from the data set. The others were filtered using the following law:

As long as the standard deviation is higher than a given criterion, if the relative difference between the instantaneous and the mean velocities is higher than another given criterion, the value is removed. Such iterations were needed because the bad values were falsifying the mean value. The filtering stops when the standard deviation is lower than approximately twice the observed periodic amplitude of the velocity.

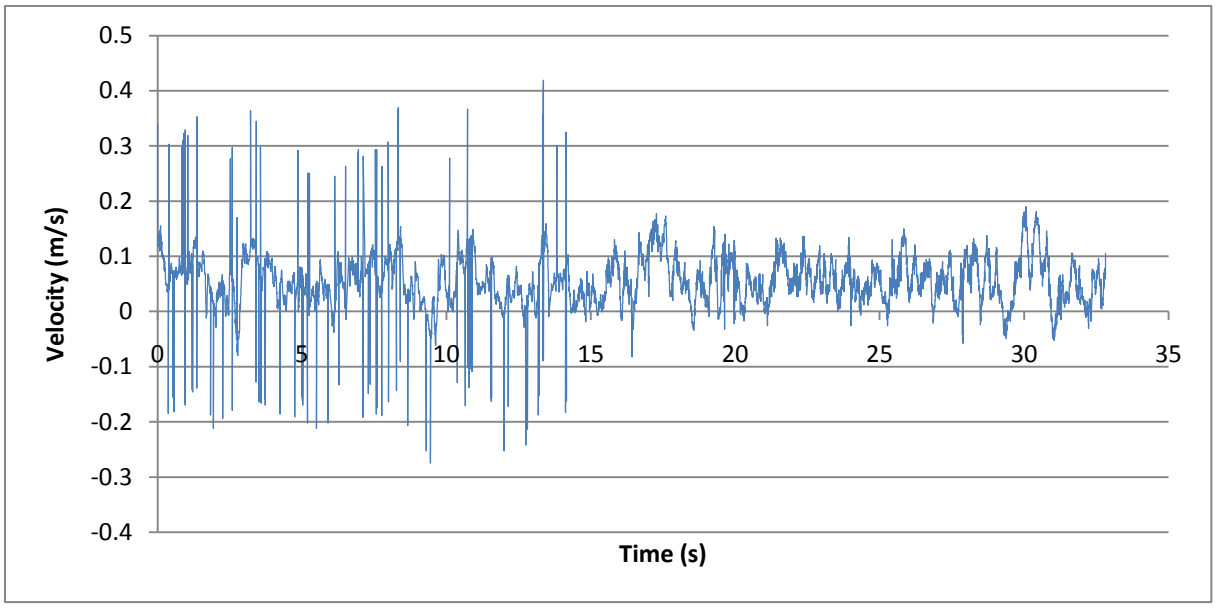

Figure XII-5: Example of velocity record with weak noise

D. Basics on Linear Wave Theory (LWT)

LWT is a potential theory first found by Airy in the 19th century. It is based on the assumption that the wave height is small compared to the wave length, therefore only first order terms of the ratio wave height/wave length are taken into account. Resulting waves are sinusoidal and can be represented analytically.

1. Generalities

The velocity potential is expressed as:

$$\phi = -\frac{H}{2}\frac{g}{\omega}\frac{\cosh(kz)}{\cosh(kh)}\sin(\omega t - kx)$$

In which:

- H is the wave height
- ω is the wave frequency with $\omega = \frac{2\pi}{T}$ and T the wave period
- k is the wave number with $k = \frac{2\pi}{L}$ and L the wave length
- g is the gravity constant
- h is the local depth
- t is the time and x the position
- z is the vertical position, pointed upward and with the origin at the bottom

The wave number and frequency are linked by the dispersion relation (non-linear):

$$\omega^2 = gk \tanh kh$$

All variables can then be derived:

Water surface elevation: $\eta = \frac{H}{2} cos\ (\omega t - kx)$

Phase celerity: $c = \frac{\omega}{k} = \sqrt{\frac{g}{k} tanh(kh)}$

Horizontal particle velocity: $u = \frac{\pi H}{T} \frac{\cosh(kz)}{\sinh(kh)}\ cos\ (\omega t - kx)$

Vertical particle velocity: $w = -\frac{\pi H}{T} \frac{\sinh(kz)}{\sinh(kh)}\ sin\ (\omega t - kx)$

Pressure: $p = \rho g \frac{H}{2} \frac{\cosh(kz)}{\cosh(kh)} sin(\omega t - kx) + \rho g(h - z)$

For simplicity we will take x equal to 0, i.e. we set the local point of interest as the origin. This does not change equations since we always take the averaged value over one period.

2. Wave Energy

Wave energy is the averaged sum of kinetic and potential energy over one wave period (or wave length).

$$\overline{E_{pot}} = \frac{1}{T} \int_0^T \frac{1}{2} \rho g \eta^2\, dx = \frac{\rho g \overline{\eta^2}}{2}$$

$$\overline{E_{kin}} = \frac{1}{2} \rho g \overline{\int_0^{h+\eta} (u^2 + w^2)\, dz}$$

where E_{pot} is the potential energy and $\overline{variable}$ means the average of the variable over one period.

From LWT equations we can derive:

$$E = \overline{E_{pot}} + \overline{E_{kin}} = \frac{1}{16} \rho g H^2 + \frac{1}{16} \rho g H^2 = \frac{1}{8} \rho g H^2$$

E is the wave energy per unit of length of the wave crest in W/m.

Wave energy does not propagate with phase celerity, but with group velocity defined as:

$$c_g = c + k \frac{dc}{dk} = \frac{c}{2} \left[1 + \frac{2kh}{\sinh(2kh)}\right] = \frac{c}{2} [1 + G]$$

G is a function of kh and accounts for wave propagation in shallow water. In deep water $\lim_{kh\to\infty} G = 0$ and in shallow water $\lim_{kh\to 0} G = 1$.

Therefore the energy flux is given by:

$$E_f = E\, c_g$$

3. Radiation stress theory

Ocean waves carry an excess flow of momentum, which is defined as radiation stresses (Longuet-Higgins and Stewart, 1964). This flux of momentum is formed by two contributions: one due to the wave-induced velocities of the water particles and another one due to pressure.

The contribution from the wave motion (i.e. from the velocities, or dynamic pressure) in a vertical cross-section can be written:

$I_m = \int_0^{h+\eta} \rho u^2\, dz$

And the one from the hydrostatic pressure:

$I_p = \int_0^{h+\eta} p\, dz$

The radiation stress tensor $[S]$ is defined as the excess of momentum flux i.e. the time averaged momentum flux in the presence of waves minus the mean flux in still water over one wave period.

In a Cartesian 2D system of coordinates (x, y) where x is the wave propagation direction, we have:

The x, or cross-shore component of radiation stresses $S_{xx} = \overline{I_m} + \overline{I_p} - I_{p0}$

The y, or alongshore component: $S_{yy} = \overline{I_p} - I_{p0}$

with $I_{p0} = \int_0^{h+\eta} p_0\, dz$, where $p_0 = \rho g(h - z)$ is the hydrostatic pressure for still water.

From LWT equations, we get:

$$[S] = \begin{bmatrix} S_{xx} & 0 \\ 0 & S_{yy} \end{bmatrix} = \begin{bmatrix} \frac{1}{8}\rho g H^2 \left(\frac{2kh}{\sinh 2kh} + \frac{1}{2}\right) & 0 \\ 0 & \frac{1}{8}\rho g H^2 \left(\frac{kh}{\sinh 2kh}\right) \end{bmatrix} = \begin{bmatrix} \frac{1}{2}E(1+2G) & 0 \\ 0 & \frac{1}{2}EG \end{bmatrix}$$

If now the coordinate system does not coincide with wave propagation, i.e. waves propagate with an angle θ with respect to the x axis, from a force balance on a small vertical triangular column we get:

$$[S] = \begin{bmatrix} S_{xx} & S_{xy} \\ S_{yx} & S_{yy} \end{bmatrix} = \begin{bmatrix} (1+G)\cos^2\theta + G & (1+G)\sin\theta\cos\theta \\ (1+G)\sin\theta\cos\theta & (1+G)\sin^2\theta + G \end{bmatrix}$$

4. Wave drift

The wave drift is the time averaged mass carried by organized ocean waves. From an Eulerian point of view it can be written:

$$q_{drift} = \overline{\int_0^{h+\eta} u\, dz}$$

Below the wave trough level, it is obvious than $\bar{u} = 0$ because u varies harmonically in time. Therefore

$$q_{drift} = \overline{\int_{h-\frac{H}{2}}^{h+\eta} u\, dz}$$

By the mean of LWT (taking only the first order of $\frac{H}{L}$), which is not appropriate if waves are steep (non-sinusoidal), we can approximate u by its value at $z = h$.

Then we get $u = \frac{\pi H}{T} \frac{1}{\tanh(kh)}\, cos\,(\omega t)$

Which gives:

$$q_{drift} = \frac{H^2 \pi}{4T} \frac{1}{\tanh\,(kh)}$$

However as waves propagate in shallow water, their shape is not sinusoidal anymore and the expression above is wrong. Higher order (non linear) expressions should be used. The surface roller contributes also to onshore mass transport.

E. Details on major sources of uncertainty

1. Heave motion

Despite efforts to stiffen or add weight on different parts of the structure, the natural frequency in heave of the central plate of the structure was still quite close to those of waves.

It appeared therefore to depend strongly on wave frequency.

For the majority of tests where T=0.83 s a quite small motion was observed.

The uncertainty due to heave motion is very different regarding the probe:

- The seaward probe measured waves just over a thick beam which the plate was screwed to in several points, so absolute motion was small. However if the wave frequency approached the natural frequency of the structure, the deck which the probe was fixed to could move a little, leading to a non negligible relative motion. Its amplitude is estimated to 2 mm for such frequencies but negligible in most tests.

- The shoreward probe measured wave just in the middle of the structure and anchored points of the plate to the deck or the beams were quite far. A very big absolute motion (relative to the wave height) could be observed (up to 1 cm). However the probe was on purpose moving with the structure so the relative motion is negligible as shown in the following.

The amplitude of the heave motion η_3 as a function of the longshore position is represented on Figure XII-5, with the assumption of a parabolic mode shape for the structure. The board which holds the probe is fixed to the structure in three points and its motion is given by the motion of the channel wall (parabolic motion along the board).

The mode shape is parabolic: $\eta_3(y) = ay^2 - aly = ay(y - l)$ since $\eta_3(0) = \eta_3(l) = 0$

l is the alongshore length = 1.9 m, a is a constant.

The board is fixed at a location $y_{board} = \frac{1.4}{1.9} l = 0.74\, l$

Therefore $\eta_3(y_{board}) = -a\ 0.19\ l^2$

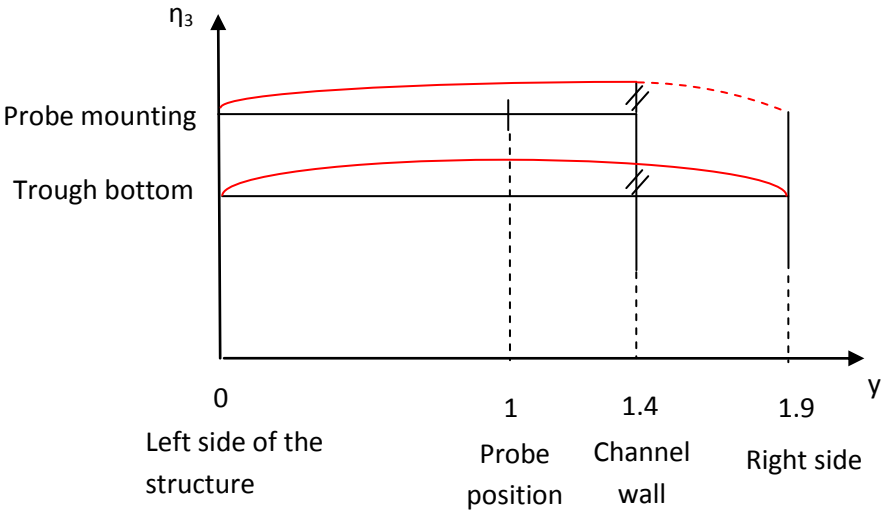

Figure XII-6: Mode shape of the structure under heave motion

Along the board $\eta_3(y) = \frac{\eta_3(y_{board})}{y_{board}}(-\frac{y^2}{y_{board}} + 2y)$ hence $\eta_3(y_{probe}) = -a\,\frac{0.19\,l}{0.74} * \frac{0.74\,l}{1.4}\left(-\frac{1}{1.4} + 2\right) = -0.17\,a\,l2$

Now let's calculate the mean value of the motion along the board up to the channel, which gives the mean variation in wave height:

$$\eta_{3\,mean} = \frac{1}{y_{board}}\int_0^{y_{board}} ay(y-l)dl = a\left(\frac{{y_{board}}^2}{3} - \frac{y_{board}}{2}l\right) = -0.19\,a\,l^2$$

The corresponding error on the mean transmitted wave height is therefore $\Delta H = \pm 0.02\,a\,l^2$

In the worst cases the amplitude of η_3 is estimated to 1 cm. $a = -\frac{4*10}{l^2}$ so $\Delta H = \pm 0.8\,mm$

In most cases the error is negligible.

2. Wave reflection

The effect of reflected waves can be separated in two parts:

- Direct reflected waves. They propagate seaward, crossing the wave probes right after they are reflected. The reflective items are the barrier and the absorbing beach (second breaking).
- Indirect reflected waves. They have been reflected once by the structure, then by the wave maker and propagate shoreward, adding to the incident wave field. The reflective items are the same as for direct reflection plus the structure itself, from the splitting in incident wave energy (over and beyond the structure, see appendix I).

Reflection coefficients are in general difficult to estimate.

Reflection by energy splitting is caused by phase-locked waves and information can be found in studies on horizontal plate breakwaters. However, it was expected to be strongly coupled with the motions of the structure, and therefore with its resonance frequency. Indeed in was observed that it depended highly on the wave period.

To avoid indirect reflection, a reflection test has been done for 2D experiments, and a period leading to low structure reflection has been chosen for 3D tests.

Direct reflection was inevitable, and an attempt of quantification is given below.

Reflection test

Procedure: Data acquisition by wave probes is launched while the water is still. Waves are generated for a short period (ca. 10s). Probes are still acquiring data until reflected waves from the generated wave train hit the structure.

Results: The criterion on the test duration to avoid reflected waves is mainly dependent on wave period. A duration lower than 40s was expected to avoid reflected waves whatever the period.

Direct reflection

A good approximation of reflection coefficients on uniform sloping beaches was proposed by Battjes (1974):

$$K_r = 0.1{\xi_0}^2$$

And was been validated for steep slopes by Tsai et al. (2004).

However it is not really appropriate for barred beaches, and should overestimate K_{ri} in our case.

If we take the approximate wave steepness from 3D experiments, we get:

-From the seaward slope of the barrier: $K_{ri} = 0.1 * \left(\frac{1}{8*\sqrt{0.04}}\right)^2 = 0.04$ (mild slope)

$K_{ri} = 0.1 * \left(\frac{1}{2*\sqrt{0.04}}\right)^2 = 0.62$ (steep slope)

- For the absorbing beach: $K_{rs} = 0.1 * \left(\frac{1}{6*\sqrt{0.02}}\right)^2 = 0.14$

The very high K_{ri} for steep slopes is not validated by observations and measured values of the transmission coefficient.

All in all the uncertainty for the seaward probe is $\frac{\Delta H_i}{H_i} = \pm(K_{ri} + K_t\, K_{rs})$ approximated as ± 0.1 for a mild slope and higher (but unquantifiable) for a steep slope. For the shoreward probe $\frac{\Delta H_t}{H_t} = \pm K_{rs} = \pm 0.14$.

It is not negligible and could have influenced significantly the measurements, depending on the location of the wave probe within the reflection envelope.

F. Experimental procedure of 2D tests

The influence of the following parameters on the 2D set-up is checked:

- Relative crest depth of the barrier $\frac{h_c}{H_i}$
- Wave steepness $\frac{H_i}{L_i}$
- Relative crest width $\frac{B}{H_i}$
- Seaward slope of the barrier $\tan\alpha$

h_c is set by changing the water level in the tank. B is constant. $L_i = \frac{2\pi}{k_i}$, k_i is calculated from the wave dispersion relationship from h_i and ω.

It is preferable to get the variation of the set-up against one parameter while the others remain constant.

The slope is first mild: $\tan\beta = \frac{1}{8}$

$\delta\left(\frac{h_c}{H_i}\right)$ is obtained for $\frac{B}{H_i}$ = 1, 1.4 and 2.

$\delta\left(\frac{B}{H_i}\right)$ is obtained for $\frac{h_c}{H_i} = 0.5$

In the two cases above H_i is defined by the constant parameter for several values of h_c, ω is then chosen to keep $\frac{H_i}{L_i} = 0.04$ for each test.

For a constant value of h_c, ω is modified to get $\delta\left(\frac{H_i}{L_i}\right)$, keeping in mind that K_i (presented in appendix I) and consequently H_i vary also with ω.

We can then change the slope $\tan\beta = \frac{1}{2}$

$\delta\left(\frac{h_c}{H_i}\right)$ is then obtained for $\frac{B}{H_i} = 1.4$

G. List of 2D tests

slope =1/8 standard configuration

Test number	Hg	T	hc	Purpose	Comments
1	5	1.03	17	first tests	
2	4	0.92	17	first tests	
3	3	0.8	17	first tests	
4	2	0.65	17	first tests	
5	1.5	0.57	17	first tests	
6	6	1.13	17	first tests	
7	7	1.22	17	first tests	
8	8	1.31	17	first tests	
9	6	1.13	18	Abac for Kd	
10	7	1.22	18	Abac for Kd	
11	5	1.22	18	Abac for Kd	
12	3	0.8	18	Abac for Kd	
13	3	1	18	Abac for Kd	
14	4.66	0.82	25	B/Hi=1	
15	6.77	0.98	25	B/Hi=1	
16	7.4	0.98	25	B/Hi=1.4	
17	3.52	0.69	25	B/Hi=2	
18	8	1	25	hc/Hi=0.4	
19	9	1	25	hc/Hi=0.4	
20	3.8	0.69	25	B/Hi=2	

21	7.4	0.98	29	B/Hi=1	
22	5.76	0.83	29	B/Hi=1.4	
23	3.2	0.69	29	B/Hi=2	
24	12	1.08	29	hc/Hi=0.4	
25	12	0.98	29	B/Hi=1	screw added, less motion
26	10	1.08	29	hc/Hi=0.4	
27	9.5	1.08	29	hc/Hi=0.4	
28	7.3	0.98	32	B/Hi=1	
29	5.28	0.83	32	B/Hi=1.4	Non ASCII data
30	3.2	0.69	32	B/Hi=2	Non ASCII data
31	11	1.14	32	hc/Hi=0.4	
32	4.8	0.83	32	B/Hi=1.4	
33	7.5	0.98	27	B/Hi=1	
34	4.9	0.83	27	B/Hi=1.4	
35	3.2	0.69	27	B/Hi=2	
36	8.7	1.04	27	hc/Hi=0.4	
37	9.5	1.04	27	hc/Hi=0.4	
38	7.6	0.98	22	B/Hi=1	Non ASCII data
39	5	0.83	22	B/Hi=1.4	
40	3.2	0.69	22	B/Hi=2	
41	6.8	0.94	22	hc/Hi=0.4	
42	7.8	0.98	19	B/Hi=1	
43	5	0.83	19	B/Hi=1.4	
44	3.3	0.69	19	B/Hi=2	
45	5.7	0.87	19	hc/Hi=0.4	
46	8	0.98	15	B/Hi=1	
47	5.1	0.83	15	B/Hi=1.4	
48	3.3	0.69	15	B/Hi=2	
49	4.3	0.77	15	hc/Hi=0.4	
50	8.2	0.98	11	B/Hi=1	Non ASCII data
51	5.3	0.83	11	B/Hi=1.4	
52	3.4	0.69	11	B/Hi=2	
53	3	0.66	11	hc/Hi=0.4	
54	4.5	0.6	15	Hi/Li=0.076	
55	4.7	0.7	15	Hi/Li=0.056	
56	5	0.8	15	Hi/Li=0.043	
57	5.4	0.9	15	Hi/Li=0.034	
58	5.8	1	15	Hi/Li=0.027	
59	5.8	1.1	15	Hi/Li=0.023	
60	4.9	0.75	15	Hi/Li=0.049	
61	7	1.3	15	Hi/Li=0.017	
62	4.6	0.65	15	Hi/Li=0.065	
63	6.4	1.3	15	Hi/Li=0.017	
64	5.4	1.3	15	Hi/Li=0.017	

trough depth changed

Test number	Hg	T	hc	Purpose	Comments
65	5.1	0.83	15	ht ≠	
66	6	1.13	17	ht ≠	
67	5	0.83	19	ht ≠	
68	5	0.83	22	ht ≠	
69	4.66	0.82	25	ht ≠	

friction added

70	4.66	0.82	25	friction ≠	
71	6.77	0.98	25	friction ≠	
72	7.4	0.98	25	friction ≠	
73	3.52	0.69	25	friction ≠	
74	8	1	25	friction ≠	
75	9	1	25	friction ≠	Non ASCII data
76	3.8	0.69	25	friction ≠	

friction added slope 1/2

79	4.66	0.82	25	friction ≠	

Transient test with opening of the gate

98	3.5	0.69	-1	transient test	t open=16 s
100	3.4	0.69	13.5	transient test	MWL stable after 5s, t open=23s

slope=1/2 standard configuration

Test number	Hg	T	hc	Purpose	Comments
77	3.52	0.69	25	B/Hi=2	
78	4.66	0.82	25	B/Hi=1.4	Undertow visible
80	3.2	0.69	29	B/Hi=2	High reflection
81	3.2	0.69	32	B/Hi=2	
82	3.2	0.69	27	B/Hi=2	
83	4.9	0.83	27	B/Hi=1.4	
84	3.2	0.69	22	B/Hi=2	
85	5	0.83	22	B/Hi=1.4	
86	3.3	0.69	19	B/Hi=2	
87	5	0.83	19	B/Hi=1.4	
88	3.3	0.69	17	B/Hi=2	Hg changed from the H/T model
89	6	1.13	17	B/Hi=1.4	hc may have moved
90	3.3	0.69	15	B/Hi=2	No file
91	5.1	0.83	15	B/Hi=1.4	No file
92	3.4	0.69	11	B/Hi=2	Bar lifted of 2 mm on a side and 4 mm on the other

93	5.3	0.83	11	B/Hi=1.4	
94	5.3	0.82	7	B/Hi=1.4	
95	3.4	0.69	7	B/Hi=2	
96	5.4	0.82	-1	B/Hi=1.4	
97	3.5	0.69	-1	B/Hi=2	Water level increasing during the test
99	3.4	0.69	13.5	B/Hi=1.4	

H. List of 3D tests

H=5.1 cm, T=0.83s, hc=15mm, full reflection conditions, duration ≈ 40s

slope=1/2, d=173mm (gate fully opened)

z=0.6h		z=0.2h		z=0.8h		z=0.9h	
y	comments	y	comments	y	comments	y	comments
20		184		80		40	
32		174		70		50	
42		164	weak noise	65		60	
30		154	noise	40		85	
40		139		30		90	
50	noise	134		20		100	
60	noise	124	weak noise	164	weak noise	30	
55	noise	114	noise	174		94	
65		104	weak noise	184		104	noise
70		94		189		124	weak noise
10	weak noise	84	noise	139		134	
10	weak noise	189		134	weak noise	154	
15		20		124	weak noise	164	noise
184		30		104		174	
174		40		94		184	
164		45	noise			189	
154	noise	65					
144	noise	70					
134		80					
124	weak noise						
114							
104							
94							
84	noise						
189							

slope=1/2, d=50mm

z=0.6h			
y	comments		
189		10	
174		30	noise
164	weak noise	25	

134	weak noise	40
139		65
124	weak noise	70
114	noise	80
104		
94	weak noise	
99		
20		

slope=1/2, all values of d

d	waves	y=184			y=70		
		z=0.6h	z=0.2h	z=0.8h	z=0.6h	z=0.2h	z=0.8h
5	x	x			x		
10		x			x		
15	x	x	x	x	x	x	x weak noise
20		x			x		
25	x	x	x	x	x	x	x
30	x	x	x	x	x	x	x
35	x	x	x	x	x	x	x
60	x	x			x		
70	x	x			x		
80	x	x	x	x	x	x	x
90	x						
100	x						
110	x	x	x	x	x	x	x
50	x						
173	x						

slope=1/8, all values of d

d	waves	y=184			y=70		
		z=0.6h	z=0.2h	z=0.8h	z=0.6h	z=0.2h	z=0.8h
8					x		
10	x				x		
15	x	x	x	x	x	x	x
20	x	x	x	x	x	x	x
30	x	x	x	x	x	x	x
50	x	x	x	x	x	x	x
80	x	x	x	x	x	x	x
110	x	x	x	x	x	x	x
173	x	x	x	x	x	x	x

I. Input, generated and incident wave heights

1. Definitions

The input wave height is what is entered in the software driving the wave maker.

The generated wave height is related to the wave really generated by the wave maker.

The incident wave height is related to the fraction of the wave which propagates on the structure, the other part propagating beyond.

2. On linking the input and generated wave heights

The input wave height equals the generated wave height when the water level in the tank is at its nominal height, i.e 1m deep. As we make the water level change to change h_c, the generated wave height differs slightly from the input one.

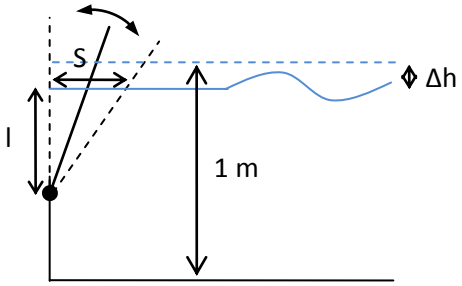

Figure XII-7: Flap type wave maker

Wave maker theory (see Dean & Dalrymple (1984)) has been used to link the two wave heights.

The problem is shown on Figure XII-7. The volume displaced by the flap is equal to the volume in the generated wave. Then $\frac{H_g}{S} = \frac{\sinh(k_g l)+k_g l}{2(\cosh(kl)-1)}$ where k_g is the generated wave number calculated from the dispersion relation $\omega^2 = gk_g \tanh(k_g(1-\Delta h))$. The stroke S is the one needed to generate the input wave height H_{input} when $\Delta h = 0$.

Therefore $S = H_g \frac{\sinh(k_g l)+k_g l}{2(\cosh(k_g l)-1)} = H_{input} \frac{\sinh(k_0 h_0)+k_0 h_0}{2(\cosh(k_0 h_0)-1)} - \frac{\Delta h\, H_g \frac{\sinh(k_g l)+k_g l}{2(\cosh(k_g l)-1)}}{h}$ in which $h_0 = l + \Delta h$ and k_0 is calculated from $\omega^2 = gk_0 \tanh(k_0)$.

It gives $H_g \left(1 + \frac{\Delta h}{h}\right) \frac{\sinh(k_g l)+k_g l}{2(\cosh(k_g l)-1)} = H_{input} \frac{\sinh(k_0 h_0)+k_0 h_0}{2(\cosh(k_0 h_0)-1)}$

We introduce the wave maker coefficient $K_{WM} = \frac{H_g}{H_{input}} = \frac{l}{h_0} \frac{\sinh(k_0 h_0)+k_0 h_0}{\sinh(k_g l)+k_g l} \frac{\cosh(k_g l)-1}{\cosh(k_0 h_0)-1}$

3. On linking the incident wave and generated wave heights

The incident wave height can be found theoretically with the energy conservation principle, stating that the generated energy is equal to the sum of the energies propagating over and beyond the structure averaged over one period:

$$\overline{E_g} = \overline{E_i} + \overline{E_{beyond}}$$

The distance from the bottom to the seaward edge of the structure is named d and the depth of the tank h.

Energy is the sum of kinetic and potential energies:

$$\overline{E_g} = \underbrace{\left[\left(\overline{E_{kin}} + \overline{E_{pot}}\right)\right]_0^d}_{\overline{E_{beyond}}} + \underbrace{\left[\left(\overline{E_{kin}} + \overline{E_{pot}}\right)\right]_d^h}_{\overline{E_i}}$$

$\overline{E_{beyond}}$ is calculated in the following.

Potential energy

$\overline{E_{pot}} = \frac{1}{2}\rho g\overline{\eta^2}$ with η the wave amplitude at a depth z

$$\eta(z) = \int_0^t w\, dt = \frac{H}{2}\frac{\sinh(\mathrm{kz})}{\sinh(kh)}\cos(\omega t)$$

H is the generated wave height.

Then $\overline{E_{pot}} = \frac{1}{16}\rho g H^2 \frac{sinh^2(kd)}{\sinh^2(kh)}$

Kinetic energy

$\overline{E_{kin}} = \int_0^d \frac{1}{2}\rho\left(\overline{u^2} + \overline{w^2}\right)dz$ with u and w the horizontal and vertical particle velocities.

$$u = \frac{\pi H}{T}\frac{\cosh(\mathrm{kz})}{\sinh(kh)}\, cos\,(\omega t)$$

$$w = -\frac{\pi H}{T}\frac{\sinh(\mathrm{kz})}{\sinh(kh)}\, sin\,(\omega t)$$

So $\overline{E_{kin}} = \frac{1}{2}\rho\left(\frac{\pi H}{T}\frac{1}{\sinh(kh)}\right)^2 \int_0^d \left(cosh^2(kz)\overline{cos^2(\omega t)} + sinh^2(kz)\overline{sin^2(\omega t)}\right)dz$

With $\overline{cos^2(\omega t)} = \overline{sin^2(\omega t)} = \frac{1}{2}$

Then $\overline{E_{kin}} = \frac{1}{2}\rho\left(\frac{\pi H}{T}\frac{1}{\sinh(kh)}\right)^2 \frac{1}{4k}\sinh(2kd) = \frac{1}{32}\rho g H^2 \frac{\sinh(2kd)}{sinh^2(kh)}$.

We notice that if $d = h$ is very large (deep water condition) we get the expression of the kinetic and potential energies found in literature $\overline{E_{kin}} = \overline{E_{pot}} = \frac{1}{16}\rho g H^2$

$$\overline{E_i} = \frac{1}{8}\rho g {H_i}^2 = \overline{E_g} - \overline{E_{beyond}} = \frac{1}{8}\rho g {H_g}^2 - \frac{1}{16}\rho g {H_g}^2\left(\frac{sinh^2(kd)}{\sinh^2(kh)} + \frac{1}{2}\frac{\sinh(2kd)}{sinh^2(kh)}\right)$$

Hence $$H_i = H_g\left(1 - \frac{1}{2}\frac{sinh^2(kd)}{\sinh^2(kh)} - \frac{1}{4}\frac{\sinh(2kd)}{sinh^2(kh)}\right)^{1/2} = H_g * K_i$$

4. Final Input wave height

From formulas above, the wave height to be entered in the system is $H_{input} = \frac{H_i}{K_{WM}\, K_i}$

In practice the formula above appears to be somewhat inaccurate due to the motions of the structure, nevertheless it gives a reasonable guess value of H_{input} for a wanted H_i.

Aiming a more accurate prediction, an attempt to make graphic empirical laws was done. The goal was to link the generated and incident wave heights according to the wave period. The period is indeed the parameter having the greatest influence on motions. However the amplitude came out to play an important role as well, so the work became too tedious.

J. Additional tests

1. 2D tests

- The roughness over the barrier has been changed. It has been presented in part X.B. It disturbed the incident waves and no acceptable results were obtained for mild slopes. A single measurement has been done for steep slopes, apparently conclusive.
- A simplified surface-roller-capturing device has been tested. Such a simply built device was hopeless to bring acceptable results.
- Second barrier. Due to the small depth the set-up was not measurable behind the second barrier. A simple observation to the naked eye shown on Figure XII-8 shows the addition of set-ups.

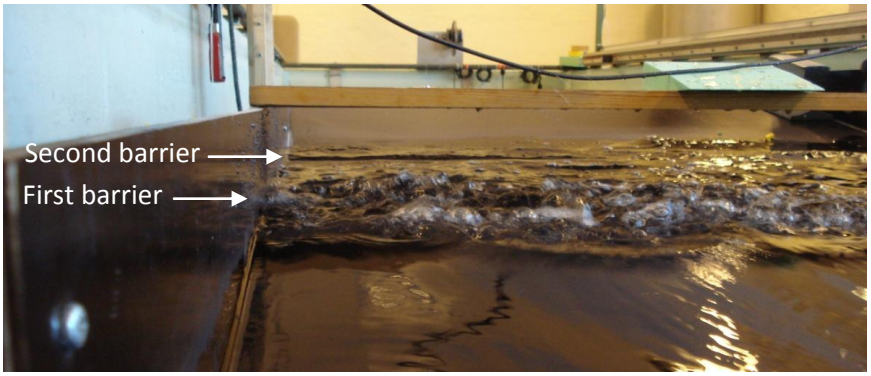

Figure XII-8: Addition of set-ups

2. 3D tests

- For these tests the barrier was narrowed for practical reasons. A seawall prevented the waves from propagating over a part of the barrier, see Figure XII-9. Behind it was a shadow zone with diffracted waves. The results are presented Figure XII-10.
- The head loss from friction has been measured by changing the alongshore position of the seaward probe from close to the channel to the shadow zone. For unknown reasons the set-up was much lower in the shadow zone, though it was expected to be higher. It might be explained by an unexpected circulation pattern shown Figure XII-9. The latter was possible because the channel entrance was protected by a wall in the region right after the barrier.
- The effect of the crest submergence of the barrier on the 3D set-up through has been analyzed.
- Obliquely incident waves have been tested. First by inclining the whole structure, secondly by inclining the guiding board by an angle θ like on Figure XII-9, creating a very rough reflector. The first case failed due to wave refraction which made the waves break normally to the barrier again.
- It came out that the crest submergence and the angle of incidence had only a weak impact in this case, at least too weak to be analyzed by tests with so much uncertainty. One can nevertheless notice the differences in 2D setups (d*=0) due to the change in hydraulic diameter (depending on h_c) and input flow rate (higher with the reflector).

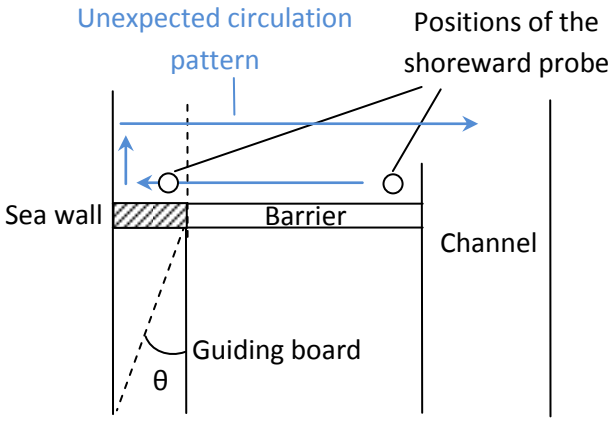

Figure XII-9: Top view of additional 3D tests

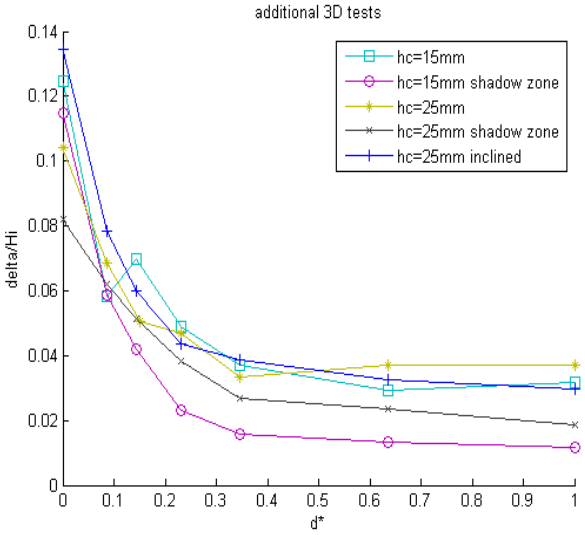

Figure XII-10: additional 3D tests results

K. Sketch of the model

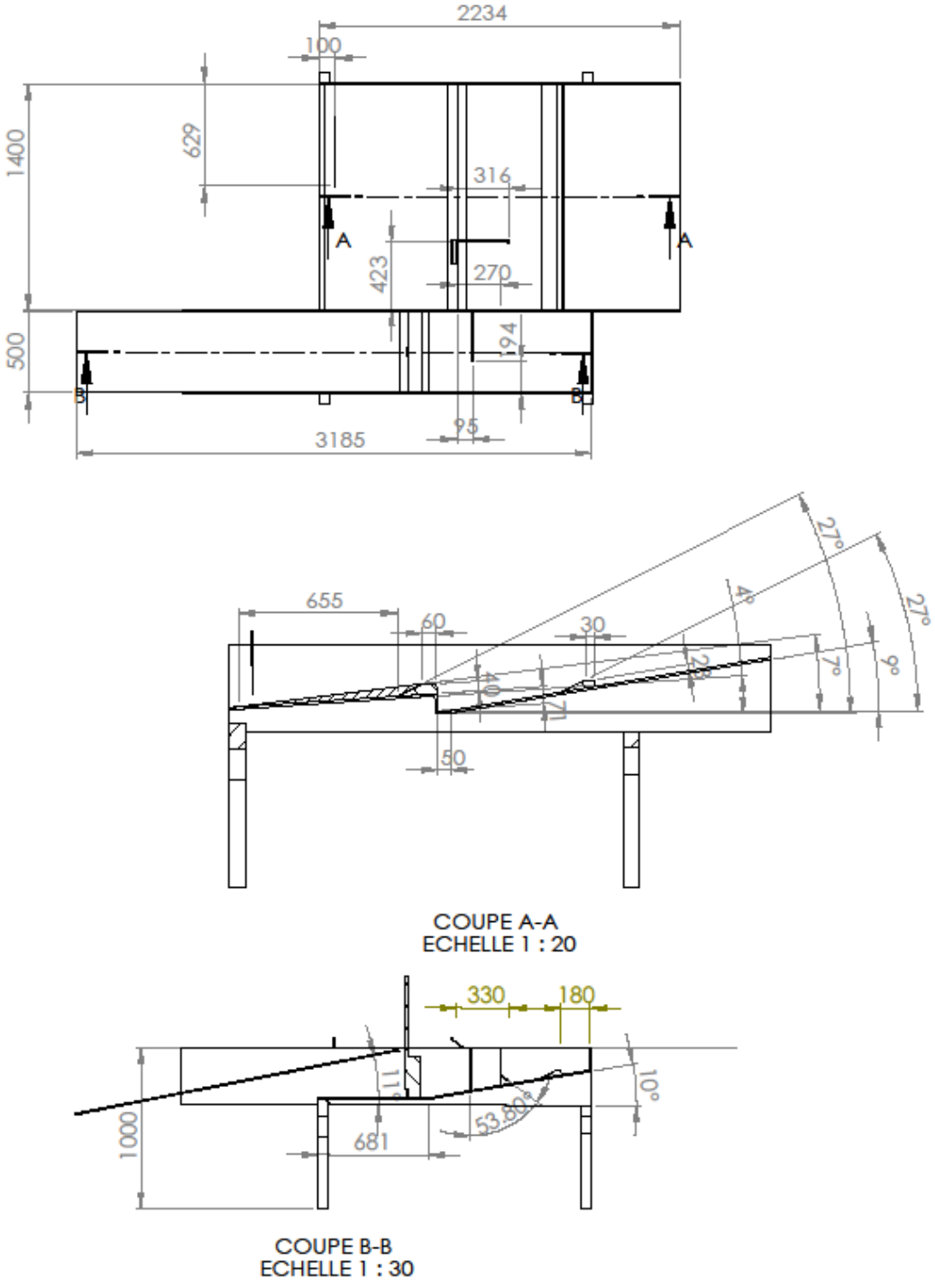

Figure XII-11: Model sketch: top view and sectional views of the barrier and the channel

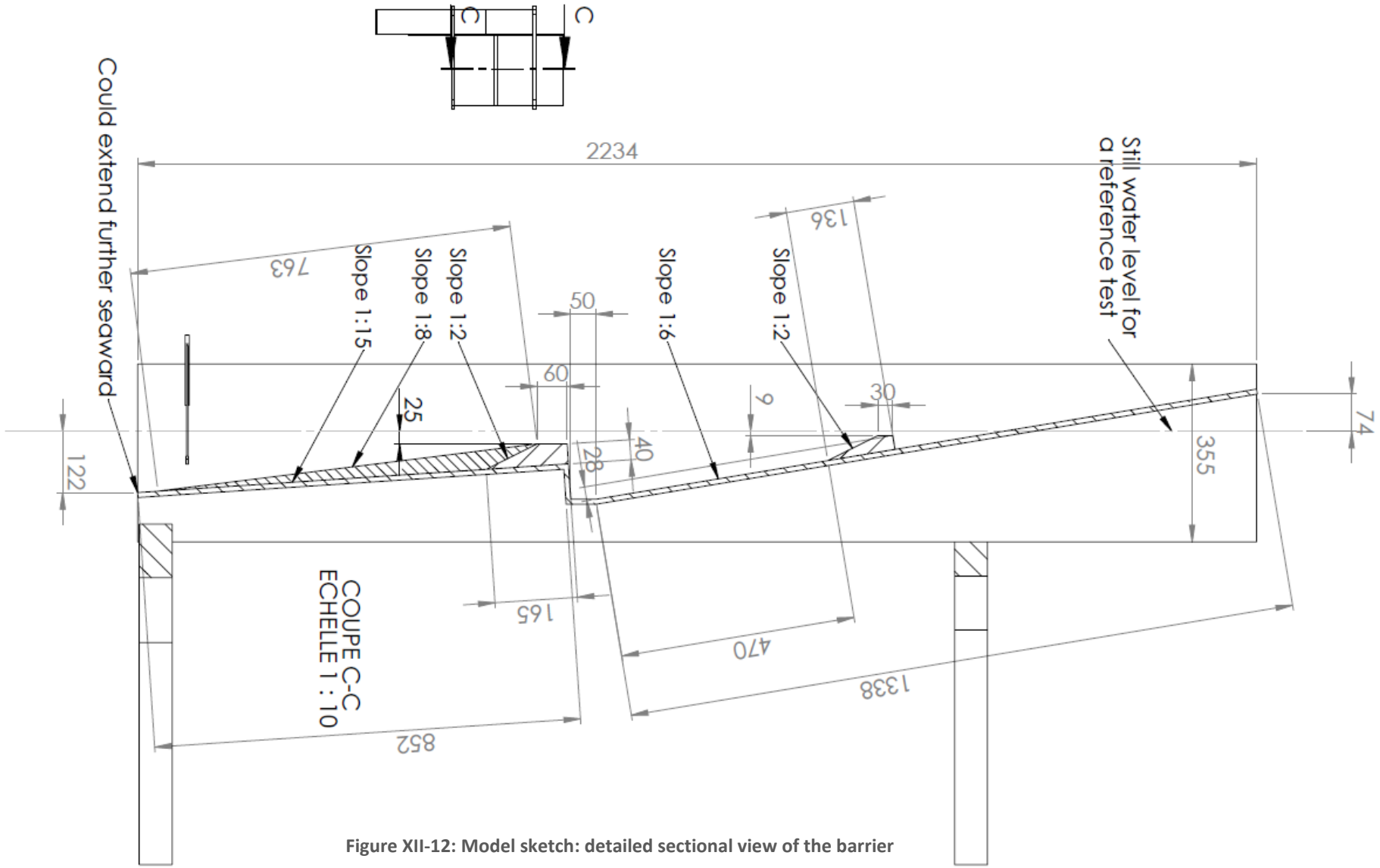

Figure XII-12: Model sketch: detailed sectional view of the barrier

L. Pictures

Figure XII-13: Model over the tank during the installation phase

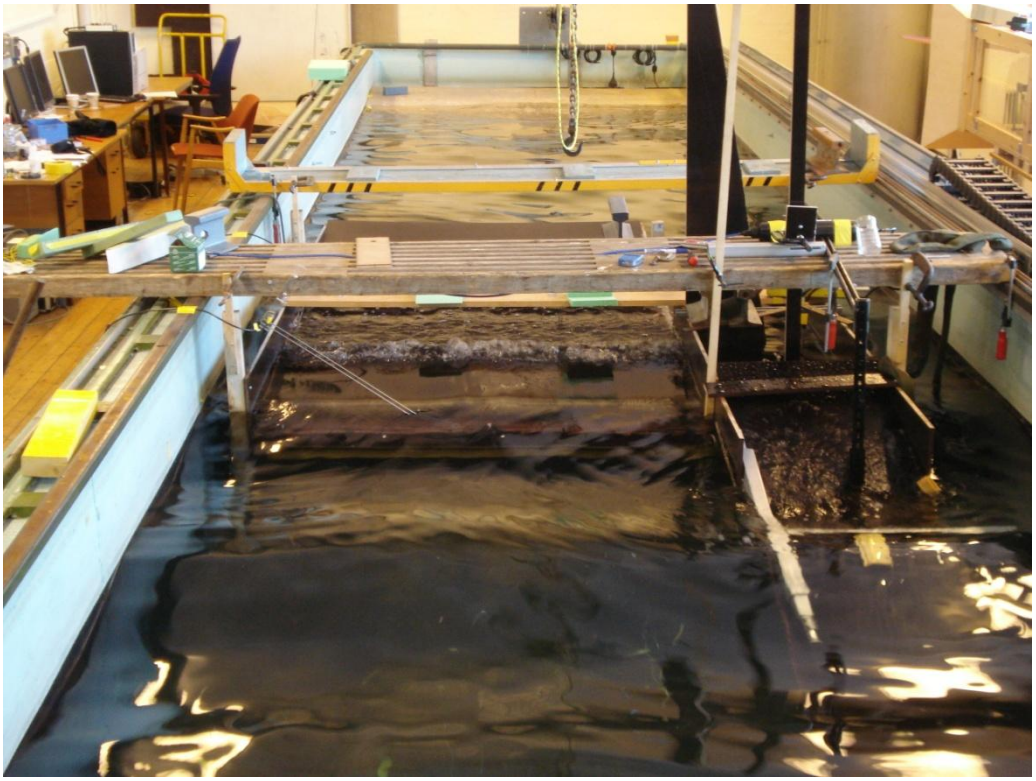

Figure XII-14: Front view

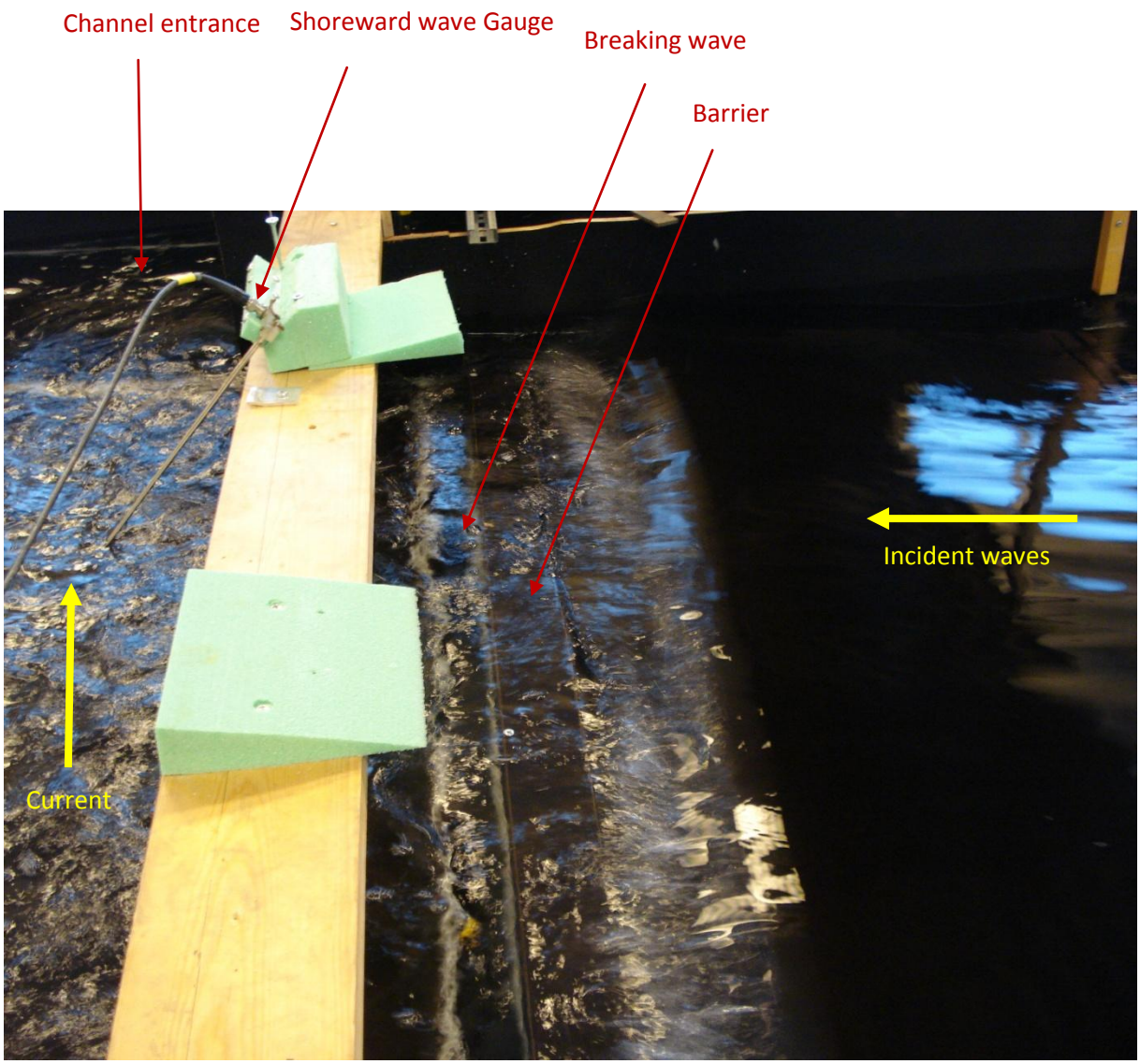

Figure XII-15: Side view

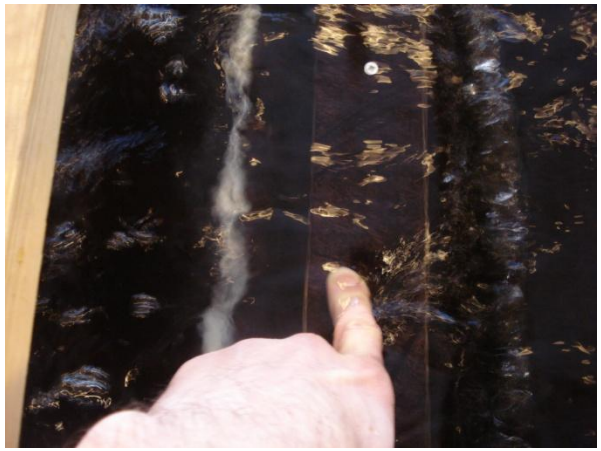

Figure XII-16: Bore-like undertow over the barrier visible to the naked eye for steep slopes

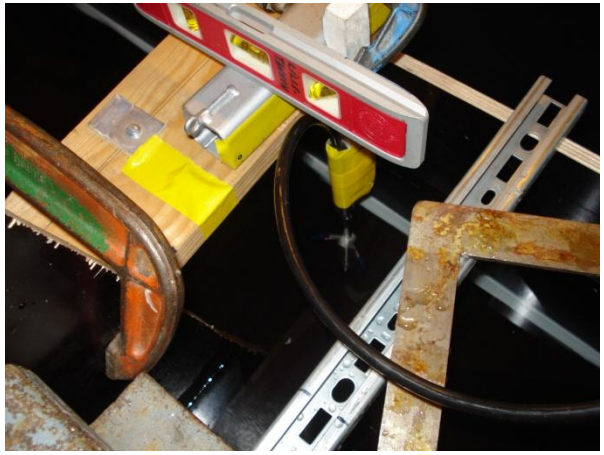

Figure XII-17: Velocity probe in the test section

Figure XII-18: Top view

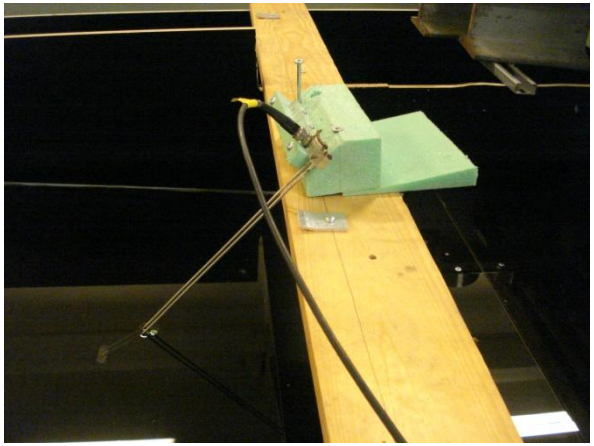

Figure XII-19: Shoreward wave gauge

Figure XII-20: Gate control

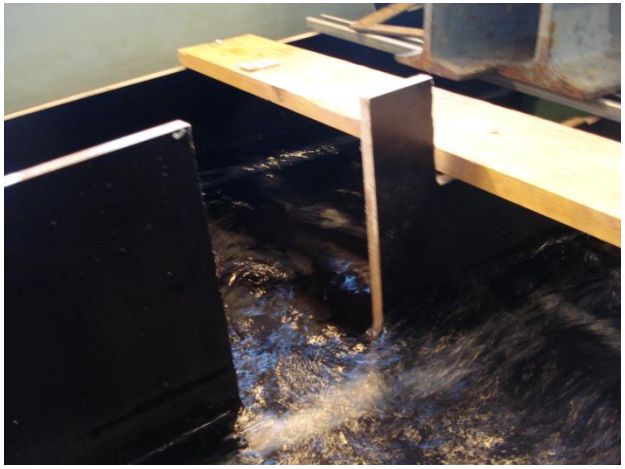

Figure XII-21: First attempt to regulate the flow rate in the channel. Strong non-uniformities and vortices in the flow are visible.

M. Matlab Scripts

The flow diagrams for the main scripts are given here. Refer to the enclosed CD for details.

1. Analytical models

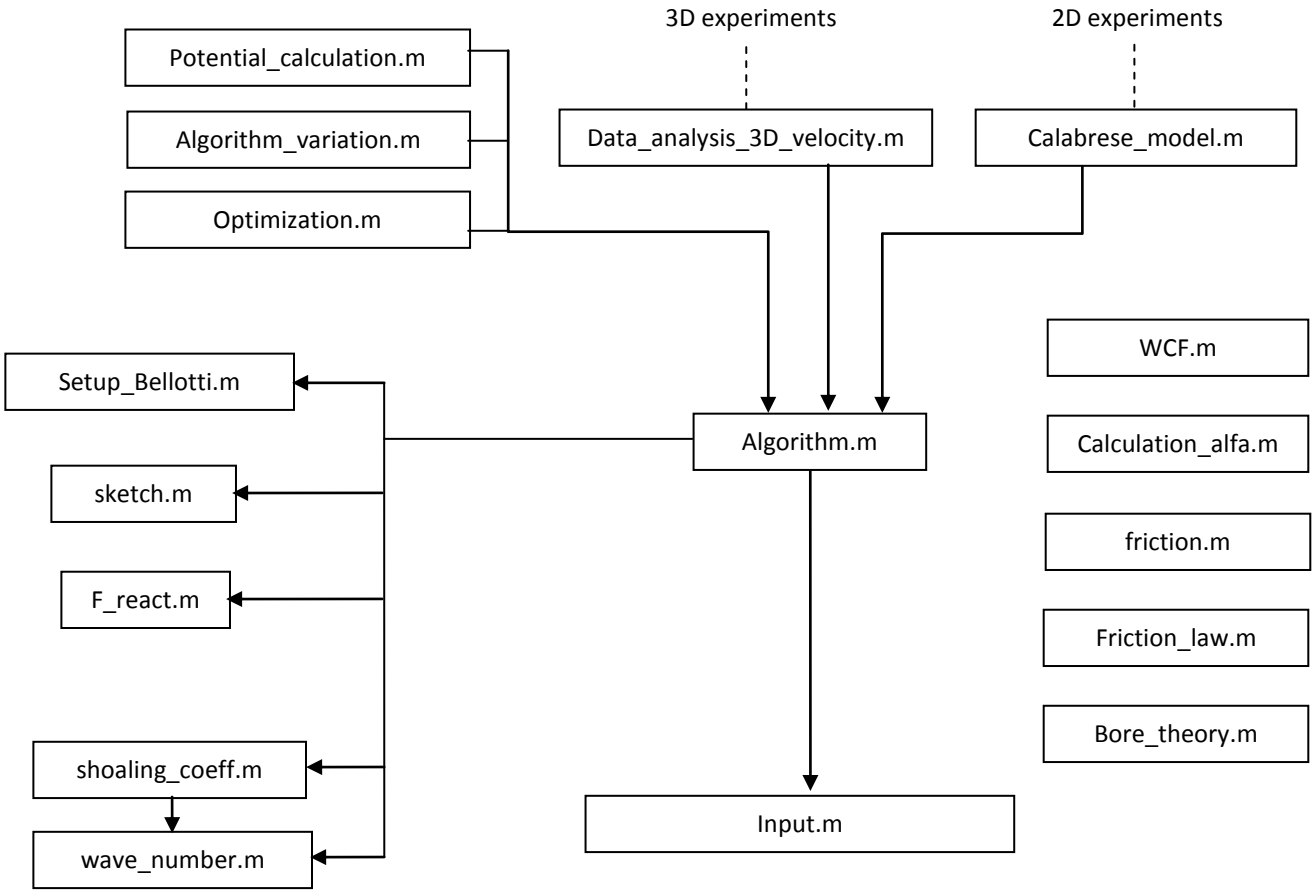

Input.m	Input parameters. 4 configurations saved: lab-scale mild-steep slope, full scale 1-2 barriers
Algorithm.m	Main function. Calculates the momentum flux set-up, the 3D set-up from Bellotti, the cross-shore discharge and the potential.
Algorithm_variation.m	Plots curves of a specified output field as a function of an input field and a range of values of a parameter (e.g. $P(\theta)$ with different K_t)
F_react.m	Reaction of the barrier
Setup_Bellotti.m	3D setup from Bellotti
Wave_number.m	Wave number from dispersion relation
Shoaling_coeff.m	Shoaling coefficient
Sketch.m	Barrier geometry from input
Optimization.m	Plots the potentials for 2 barriers as a function of discharge fraction and transmission coefficient.
Friction.m	Head losses due to friction
WCF.m	Wave shape factor from ursell number used in Calabrese (2008)
Calculation_alfa.m	Potential against discharge fraction for different models of undertow
Potential_calculation.m	Executes Algorithm.m and displays main output variables
Friction_law.m	Analytical modeling of undertow with friction law
Bore_theory.m	Analytical modeling of undertow with bore theory

2. Data extraction

The following example concerns the extraction of 2D waves. The procedure is the same for the other extraction programs (3D waves and 3D velocity).

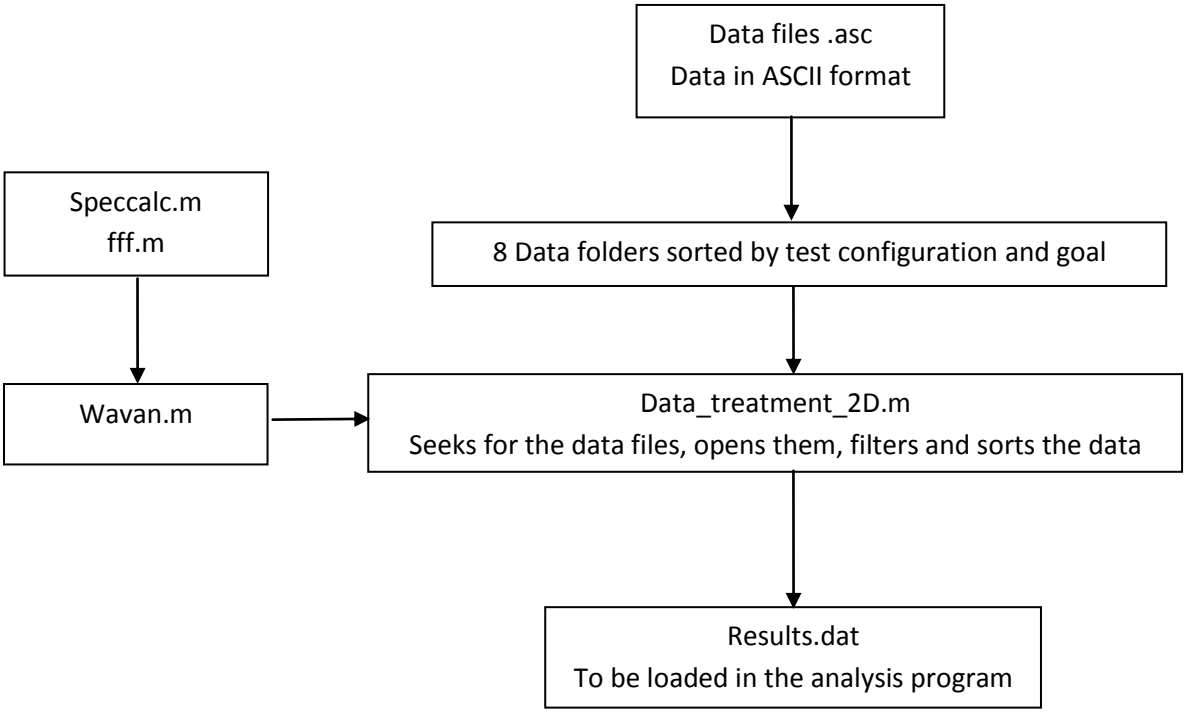

Wavan is a program to analyze time series from wave measurements provided with the book "Introduction to coastal engineering and management" by Kamphuis (2000).

3. 2D data analysis

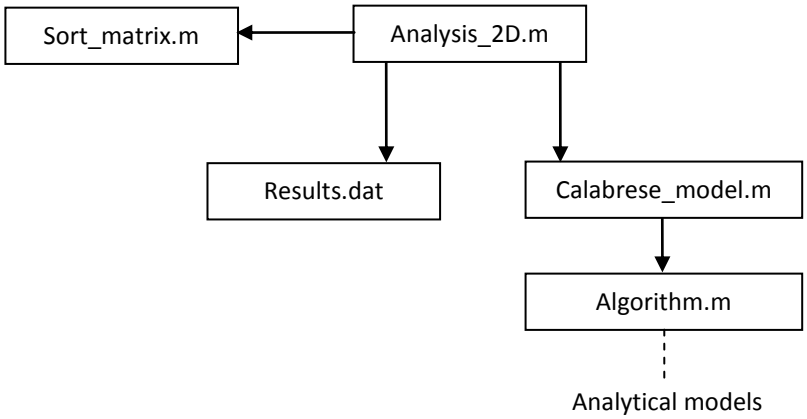

Analysis_2D.m	Sorts, and display the data on scatters.
Results.dat	Extracted experimental data
Calabrese_model.m	Comparison with analytical model
Sort_matrix.m	Sorts data in increasing order

4. 3D data analysis: set-up

Only one program: Data_analysis_3D_waves.m which sorts, plots and interpolates the set-up for 3D tests and additional tests, from extracted data contained in Results_3D_waves.mat.

5. 3D data analysis: velocity

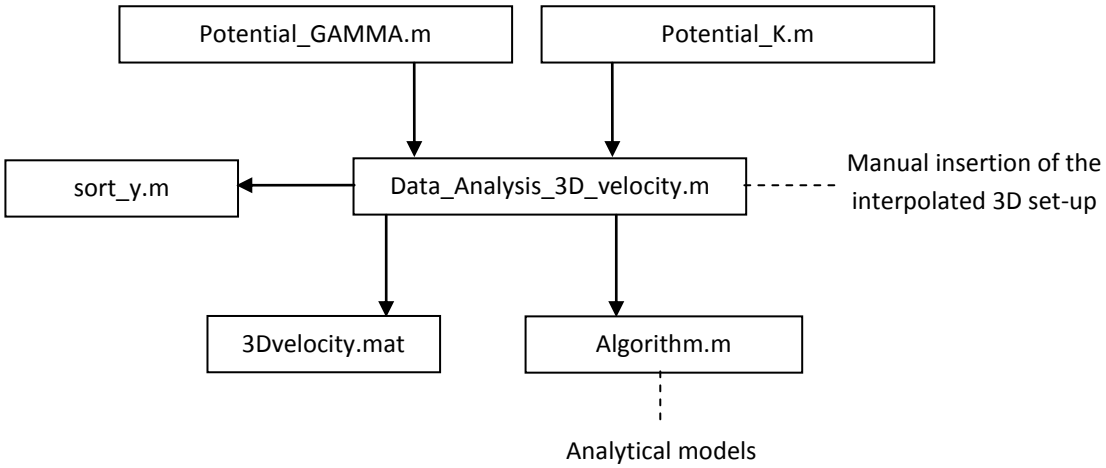

Data_Analysis_3D_velocity.m	Sorts the data, plots, interpolates and calculates the flow rate. Links the undertow with the 3D set-up. Takes into account head losses to calculate the potential. Compares with theory.
3Dvelocity.mat	Extracted experimental data
Potential_K.m	Experimental potential as a function of the head loss coefficient
Potential_GAMMA.m	Experimental potential as a function of the continuity parameter
sort_y.m	Arranges velocity data for flow rate calculation